SPIN TRANSFER TORQUE MEDIATED MAGNETIZATION DYNAMICS

MICHAEL SCHREIER

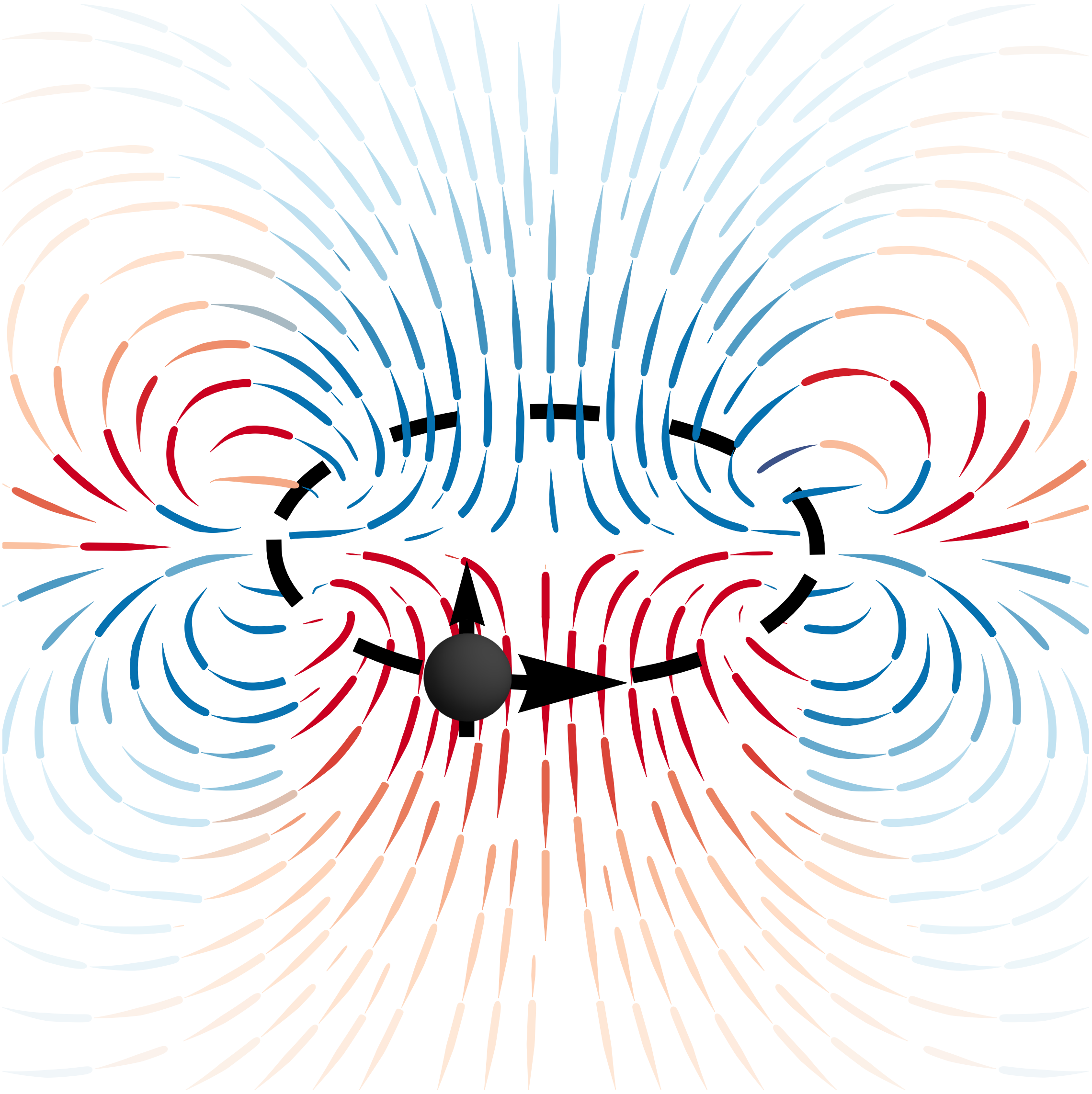

Spin current loop electric field

Bayerische Akademie der Wissenschaften
Walther-Meißner-Institut für Tieftemperaturphysik
Technische Universität München

May 5, 2017

TECHNISCHE UNIVERSITÄT MÜNCHEN

Lehrstuhl E23 für Technische Physik

Walther-Meißner-Institut für Tieftemperaturforschung
der Bayerischen Akademie der Wissenschaften

SPIN TRANSFER TORQUE MEDIATED MAGNETIZATION DYNAMICS

Michael Sebastian Schreier

Vollständiger Abdruck der von der Fakultät für Physik der Technischen
Universität München zur Erlangung des akademischen Grades eines

Doktors der Naturwissenschaften

genehmigten Dissertation.

Vorsitzender:		Prof. Dr. Martin Zacharias
Prüfer der Dissertation:	1.	Prof. Dr. Rudolf Gross
	2.	apl. Prof. Dr. Martin Brandt
	3.	Prof. Dr. Burkard Hillebrands

Die Dissertation wurde am 11.05.2016 bei der Technischen Universität München
eingereicht und durch die Fakultät für Physik am 05.05.2017 angenommen.

Things are only impossible until they’re not!
— Jean-Luc Picard (Patrick Steward)

To my parents

ABSTRACT

The flow of spin angular momentum is referred to as *spin* or *magnetization current*, just like the motion of electric charge is themed *charge current*. In electrical conductors both quantities are linked to each other via the spin Hall effect, which in turn allows to conveniently study and manipulate magnetic properties with conventional electronic methods and devices. Of particular interest for the study of spin currents is the conversion between electron based magnetic currents and those carried by magnons, the quantized ,fundamental excitations in a magnetic solid.

The focus of this thesis is on the broadband and coherent magnetization dynamics in insulating magnetic solids under a bias imposed by magnetization currents. To this end the coupling between magnetic, electronic and phononic thermal conduction channels in magnetic solids is investigated by means of analytical and numerical methods. Experiments map out the energy distribution of the magnetic excitation responsible for the emission of the magnetization currents in broadband excitation experiments and demonstrate the efficient excitation of coherent magnetization dynamics by electron based magnetization currents.

On a technical level, two novel techniques for the simple generation of broadband magnetic excitations and the precise and robust measurement of magnetization current based effects are introduced.

The thesis is complemented by the resolution of an often encountered ambiguity in the literature pertaining the absolute sign of the spin Hall effect.

ZUSAMMENFASSUNG

Ein Fluss von Spin-Drehimpuls wird als *Spin-* oder *Magnetisierungsstrom* bezeichnet, genauso wie der gerichtete Fluss von elektrischer Ladung *Ladungsstrom* genannt wird. In elektrisch leitfähigen materialien sind die beiden Größen über den Spin-Hall-Effekt miteinander verknüpft, was wiederum das Studium und die Manipulation magnetischer Eigenschaften mit Hilfe konventionalle elektronischer Methoden und Geräte erlaubt. Von besonderem Interesse für die Untersuchung von spinströmen ist die Umwandlung von auf Elektronen basierenden Magnetisierungsströmen zu solchen, die von Magnonen, den quantisierten, fundamentalen Anregungen magnetischer Festkörper, getragen werden.

Der Fokus dieser Dissertation liegt auf der Breitband- und kohärenten Magnetisierungsdynamik in nichtleitenden magnetischen Festkörpern in einem durch Magnetisierungsströme hervorgerufenen Nichtgleichgewichtszustand. Zu diesem Zwecke wird die Kopplung zwischen magnetischen, elektronischen und phononischen thermischen Leitungskanälen in magnetischen Festkörpern mit Hilfe numerischer und analytischer Methoden untersucht.

In Experimenten wird die Energieverteilung der magnetischen Anregungen, die die Emission der Magnetisierungsströme bei Breitbandanregungsexperimenten verursachen vermessen, und die effiziente Anregung kohärenter Magnetisierungsdynamik durch elektronenbasierende Mangetisierungsströme demonstriert.

Auf technischer Seite werden zwei neuartige Methoden für die einfache Erzeugung breitbandiger magnetischer Anregungen und für die genaue und zuverlässige Messung von auf Magnetisierungsströmen basierenden Effekten vorgestellt.

Ergänzend klärt diese Dissertation auch die oft in der Literatur anzutreffenden Doppeldeutigkeit des absoluten Vorzeichens des spin Hall Effekts.

CONTENTS

1

INTRODUCTION

Solid state systems are often modeled as an ensemble of harmonic oscillators, i.e. by a group of particles orbiting some other group of particles. This concept applies, within some limits, not only to the microscopic world but also describes the actions of certain macroscopic objects. From point like particles the enumeration extends to planets that orbit a star, stars that orbit the galactic core and galaxies that orbit around a common barycenter (center of mass)[1]. Magnetism is a phenomenon encountered on all these length scales, from magnetic fields spanning multiple galaxies [7, 8] to the electron magnetic moment or electron spin. Because microscopic and macroscopic world are so similar conceptually, findings on one end of the length spectrum may equally be relevant on the other. Nevertheless, each end still provides its own unique set of phenomena awaiting to be uncovered. This thesis revolves around the fundamental excitations in magnetically ordered lattices and the transfer, manipulation and transport of magnetic properties, the latter of which occurs on a scale that often does not exceed some nanometers.

Magnetism on a microscopic scale is attractive for both fundamental research and technological applications, as some of its quantum mechanical properties are easily accessible, even at room temperature. In particular, spins and the related magnetic moments, vectorial quantities in a semi-classical treatment, can be probed and manipulated with relative ease, e.g. by conventional magnetic fields. Thereby, an additional degree of freedom can be exploited in fundamental research and for applications. Another important point derives from the fact that electrons, the agents of conventional electronics, are intrinsically magnetic and allow for convenient coupling of the charge and spin degree of freedom. Conducting, magnetically ordered materials have been exploited for this very reason for some time in many applications and are still an active area of fundamental research. Although the coupling of charge and spin degree in conducting, magnetically ordered materials is a

---

[1] $1/r$-type central potential problems can be transformed to mirror the harmonic oscillator by the *Levi-Civita transformation* in two dimensions [1] and similarly by the *Kustaanheimo-Stiefel transformation* for the three dimensional Kepler problem (i.e the effective potential formed by the gravitational $-1/r$ and $1/r^2$ centrifugal term) as discussed in Refs. [2–5] and briefly reviewed in e.g. Ref. [6].

blessing on one side it also complicates design and interpretation of devices and experiments on the other. Within the last decade, however, it turned out that even magnetic insulators in which the charge degree of freedom is completely frozen out are promising for applications. Actually, since charge currents are frozen out magnetic insulators represent clean model systems for studying pure magnetization currents. Combined in heterostructures with specific metals, the magnetic properties of the magnetically ordered solid can be studied by probing the electrical properties of the metal. Here, spin transfer torques provide an interface between localized magnetic moments and magnetization currents, associated with the motion of (quasi-)particles with a finite magnetic moment. Spin transfer torques, for instance, couple the excitation of the magnetic moments in the insulating, magnetically ordered material to the spatial distribution of electron spins in an adjacent metallic layer. In some metals, platinum being the prime example, this also affects the electric properties of the metal and can therefore be detected with relative ease. In this context, three effects exemplarily demonstrate the relevance of spin transfer torques: spin pumping [9], spin Seebeck effect [10] and spin Hall magnetoresistance [11]. Spin pumping covers the transfer of spin angular momentum from the insulating, magnetically ordered material to the electrons in the metal, while the spin Hall magnetoresistance is mainly concerned with the inverse process, i.e. the absorption of spin angular momentum from the electron system by the magnet. The spin Seebeck effect covers both directions of spin angular momentum transfer through the presence of a fluctuating spin current caused by thermal noise in the metal [12] but is, in contrast to the aforementioned two, exclusively an incoherent phenomenon.

This thesis aims to broaden the knowledge about magnetization (spin) currents, covering both the state in the magnetic insulator as well as in the metal under spin angular momentum transfer. Without anticipating the more comprehensive listing of all results covered in this thesis below, notable scientific contributions include: (i) the design and implementation of experimental techniques for fast and robust detection of spin current based effects and in-situ thermal spin current generation and detection, (ii) a numerical study of the spatial distribution of thermally induced magnetic excitations in the insulator, (iii) experimental insights into their spectral composition derived from picosecond optothermal excitation experiments, (iv) the resonant excitation of coherent magnetization dynamics, both uniform and spatially varying, by means of electronically controlled spin angular momentum absorption. The last-mentioned experiment is noteworthy in particular, due to the simultaneous occurrence of all the spin effects introduced above, which demonstrates the intricate relations that need to be considered when designing nanostructures for applications.

Picking up on the notion that results in the microscopic world are relevant for the macroscopic world and vice versa, the concept of magnetization currents also applies to e.g. Earth orbiting Sun. Earth's property as a giant magnetic dipole has not only been utilized by men for over 2000 years for navigation purposes but also renders the time average of Earth's passage around sun a closed spin (and mass) current loop. By considering an extension of Maxwell's equations to include magnetization (dipole) currents [13, 14] this spin current loop generates a peculiarly shaped electric field that expels both positively and negatively charged ions from the center of its orbit (see title illustration) with a strength that reaches several mV/m for e.g Jupiter's inner moons.

The detailed organization of the thesis is described in the following.

Chapter 2 serves as the starting point and introduces the key concepts for spin transport in nanostructures. An emphasis is therein put on the diffusive character of this type of transport, as well as the various means to generate and detect spin accumulations.

Chapter 3 is a compact overview over the magnetic insulator yttrium iron garnet that is employed for all experiments in this thesis. Its physical properties and the fabrication of yttrium iron garnet based samples are briefly discussed.

The first experimental chapter (Ch. 4) introduces a measurement technique based on the utilization of continuously rotating magnetic fields, implemented in experiment by mechanical rotation of a permanent magnet assembly. This enables fast, sensitive and robust measurements of spin current based effects. The mathematical model underlying the analysis is derived, with a focus for application to the spin Hall magnetoresistance but also generalized to other phenomena. The setup is characterized and first experimental results are discussed.

The spin Seebeck effect links heat and spin currents and is discussed in both the static as well as the dynamic regime in Ch. 5. The first part of this chapter demonstrates how finite elements analysis can be used to gain insight into the energy transfer between the electronic, phononic and magnonic subsystems on a nanometer scale. The simulation extends previous attempts to solve energy transfer problems across interfaces and with coupled heat conduction channels. It makes a quantitative determination of the spatial thermal

profiles of magnetic excitations possible also for complex geometries or boundary conditions, or both. The simulation is verified by comparison with recent experiments. The corresponding results have been published in Phys. Rev. B **88**, 094410 (2013) [15].
The second part of Ch. 5 deals with the spin Seebeck effect which is studied in terms of its transient response to periodical heating up to frequencies of several gigahertz. The impact of the yttrium iron garnet film thickness is studied and compared to a theoretical modeling of the magnon dynamics in the system. The results are compared to recent experimental studies, which enables the formulation of a qualitative model that connects the magnon dynamics in the magnetic insulator to the transient voltage response measured in experiment. These insights have been compiled into a manuscript submitted for peer-review.
The last part of this chapter introduces an alternative experimental approach to conventional heating techniques in spin Seebeck effect experiments on yttrium iron garnet/platinum samples. The approach utilizes the metallic Pt layer as spin detector and as a resistive heater simultaneously. It is then demonstrated how the signal of interest is recovered below a vast spurious background voltage signal. Experiments to verify the consistency of the method as well as the behavior of the spin Seebeck effect under large external magnetic fields and at low temperatures are presented. The technique has been published in Appl. Phys. Lett. **103**, 242404 (2013) [16].

In Ch. 6 a didactic dilemma, inseparably connected with the interpretation of experimental results, is addressed. The dilemma concerns the absolute sign of the spin Hall angle, perhaps the most central quantity for spin current based experiments. A theoretical toy model is developed to unambiguously define the sign of the spin Hall angle. Additionally, a guide to the experimentalist is given to allow a clear and easy identification also in practical applications. These efforts have been compiled into a manuscript published in J. Phys. D: Appl. Phys. **48**, 025001 (2015) [17].

Chapter 7 deals with the direct, resonant excitation of magnetization dynamics by means of the spin transfer torque. The effect, which had only been demonstrated on conducting magnetic materials so far, is here validated also for the magnetic insulator yttrium iron garnet. By exploiting the scaling of the spin transfer torque with the magnetic layer thickness together with theoretical modeling of the experiment the spin torque effects are identified and separated from spurious contributions. The findings have also been published in Phys. Rev. B **92**, 144411 (2015) [18].
In an extension of this proof of principle experiment it is also demonstrated how spin torque mediated magnetization actuation

can be utilized to excite standing spin waves and extract magnetic properties of a sample in an all electrical measurement scheme.

To conclude the thesis, Ch. 8 briefly summarizes the main results presented in the preceding chapters.

As already indicated, the results presented in chapters 5, 6 and 7.1 have previously been published or submitted for peer-review. The corresponding text and figures in these chapters are, in large parts, taken from the respective manuscripts (referenced prominently in each chapter).

2

THEORETICAL FOUNDATIONS

The Stern-Gerlach experiment [19, 20] demonstrated that particles possess a quantum property that was later called *spin*. Provided the particle may be attributed a finite diameter, a classical picture of a particle's spin is the rotation of the particle around a particular axis through its center of mass. Indeed, the mathematical treatment of the quantum mechanical spin follows the laws applicable to classical angular momentum, which makes this picture particularly appealing. Fundamentally, however, it is important to distinguish between a particle's spin $\boldsymbol{s}$ and its angular momentum $\boldsymbol{l}$. The quantity $\boldsymbol{s}$ is a consequence of relativistic quantum electrodynamics which attribute it a value of $\boldsymbol{s} = \frac{\hbar}{2}\boldsymbol{\sigma}$ (for spin-1/2-particles), with the Planck constant $\hbar$ and the vector of Pauli matrices $\boldsymbol{\sigma}$. The quantity $\boldsymbol{l}$ on the other hand, is the well known classical angular momentum obtained from the motion of a massive particle around a fixed point in space. At the same time both quantities are linked to the magnetic moment $\boldsymbol{\mu}_{l(s)}$ of the particle by means of the gyromagnetic ratio $\gamma = q/(2m)$ with the particle's charge q and mass m by the relation $\boldsymbol{\mu}_{l(s)} = \gamma\, \boldsymbol{l}(\boldsymbol{s})$. For electrons $\gamma = g\mu_\mathrm{B}/\hbar$, with the Landé(-$g$)-factor g and the Bohr magneton μ_B.

The behavior of a magnetic moment in an external magnetic field $\boldsymbol{B}$ can be derived from basic quantum mechanics. The time evolution of the expectation value $\langle \boldsymbol{o} \rangle$ of an operator $\boldsymbol{o}$ is given by the equation

$$\frac{d}{dt}\langle \boldsymbol{o} \rangle = \frac{i}{\hbar}\left\langle [\mathcal{H}, \boldsymbol{o}] \right\rangle, \tag{2.1}$$

where $\mathcal{H}$ is the Hamilton operator of the system and $[\mathcal{H}, \boldsymbol{o}]$ denotes the commutator of $\mathcal{H}$ and $\boldsymbol{o}$. For the case at hand $\mathcal{H} = -\boldsymbol{\mu} \cdot \boldsymbol{B}$, i.e. the Zeeman energy [21]. Utilizing the angular momentum commutation relation $[\boldsymbol{l}_i, \boldsymbol{l}_j] = i\hbar\epsilon_{ijk}\boldsymbol{l}_k$ provides the Larmor equation

ϵ_{ijk} *is the* Levi-Civita symbol *or* totally antisymmetric tensor.

$$\frac{d}{dt}\langle \boldsymbol{\mu} \rangle = -\gamma\langle \boldsymbol{\mu} \rangle \wedge \boldsymbol{B}, \tag{2.2}$$

which describes a precessing motion of $\boldsymbol{\mu}$ around $\boldsymbol{B}$.

In a solid with long range magnetic order many individual magnetic moments are tightly locked together and behave as one single, large magnetic moment under application of the external field. The quantized elementary excitations of such an arrangement are called *magnons*. Conceptually, single magnons are described by plane waves

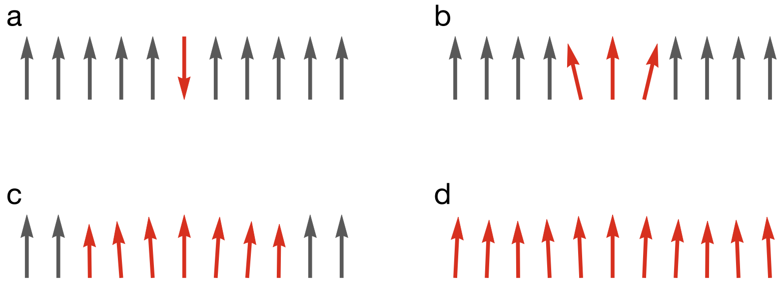

Figure 2.1.: At zero temperature all magnetic moments are aligned parallel to a direction imposed e.g. by an external magnetic field. The deflection of a single magnetic moment (**a**), corresponding to an excited state of the ensemble (i.e. a magnon) is energetically unfavorable and is redistributed among the neighboring moments until the excitation has spread throughout the entire magnetic lattice (**b-d**).

and are thus fully delocalized within the magnetic lattice. In a realistic scenario, however, the deflection of a single (or more) magnetic moment of the underlying lattice that leads to the generation of a magnon will not only excite a specific vibrational (magnon) mode but rather an entire collection of modes within a certain frequency interval. The corresponding wave function, i.e. the superposition of multiple plane waves, can then be localized to a volume that corresponds to Fourier transform of the frequency (momentum) interval. Just as sometimes done for phonons it can then make sense to treat magnons as localized particles – if only for a short time after their creation. This viewpoint can be especially helpful in forming an intuitive understanding for the interaction of magnons with other particles, but is not necessary to formulate a consistent theory. At any rate, each magnon decreases the projection of the magnetic moment along $\boldsymbol{B}$, by inducing an oscillation of the magnetic lattice (Fig. 2.1). Magnons thus posses a magnetic moment antiparallel to that of the host material. Just like other particles magnons possess a characteristic energy E that is related to its wave number q via the dispersion relation $\omega(q)$. Although the full dispersion may turn out to be much more complex [22] in specific materials, a simple form is given by [23]

$$\omega = \left[\left(\gamma B + \frac{Dq^2}{\hbar} \right) \left(\gamma B + \frac{Dq^2}{\hbar} + \gamma \mu_0 M \sin^2 \theta \right) \right]^{1/2} \tag{2.3}$$

with the so-called spin wave stiffness D, the vacuum permeability μ_0, the magnetic field B, the magnetization figure M of the magnetic host material, and the angle θ enclosed by $\boldsymbol{q}$ and $\boldsymbol{B}$. For many practical applications, Eq. (2.3) can be further simplified to the quadratic expression $\omega = \gamma B + Dq^2/\hbar$. The dispersion relation allows to deduce other quantities such as the propagation speed or specific heat for individual particles and an entire ensemble, respectively. As bosons with spin 1, magnons in equilibrium are subject to Bose-Einstein statistics giving their average occupation number.

The coupling of magnons across an interface to conduction electrons in adjacent metallic materials is crucial for most effects discussed in this thesis. This coupling enables an all electrical detection of magnetic properties which can take advantage of decades of optimization of highly sensitive electronic measurement devices. The laws governing such purely electric transport are well established and will not be discussed in detail in the following. However, even materials without long-range magnetic order, i.e. para- or diamagnetic solids, can host magnetization currents. In the following such (conducting) materials will be referred to as *normal metals* and the short term *magnets* will be used for ferro-, ferri- and antiferromagnetic materials. While most of the effects to be discussed in the following are expected to be present in or in conjunction with all types of magnets, this thesis is exclusively concerned with the ferrimagnetic insulator yttrium iron garnet, introduced in more detail in Ch. 3. The treatment of spin transport in normal metals requires the introduction of some core concepts and equations. In particular, when magnets and normal metals are combined in heterostructures, a rich collection of effects can be observed.

2.1 SPIN TRANSPORT IN NORMAL METALS

In normal metals, the distribution of the electrons spin orientation is random. At elevated temperatures, this condition holds even in the presence of large external magnetic fields which only bring about minuscule spin polarizations. In the absence of an external bias (e.g. an applied voltage) the motion of the electrons can also be considered random, that is it is well described by random walk behavior as depicted in Fig. 2.2a.

In Pt a fraction of about 10^{-9} of all conduction electrons is polarized at a magnetic field of 1 T.

For $t \to \infty$ the random motion negates any local deviation from the equilibrium state and maximizes the system's entropy (Fig. 2.2b). For large ensembles of particles the random walk process is described by the diffusion (heat) equation $\frac{\partial \mu_\mathrm{s}}{\partial t} = D\Delta\mu_\mathrm{s}$, where μ_s is a chemical potential, i.e. a measure for the total number of spin-$\circ$ (or $\bullet$) particles, and D is the characteristic diffusion parameter of the system. Due to spin flip processes during scattering events the total number of spin-$\circ$ (or $\bullet$) particles is not conserved. This adds a term μ_s/τ with the scattering rate $1/\tau$ (lifetime τ) to the diffusion equation above to form a reaction-diffusion system

$$\frac{\partial \mu_\mathrm{s}}{\partial t} = D\Delta\mu_\mathrm{s} + \frac{\mu_\mathrm{s}}{\tau}\,, \tag{2.4}$$

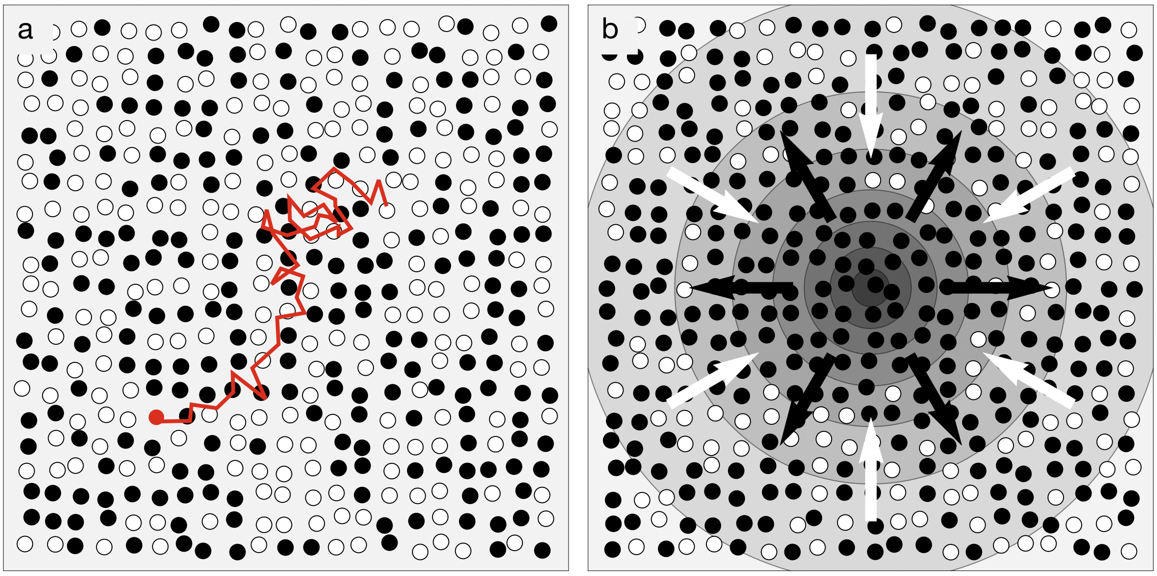

Figure 2.2.: **a** In a naïve picture the conduction electrons in a normal metal can be envisaged as a set of discrete particles. The motion of any individual particle (spin-● or spin-○ electrons) can be considered random and one does not need to consider macroscopic forces to describe the system at large. It is important to realize that random walk preserves the average particle density for large particle numbers. **b** On large scales and over long time periods, random motion averages out any initial imbalance in the spin distribution. Considering an initial surplus of spin-● in the center particles the random motion, on average, generates an outward spin-● current and an inward spin-○ current until the system is in equilibrium again.

which is commonly referred to as the *spin diffusion equation* [24–26]. The quantity μ_s thereby is the spin chemical potential and $\sqrt{D\tau} = \lambda$ is the spin diffusion length. The spin diffusion length typically takes values between few nanometers up to few microns, depending on the material. In practice, the exact numerical value for a certain material is often contested as different experimental techniques often yield vastly different numbers. This is further complicated by varying impurity levels, crystalline quality and correction factors [27, 28] that are not always accounted for in the analysis. Another point to note is that the diffusion parameters are most often treated as scalars, i.e. the diffusion process is assumed to be fully isotropic. Fundamentally, however, factors such as crystallinity render the process anisotropic and one should expect the spin diffusion length in particular to be dependant on the chosen measurement geometry.

Quite often one is interested in spin currents (spin current density $\boldsymbol{j}_s$) rather than the spin chemical potential itself. Analogously to how one obtains charge currents from the electric potential by taking the negative of its gradient multiplied by the (electrical) conductivity σ

divided by the electron charge $-e < 0$, spin currents are derived from the chemical potential as [29]

$$\boldsymbol{j}_{\mathrm{s}} = -\frac{\hbar}{2e}\frac{\sigma}{e}\nabla\mu_{\mathrm{s}}. \tag{2.5}$$

Here the additional prefactor $\hbar/(2e)$ accounts for the different dimensionality of spin currents compared to charge currents which is discussed in more detail in the following section. It is intriguing to think of spin currents as a sort of directed motion of electrons with a particular spin orientation. Microscopically, however, the spin current is nothing else but a biased random walk process of countless individual particles. Since this bias only acts on the spin degree of freedom (particle density as a whole being conserved), the random walk picture also explains why spin currents do not transport any net charge, although the spin is tied to charged carriers. For the situation depicted in Fig. 2.2b the net flow of one spin species in a given direction is counterbalanced by an opposing flow of the other spin species, which cancels the charge transfer associated with the motion of the individual particles. Spin currents as derived in Eq. (2.5) are also called *pure spin currents* for this reason.

2.2 SPIN HALL EFFECT

While pure spin currents $\boldsymbol{j}_{\mathrm{s}}$ do not transport any net charge, they are tied to charge currents $\boldsymbol{j}_{\mathrm{c}}$ via the spin orbit interaction. Predicted by Dyakonov and Perel [30], and picked up almost three decades later by Hirsch [31], the spin orbit interaction renders the electron transport spin sensitive, either due to spin selective scattering at impurities or as a property of the band structure. The strength of these effects is commonly compiled in a parameter θ_{SH} which is referred to as the *spin Hall angle*. In analogy to the conventional Hall effect the spin Hall effect generates a spin current transverse to the original charge current (Fig. 2.3). Correcting for dimensionality between $\boldsymbol{j}_{\mathrm{s}}$ (in units of $[\mathrm{J/m^2}]$) and $\boldsymbol{j}_{\mathrm{c}}$ (in units of $[\mathrm{A/m^2}]$) the spin Hall effect and its inverse, the generation of a transverse charge current from a spin current, are described by the equations [17]

$$\boldsymbol{j}_{\mathrm{s}} = +\theta_{\mathrm{SH}}\frac{\hbar}{2e}\boldsymbol{j}_{\mathrm{c}} \wedge \boldsymbol{\sigma}_{j_{\mathrm{s}}}, \tag{2.6}$$

$$\boldsymbol{j}_{\mathrm{c}} = +\theta_{\mathrm{SH}}\frac{2e}{\hbar}\boldsymbol{j}_{\mathrm{s}} \wedge \boldsymbol{\sigma}_{j_{\mathrm{s}}}, \tag{2.7}$$

where $\boldsymbol{\sigma}_{j_{\mathrm{s}}}$ is the spin polarization direction of $\boldsymbol{j}_{\mathrm{s}}$. This was first experimentally observed by Kato *et al.* [32] in a semiconductor, and has since been observed in a large number of materials [33]. Scaling as the proton atomic number to the fourth, the spin orbit interaction and thus the spin Hall angle is particularly large in heavy metals such as platinum, tantalum or tungsten. However, the exact relation between

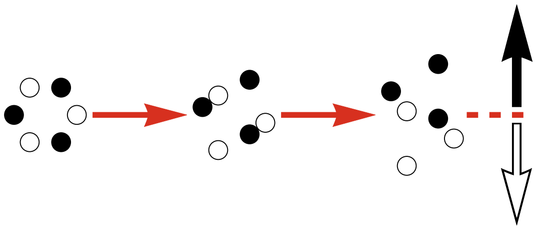

Figure 2.3.: In materials with non-vanishing spin Hall angle scattering processes are biased with respect to the electrons' spin orientation. Over the course of several such scattering processes the original charge current develops a transverse spin current component.

the spin orbit interaction and the spin Hall angle is fairly complicated and other heavy metals like gold or even uranium [34] have much smaller spin Hall angles despite comparably or even much larger atomic numbers. The spin Hall angle can take both positive and negative values.

The experimental determination of the numeric value of the spin Hall angle is unfortunately nontrivial. In most cases it requires knowledge of at least the value of the spin diffusion length λ which, as discussed in Ch. 2.1, is itself subject to debate in the literature. Subsequently the numerical values in literature, even for very commonly used materials such as platinum, quite often vary by an order of magnitude [33].

2.3 SPIN HALL MAGNETORESISTANCE

Spin currents, generated e.g. by the spin Hall effect, also affect the electrical properties of normal metals. For an intuitive understanding of this phenomenon Eq. (2.4) has to be solved for a finite conductor. The solution to this problem shows that the spin Hall effect generates a spin accumulation (nonzero spin chemical potential μ_s) at the edges of the conductor. The spin accumulation here counterbalances the spin Hall effect induced spin current which, to first order, nullifies the spin Hall effect generated spin current and thus leaves a longitudinal charge transport unaffected. Contacting the edges of the normal metal conductor with a magnet, however, enables tuning of the spin accumulation via the *spin transfer torque* discussed further below. More specifically, the spin transfer torque allows the spin accumulation to relax into the magnet, i.e. it negates the cancellation of the spin Hall effect generated spin current. Due to the finite diffusion length of spin currents they are dissipative in nature and thus contribute a finite offset to the (electrical) resistivity in the normal metal. The configuration comprised of a (thin) normal metal in contact with a magnet serves as the model system for the remainder of the discussion in this chapter.

The absorption of the spin accumulation by the magnet which is mediated by the spin transfer torque occurs in the form of a torque acting on the magnetic moments in the magnet. One distinguishes between several types of spin transfer torques. Of particular interest to the experiments in this thesis is the so-called Slonczewski-like torque [35–38] which originates from the particle-wave duality of the electrons. In a semi-classical picture the spin of an incident electron will start to precess in the exchange field of the magnet [*cf.* Eq. (2.2)] upon passing into the magnet or scattering at its interface. Because electrons may possess any wave number permitted by the fermi surface in the normal metal, and thus the passage through the exchange field is largely random, the spin component transverse to the magnetization vanishes in the superposition of all possible scattered wave functions at a short distance from the interface (Fig. 2.4) due to classical dephasing [36, 39, 40]. At this point it is important to emphasize that spin or magnetic moment orientation are quantum mechanical states of angular momentum rather than simple vectors. Although this aspect can sometimes be neglected for purely experimental purposes, it is crucial to understand that the term "transverse" actually signifies (or can be understood as) a particular linear combination of the two possible spin states, rather than a state that vanishes under projection on any of the two like a simple vector would. Keeping this in mind, the vanishing transverse electron spin (angular momentum) is accounted for by a torque exerted on the magnetization. The inverse process in which spare angular momentum in the magnet is used to align electron spins impinging on the interface with the magnetization will be discussed in Ch. 2.4. For magnetic insulators in particular, another important point is that the superposition of incident and reflected electron wave function, each of fermionic character, can also be understand as the wave function of a single bosonic (spin 0 or 1), charge neutral particle – a concept also employed for the description of scattering events at normal metal/superconductor interfaces [41]. The Slonczewski-like torque, associated with the dissipation of transverse spin moment, is proportional to

$$\boldsymbol{\tau}_{\mathrm{Slonczewski}} \propto \mathrm{Re}\left(g^{\uparrow\downarrow}\right) \mu_{\mathrm{s}}\, \boldsymbol{m} \wedge (\boldsymbol{m} \wedge \boldsymbol{\sigma}_{\mu_{\mathrm{s}}}), \tag{2.8}$$

where $\boldsymbol{\sigma}_{\mu_{\mathrm{s}}}$ is the spin accumulation polarization vector, $\boldsymbol{m}$ is the magnetization unit vector and $g^{\uparrow\downarrow}$ is the spin mixing interface conductance [38], which is a measure of the spin flip scattering rate of a given normal metal/magnet interface [42, 43]. For highly reflective magnets (i.e. insulators) or ones that exceed the transverse electron spin coherence length the spin mixing conductance can be formulated solely in terms of the spin dependent interface scattering coefficients [39, 40, 44]. The latter can be calculated from relatively straight forward wave function matching at the interface as outlined

The experimental determination of the numeric value of $g^{\uparrow\downarrow}$ faces similar challenges as θ and λ.

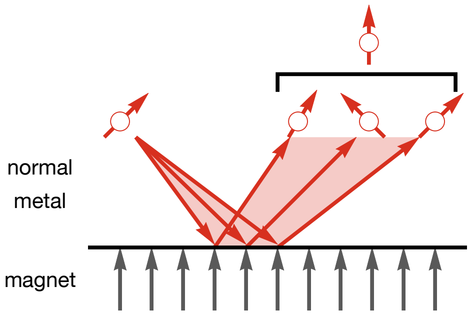

Figure 2.4.: Toy model of the spin transfer torque at the normal metal/magnet interface. The incident spin precesses in the exchange field of the magnetic moments in the magnet which leads to dephasing of the transverse spin component when considering the superposition of all possible scattered electron wave functions. The lost transverse momentum is absorbed by the magnetic lattice where it may either create or annihilate a quantum excitation of the lattice (magnon).

in Ref. [39] or in a more exhaustive fashion in Refs. [45, 46].

In experiment, the application of an external magnetic field allows tuning the magnetization with respect to the spin accumulation spin polarization direction $\boldsymbol{\sigma}_{\mu_s}$, and therefore the magnitude of the torque. For the electrical conductivity of the normal metal two cases need to be considered. When the magnetization is aligned parallel to the spin accumulation spin polarization the torque vanishes, retaining the situation in which the spin accumulation at the interface counteracts the spin Hall effect mediated increase of the resistivity. When magnetization and spin accumulation spin polarization are perpendicular to each other (Fig. 2.4), the spin accumulation partly dissipates into the magnet via the spin transfer torque. Hence, the spin Hall effect induced spin current in the normal metal is not canceled out and contributes to the resistivity of the normal metal as discussed above. In real systems, due to fluctuations, the state at the interface will always be a weighted superposition of the two cases discussed above (Fig. 2.4). Taken together, by application of an external magnetic field one can control the magnitude of the Slonczewski-like torque and thus the rate at which the spin accumulation in the normal metal can be absorbed by the magnet. This enables control of the spin current dissipation channel, i.e. the resistivity of the normal metal via the external magnetic field and is called *spin Hall magnetoresistance* [11, 47, 48]. Since the spin accumulation also depends on the spin transport parameters in the normal metal (λ and θ_{SH}) this spin Hall magnetoresistance is only substantial ($\Delta\rho/\rho \approx 10^{-4}$) in select geometries and materials, e.g.

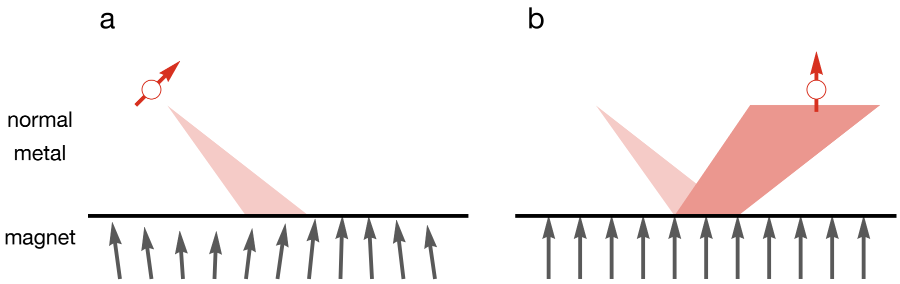

Figure 2.5.: **a** In spin pumping experiments the application of a magnetic field oscillating at the resonance frequency of the magnetization generates a coherent excess magnon population in the magnet. **b** Electrons scattering at the interface will predominantly absorb the quantized excitations of the magnetic lattice (annihilate magnons) via the spin transfer torque.

few nanometer thick Pt films on magnetic insulators.

2.4 SPIN PUMPING

The coupling between the electron spins in the normal metal and the magnetic moments in the magnet via the spin transfer torque also has to be considered in the description of the magnetization dynamics. By accounting for the damping of the motion of the magnetic moments in Eq. (2.2), the Landau-Lifshitz-Gilbert equation [49, 50]

$$\dot{\boldsymbol{m}} = -\gamma\mu_0(\boldsymbol{m} \wedge \boldsymbol{H}_{\mathrm{eff}}) + \alpha\, \boldsymbol{m} \wedge \dot{\boldsymbol{m}}, \tag{2.9}$$

describes the time evolution of the magnetization unit vector in an external magnetic field, where $\boldsymbol{H}_{\mathrm{eff}}$ is the sum of external, exchange and anisotropy magnetic fields and α is a phenomenological damping parameter, which aligns $\boldsymbol{m}$ parallel to $\boldsymbol{H}_{\mathrm{eff}}$ for $t \to \infty$. By explicitly expanding the damping term $(\boldsymbol{m} \wedge \dot{\boldsymbol{m}})$ in Eq. (2.9) under reuse of Eq. (2.9) itself the phenomenological analogy to the spin transfer torque in Eq. (2.8) becomes apparent [38]. Thus, accounting for Slonczewski-like spin transfer torques between the magnet and the normal metal introduces an additional damping channel for the motion of the magnetization [37]. This phenomenon is referred to as *spin pumping* [9].

When the magnetization is in thermal equilibrium magnon annihilation and generation are approximately equally likely and the fluctuations of the magnetization will not generate a spin accumulation in the normal metal. A sizeable spin accumulation can, however, be generated when the magnetization is excited resonantly, e.g. by oscillating magnetic fields.

Assuming a static external magnetic field H_{ext} along the $\boldsymbol{z}$ direction and an oscillating field along the $\boldsymbol{x}$ direction, Kittel [51] derived the magnetization resonance condition as

$$\omega_{\mathrm{res}} = \gamma\mu_0\sqrt{[H_{\mathrm{ext}} + (N_y - N_z)M_{\mathrm{s}}][H_{\mathrm{ext}} + (N_x - N_z)M_{\mathrm{s}}]}, \tag{2.10}$$

where M_{s} is the net (saturation) magnetization of the magnet at a given temperature and the N_i are the dimensionless demagnetization factors which depend on the geometry of the magnet and add up to one. For the common case of a magnetic thin film with H_{ext} in its film plane Eq. (2.10) reads $\omega_{\mathrm{res}} = \gamma\mu_0\sqrt{H_{\mathrm{ext}}[H_{\mathrm{ext}} + M_{\mathrm{s}}]}$.

When the magnet is exposed to an oscillating magnetic field that matches the resonance condition in Eq. (2.10), the magnetization is excited resonantly and a substantial excess magnon population can be generated in the magnet. Electron scattering and spin transfer torque at the interface now become biased towards the magnon annihilation process and generate a spin accumulation and therefore a spin current in the normal metal (Fig. 2.5). Employing the inverse spin Hall effect [Eq. (2.7)] this spin current can also be detected electrically as a voltage drop transverse to the interface normal and the magnetization orientation in the normal metal. One further distinguishes between the AC and DC components of the spin current (voltage), the latter being easier to detect and thus more commonly investigated.

Spin pumping like effects had been observed experimentally earlier [52] but didn't receive much attention until the inverse spin Hall effect was used to electrically detect the associated spin currents [53–55]. Since then, electrically detected spin pumping has been performed in a large variety of materials, including metallic [56, 57], semiconducting [58] and insulating [59] magnets, or even above the magnetization ordering temperature [60].

2.5 SPIN SEEBECK EFFECT

Other than the resonant excitation of the magnetization it is also possible to stimulate spin current emission from or into a normal metal by the broadband excitation of the magnetization in an adjacent magnet. Uchida *et al.* [10] discovered that application of a thermal gradient across the normal metal/magnet interface generates a transverse voltage in the normal metal. Accounting for its origin in the spin accumulation at the interface, the observation was themed *spin Seebeck effect*, in analogy to Thomas Seebeck's findings almost 200 years before [61]. Albeit significant theoretical and experimental progress since, details of the theoretical interpretation of these results are still vividly debated [12, 62–69]. Much of the discussion revolves around the composition and origin of the magnon accumulation at the interface. From experiment it was inferred that the magnitude of the effect is nontrivially connected to saturation [70] and sublattice [71] magnetization of the host magnet and it was argued [72] that the rel-

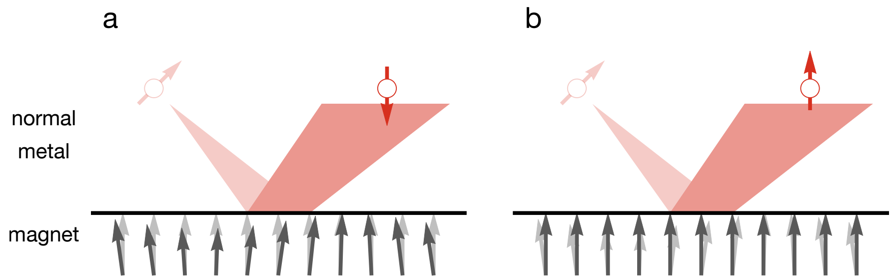

Figure 2.6.: **a** When the magnet is at a lower effective temperature than the normal metal magnon generation, i.e. the excitation of dynamics in the magnetic lattice, is the dominant scattering process. This creates a spin accumulation polarized antiparallel to the magnetization at the interface. **b** In the opposite case, when the magnet is at a higher effective temperature than the normal metal, most scattering processes annihilate magnons, generating a spin accumulation in the normal metal which is polarized parallel to the magnetization. In thermal equilibrium both processes are equally likely and no spin accumulation emerges.

evant magnon accumulation is dominated by low-energy magnons. Regardless of these open points, however, the spin transfer between the normal metal and the magnet is expected to obey the principles outlined in the previous sections.

Xiao *et al.* [12] investigated the spin pumping from a broad magnon spectrum and developed a theory formulated in terms of deviations from thermal equilibrium. Thermal equilibrium thereby refers to equality between the electron temperature in the normal metal and the magnon temperature in the magnet. Within this framework, the magnon temperature measures the magnon population at the interface, but does not necessarily have to reflect an actual physical temperature, i.e. when the magnetic excitations are not in thermal equilibrium with the lattice. Assuming this is the case, however, the laws of thermodynamics allow for a formulation in terms of the heat equation which permits a relatively convenient, classical and macroscopic treatment of the problem. Potential issues with this approach are discussed in more detail in Ch. 5.1. To attain thermal equilibrium or a steady state, temperature differences are then harmonized out by appropriately balancing magnon generation (injecting energy into the magnet) or annihilation (taking energy from the magnet) processes.

When the magnet is situated at a lower temperature compared to the normal metal (Fig. 2.6a) spin transfers that generate additional magnons in the magnet are more likely than those that decrease the number of magnons. This generates a spin accumulation at the interface between the magnet and the normal metal, which in turn generates a spin current between the two.

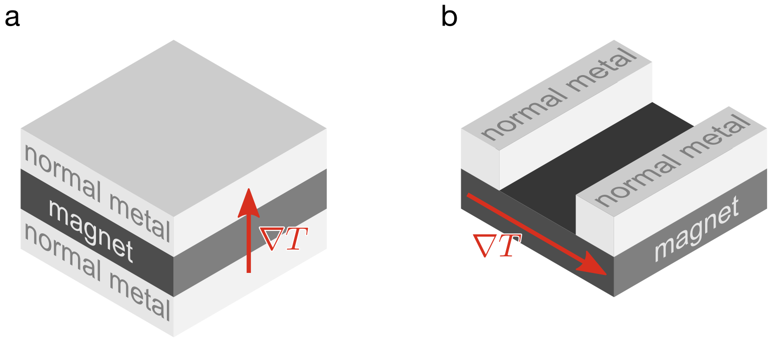

Figure 2.7.: **a** In the longitudinal spin Seebeck configuration the thermal gradient is applied along the interface normals. **b** For the transverse configuration the thermal gradient lies in the film plane of the magnet, with several separate, thin Pt strips patterned on top.

Conversely, when the magnet is at a high temperature, corresponding to a large magnon population (Fig. 2.6b), the situation is reversed. Spin transfer processes that decrease the number of magnons now dominate the interface scattering. The spin accumulation and its associated spin current in this case are now polarized in the opposite direction compared to the previous situation.

In thermal equilibrium magnon generation and annihilation are equally likely and no spin accumulation emerges for the vanishing net spin transfer across the interface.

The configuration described above, with the thermal gradient aligned parallel to the interface normal (Fig. 2.7a) is also referred to as *longitudinal* (spin Seebeck) configuration. In contrast, Uchida *et al.* had originally [73, 74] proclaimed observation of the effect for a thermal gradient in the film plane, i.e. *transverse* to the interface normal (Fig. 2.7b). From the viewpoint of the theoretical framework outlined above, the configurations depicted in Fig. 2.7 are identical, however, recent findings [75–77] suggest that the characteristic length scale to be micrometers rather than millimeters as reported by Uchida *et al.*. This explains why subsequent studies [15, 78] could not reproduce these findings.

For this reason the longitudinal configuration is now employed almost exclusively in experiments. Unfortunately, it is prone to contamination via the anomalous Nernst effect that generates a thermal voltage with largely identical symmetry with respect to external magnetic fields. The use of insulating magnets in most experiments today avoids this issue, although a careful choice of material combinations or fabrication conditions or both [79–82] is still required to unequivocally prevent contamination by spurious voltage signals.

3

SPINTRONICS ON INSULATING MAGNETIC MATERIALS

The strength of the magnetic field generated by magnetic insulators (the saturation magnetization) is typically smaller than that generated by the elementary ferromagnets Fe, Co and Ni. This diminishes the practical use of the former for many applications but yields some interesting benefits for others.

The redeeming quality of the ferrimagnetic insulator yttrium iron garnet ($Y_3Fe_5O_{12}$, YIG) is its extremely low magnetization damping that makes it very well suited for microwave applications. YIG, first synthesized in the 1950s [83, 84], has been intensively investigated in the subsequent decades [22], however, interest diminished when spin dependent (electron) transport in the solid state was popularized by the discovery of the giant magnetoresistance [85, 86] in the late 1980s. (Semi-)Conducting magnets today form the basis for most commercial applications in which spin effects are utilized, such as hard disk read heads or magnetic random access memory. They further profit from the availability of sophisticated fabrication techniques that make production of high quality, nanometer scale devices relatively straight forward.

YIG is a synthetic garnet and does not occur naturally on earth.

The interest in YIG was renewed, however, by the advent of pure spin currents, triggered by the realization of the spin Hall effect, spin pumping and other pure spin current generation schemes. YIG here allows to separate the electric from the magnetic components of a device in an elegant fashion. Not without its own challenges, the absence of mobile charge carriers in YIG allows for an easier, in some sense cleaner and thus more robust, interpretation of experimental data as already discussed in Ch. 2.5.

The crystal structure of yttrium iron garnet is fairly complicated with 80 atoms in the unit cell (lattice constant $a_{\mathrm{YIG}} = 12.376\,\text{Å}$). The Curie temperature T_C is commonly given as 560 K [22], however the value $T_C = 550\,\mathrm{K}$ is also reported in literature [90]. The color of large specimen is black due to the small but non negligible light absorption [91, 92] in the visible spectrum. Thin films or very small specimen, on the other hand, are transparent and exhibit a yellowish [93, 94] (see also Fig. 3.1) or greenish [94, 95] tint. The optical properties in particular differ significantly between publications [91, 96]

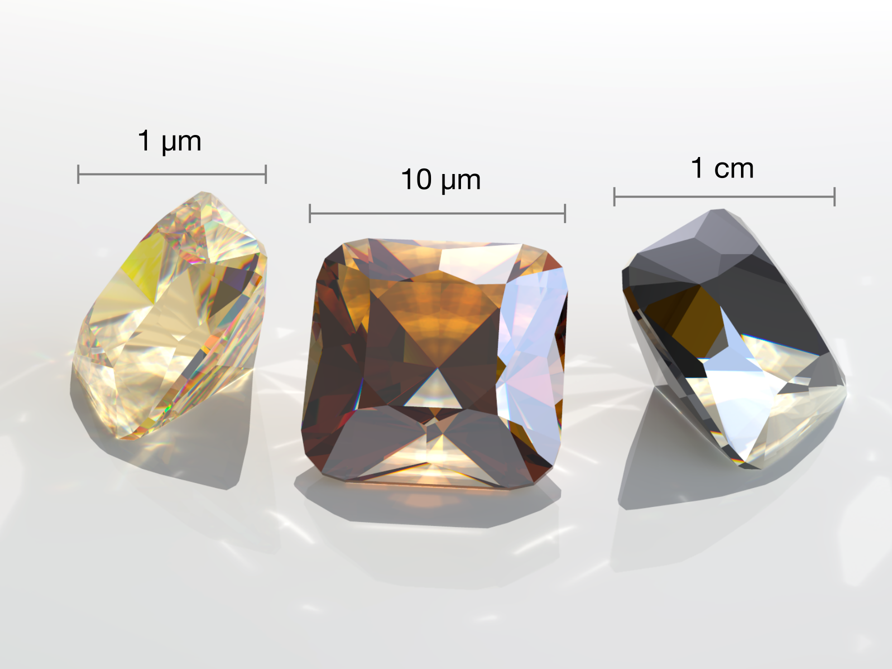

Figure 3.1.: 3D rendered YIG crystal gemstones of various sizes. Image generated using POV-Ray [87] and the *spectral rendering using POV-Ray* scripts [88], employing the refractive index data from Ref. [89].

which might root in varying impurity concentrations as obtained by different growth methods [91].

The magnetization of bulk YIG crystals is reported as $M_\mathrm{s} \cong 140\,\mathrm{kA/m}$ [97] along with a magnetization damping of the order of $\alpha \approx 10^{-4}$ or even lower [98]. The YIG films grown at the Walther-Meißner-Institut have been optimized foremost for crystalline quality and typically feature magnetization values smaller by up to 30% than the one given above. As a consequence of ongoing optimization efforts, however, values between individual specimen can differ substantially. This is also true for the magnetization damping that routinely takes values of the order of 10^{-3} [99].

The vast majority of samples investigated in this thesis are yttrium iron garnet thin films, capped with a few nanometer thick platinum layer. The YIG thin films are grown on [111] oriented gadolinium gallium garnet (GGG) or yttrium aluminium garnet (YAG) substrates by means of pulsed laser deposition at the Walther-Meißner-Institut. To guarantee high interface quality the Pt layers are deposited on the YIG films, *in-situ*, without breaking the vacuum, by electron beam evaporation. YIG samples have kindly been provided by Stephan Geprägs, Sibylle Meyer, Matthias Althammer, Michaela Lammel and Stephan Altmannshofer. For detailed reports on the sample fabrication process the reader is referred to Refs. [48, 81, 99–101].

4

ROTATING MAGNETIC FIELDS FOR SPINTRONICS MEASUREMENTS

Measurements of the spin Hall magnetoresistance, like many other spin current based phenomena, need to be conducted under precisely controlled environmental conditions, that minimize the drift of the ambient temperature, as well as electromagnetic noise or cable length, to name only a few parameters that need to be considered for accurate results. In the yttrium iron garnet/platinum samples featured prominently in this thesis the temperature coefficient of the metallic layer, i.e. the relative change of the resistivity per Kelvin, is of the order of 10^{-3} [102], while the resistivity modification attributed to the spin Hall magnetoresistance attains this value only under ideal conditions [11, 47, 48] but is typically (much) smaller. The characteristic signature of the effect is then often masked by a temperature drift induced resistivity change. The issue is amplified by long measurement times (in excess of an hour), as dictated by the experimental setup. Similar issues have to be faced in spin pumping and spin Seebeck effect experiments where the signals of interest quite often do not exceed a few hundred nanovolts which puts the detection equipment to the extreme limits of its sensitivity range.

This chapter presents a novel method for highly accurate measurements of any effect whose magnitude is tied to the relative orientation of an external magnetic field with respect to some particular axis. The new measurement method in addition is much faster than conventional measurement methods, with the values of interest available within few seconds to about a minute, instead of upwards of an hour for cryostat based measurements. In particular, the chapter will focus on the spin Hall magnetoresistance, but the approach can also be applied to a large variety of other phenomena. The method is based on the continuous modulation of the effect magnitude by means of transient, rotating magnetic fields and detection based on Fourier analysis. In essence, the method employs a modulation spectroscopy [103, 104] approach to grant a more direct access to the quantities of interest. For the experiments a custom built benchtop rig, incorporating a high field permanent magnet is utilized, for the mechanical design and construction of which the author is indebted to

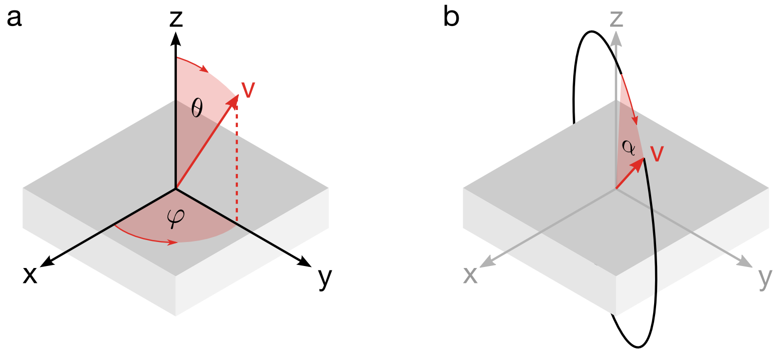

Figure 4.1.: **a** The (conventional) polar angles φ and θ measure the angle between a vector $\boldsymbol{v}$ (red) and the $\boldsymbol{x}$ axis in the plane spanned by $\boldsymbol{x}$ and $\boldsymbol{y}$ and the angle between $\boldsymbol{v}$ and $\boldsymbol{z}$, respectively. **b** The angle α measures the angle between $\boldsymbol{v}$ and an arbitrary axis in an arbitrary plane.

Thomas Brenninger and the workshop team at the Walther-Meißner-Institut.

4.1 MATHEMATICAL CONCEPT

The magnitude of spin current based effects, by virtue of spin Hall effect and spin transfer torque (Ch. 2.2, Ch. 2.3), can often be controlled by the relative orientation between an applied magnetic field and a characteristic direction given by the sample design. Consider a thin film sample in the xy-plane as depicted in Fig. 4.1. The voltage V_x arising along the $\boldsymbol{x}$ direction can be decomposed into its Fourier coefficients

$$V_x = \sum_{i=0}^{\infty} V_i(\theta, \varphi) = \sum_{i=0}^{\infty} V_i(\alpha), \tag{4.1}$$

Fundamentally, α may also be the curve parameter of some closed curve.

where the second equality holds when considering the variation of the external magnetic field orientation in a given plane. In that case the angle α is a (potentially complicated) function of the conventional polar angles θ and φ. Experimentally Eq. (4.1) is typically verified by performing a series of measurements with the external magnetic field $\boldsymbol{H}_{\mathrm{ext}}$ at angles α_i and subsequently fitting the data with the expected modulation with respect to $\alpha\ (\theta, \varphi)$. As each measurement point $V_x(\alpha_i)$ typically takes several seconds to record, even a measurement in only a single plane will take several minutes to upwards of an hour to complete, depending on the number of measurement points, field strength H_{ext}, and the magnet equipment used for the experiment, not including any additional time required to achieve a thermally stable state as discussed above. The long time required per measurement point is largely determined by the time required by the magnet to stabilize from its initial orientation α_i to another orientation α_j and the condition $\partial_t \boldsymbol{H}_{\text{ext}} = \boldsymbol{0}$ during the actual voltage measurement as to exclude contamination by electromagnetic induction (Faraday's law [105]). Neglecting the later issue for a brief moment, much shorter measurement times can be achieved if $\boldsymbol{H}_{\text{ext}}$ is rotated steadily rather than stepwise with measurements taken continuously during the rotation. Mathematically it is then convenient to first transform Eq. (4.1) to the time domain, i.e. $\alpha \to \alpha(t) = \omega t$. The accordingly adjusted Eq. (4.1) reads

$$V_x(t) = \sum_{i=0}^{\infty} V_i(t). \tag{4.2}$$

Expanding Eq. (4.2) in terms of its harmonic frequency components yields

$$V_x(t) = V_0 + V_1 \sin[\omega t + \Phi_1] + V_2 \sin[2(\omega t + \Phi_2)] + \cdots, \tag{4.3}$$

where it is convenient, but not required for a later analysis of experimental data, to chose the Φ_i such that $V_i > 0$. A series of data points $V_x(t_j)$ can thus be analyzed in terms of the harmonics of ω to obtain the individual series coefficients V_i. In experiment this can be achieved conveniently by a lock-in amplifier. Even for relatively small ω of the order of 1 Hz, in a short time, the lock-in averages over many more rotation periods and at substantially higher sampling rates than what is conceivable by the conventional, field-orientation stepping approach. As an added benefit, the short time required for a measurements reduces thermal drift significantly which also enables measurements under less than ideal environmental conditions.

To investigate the significance of the V_i in Eq. (4.3) a comparison to an actual physical effect is adequate. In the spin Hall magnetoresistance, a current driven along $\boldsymbol{x}$ will generate a voltage drop V_{xx} along the same direction. In coordinates of Fig. 4.1a, V_{xx} reads [47, 48]

$$V_{xx} = V_{xx,0} + \Delta V \sin^2 \varphi \sin^2 \theta. \tag{4.4}$$

For a continuous rotation of $\boldsymbol{H}_{\text{ext}}$ in the xy-plane ($\theta = \pi/2$) Eq. (4.4) can be written as

$$V_{xx} = V_{xx,0} + V_{\text{ind}} \sin(\omega t + \Phi_{\text{ind}}) + \Delta V \sin^2(\omega t + \Phi_{\Delta V}), \tag{4.5}$$

where V_{ind} accounts for the electromagnetic induction ($V_{\text{ind}} \propto \partial_t H_{\text{ext}}$) and Φ_{ind} and $\Phi_{\Delta V}$ depend on the offset between φ and α with $\Phi_{\Delta V} = 0$ when $\alpha(t) = \varphi(t)$. Employing the trigonometric identity $\sin^2 x = \frac{1}{2} - \frac{1}{2}\sin(2x + \pi/2)$ and sorting terms, Eq. (4.5) can be reformulated as

Φ_{ind} is highly dependent on details of the setup design and can be considered arbitrary for the discussion here.

$$\begin{aligned} V_{xx} = &+ V_{xx,0} + \frac{\Delta V}{2} \\ &+ V_{\text{ind}} \sin(\omega t + \Phi_{\text{ind}}) \\ &+ \frac{\Delta V}{2} \sin[2(\omega t + \Phi_{\Delta V} + \pi/4)]. \end{aligned} \tag{4.6}$$

The variation of V_{xx} with 2ω (hereafter referred to as the second harmonic) is thus directly proportional to ΔV and not contaminated by the spurious inductive signal. This only holds, however, when $\boldsymbol{H}_{\text{ext}}$ can be considered homogenous across the sample volume and the electrical supply lines. In general, V_{ind} will also leak into all higher harmonics but at a much reduced magnitude for reasonably homogeneous magnetic fields. Some further measures can also be taken to reduce or even remove V_{ind} in *all* relevant harmonics as is discussed in the remainder of this section.

When the homogeneity of $\boldsymbol{H}_{\text{ext}}$ can not be guaranteed or the effect to be investigated is itself expected to be dominant in the first harmonic of ω, the simplest approach is to scale either V_{ind} or the effect magnitude ΔV with respect to each other. Since $V_{\text{ind}} \propto \partial_t H_{\text{ext}}$, it is a function of ω as well and can be scaled in magnitude by changing the field rotation frequency ω. ΔV being unaffected by this change an extrapolation to $\omega = 0$ from a series of measurements at different ω can be employed to separate ΔV from V_{ind}. The same can be achieved when it is possible to change the magnitude of ΔV by a second parameter, e.g. the applied current in a spin Hall magnetoresistance measurement.

The scaling works regardless of the specific harmonic ΔV is proportional to.

The above constitutes the main idea of the suggested measurement approach. Before discussing some remaining mathematical details, a further generalization is conceptualized.

In some cases, e.g. when V_{ind} vastly dominates ΔV, the scaling approach proposed above may not suffice to identify the absolute value of ΔV. An alternative approach then is to imprint a second periodic modulation onto ΔV, via tuning of another parameter ΔV is dependent on. In this case all of Eq. (4.4) is multiplied by a factor $\sin(\omega_{\text{mod}} + \Phi_{\text{mod}})$ and by exploiting the trigonometric identity $\sin x \sin y = \frac{1}{2}[\cos(x-y) - \cos(x+y)] = \frac{1}{2}[\sin(x-y+\pi/2) - \sin(x+y+\pi/2)]$ as well as accounting for the electromagnetic induction the equivalent of Eq. (4.6) reads

$$\begin{aligned} V_{xx} = &+ (V_{xx,0} + \frac{\Delta V}{2}) \sin(\omega_{\text{mod}} t + \Phi_{\text{mod}}) \\ &+ V_{\text{ind}} \sin(\omega t + \Phi_{\text{ind}}) \\ &+ \frac{\Delta V}{4} \sin[(2\omega - \omega_{\text{mod}})t + (2\Phi_{\Delta V} - \Phi_{\text{mod}}) + \pi] \\ &+ \frac{\Delta V}{4} \sin[(2\omega + \omega_{\text{mod}})t + (2\Phi_{\Delta V} + \Phi_{\text{mod}}) + \pi]. \end{aligned} \tag{4.7}$$

Notably, V_{ind} is unaffected by the additional modulation of ΔV. Higher order terms of V_{ind} ($\propto \sin 2\omega, \sin 3\omega, \dots$) are thus at fundamentally different frequencies than ΔV, detected at either $2\omega - \omega_{\text{mod}}$ or $2\omega + \omega_{\text{mod}}$. A more interesting case for this double modulation scheme than the spin Hall magnetoresistance covered in Eq. (4.7), is when the desired quantity itself is proportional to $\sin \omega$ before

provided $\omega_{\text{mod}} \neq \omega$

accounting for ω_{mod} (e.g. spin Seebeck effect, spin pumping, or spin Hall magnetoresistance in the presence of uniaxial magnetic anisotropy). The detection frequency then analogously transforms to $\omega \pm \omega_{\text{mod}}$. While straightforward mathematically, this procedure adds some complexity experimentally in requiring detection and data analysis at the mixed frequencies. This method is employed for some of the data acquisition in Ch. 5.2.

Returning to the points left open in the initial discussion of the rotating field scheme, the significance of the phases Φ_i and the constant fractions of π adding to the total phase have to be clarified. In short, the sign of ΔV or the angle α that maximizes $\Delta V(\alpha)$ is encoded in these parameters. A trivial example is when $V_{\text{ex}} = \Delta V \cos\varphi$ with a rotation of $\boldsymbol{H}_{\text{ext}}$ in the xy-plane and $\boldsymbol{H}_{\text{ext}}(t=0) \parallel \boldsymbol{x}$. Then $\alpha(t) = \varphi(t)$, i.e. $\Phi_{\Delta V} = 0$, and $V_{\text{ex}} = \Delta V \sin(\omega t - \pi/2)$. The total phase of $-\pi/2$ signifies the rising slope zero crossing of $V_{\text{ex}}(\varphi)$ at $\varphi = -\pi/2$ and thus a maximum of V_{ex} at $\varphi = 0$. Experimentally the relation between $\alpha(t)$ and $(\varphi, \theta)(t)$ depends on details of the implementation and has to be derived for the particular measurement configuration at hand. In experiments the phase Φ_i in particular is sensitive to contamination via spurious signals. However, by shifting Φ_i by π (e.g. by inverting the current in a spin Hall magnetoresistance measurement), the true phase can be recovered by comparing the measured phase values with and without the intentional phase shift.

Taken together the parameters V_i and Φ_i represent the complex (magnitude and phase) Fourier coefficients of V_x in Eq. (4.2) and (4.3) and can, in principle, reconstruct any $V_x(\alpha)$, e.g. when strong anisotropy distorts the modulation of $V_x(\alpha)$. Factors limiting the precision of the method, besides the usual sources of noise, include the dynamic range of the detection device, irregular ω and ω_{mod} and potentially a nonlinear feedback between effect magnitude and the electromagnetically induced voltages.

4.2 EXPERIMENTAL REALIZATION

The perhaps most challenging part of the implementation of the method outlined above is the generation of the continuously rotating magnetic field $\boldsymbol{H}_{\text{ext}}$. As mentioned above, superconducting magnets employed in e.g. cryostats are most often restricted to rather small $\partial_t H_{\text{ext}}$, resulting in very small ω (far below 1 Hz). Conventional, resistive magnets can be driven much faster, but generally produce smaller fields, in particular at large ω due to the inductive reactance of the magnet coils. Fundamentally, however, a pair of resistive coils is well suited to provide the rotating field, provided the magnetic samples of interest have low enough coercive and anisotropy fields.

The inductive reactance of coils can be compensated for by a capacitor connecter in series.

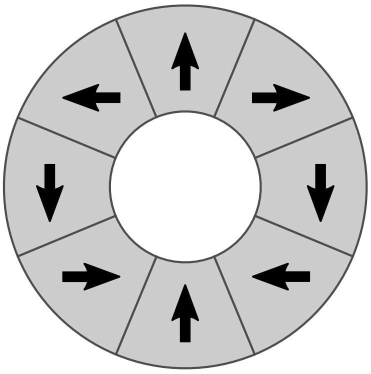

Figure 4.2.: Cross section through an eight segment circular Halbach array in dipole configuration. The arrows indicate the magnetization direction of each cylinder segment.

Unfortunately shape anisotropy in magnetic thin films easily exceeds an equivalent of 100 mT when the magnetic field $\boldsymbol{H}_{\text{ext}}$ also is to be rotated normal to the film plane. A solution to this problem was provided by Halbach [106], who elaborated on a phenomenon first discussed by Mallinson [107] and laid out designs for permanent magnet arrays with very high field homogeneity and strength. By magnetizing and arranging a set of cylinder segments in a particular fashion various highly symmetric field configurations can be achieved. The particular configuration depicted in Fig. 4.2 generates a large and very homogenous radial magnetic field in the inside of the cylinder while the magnetic field on the outside of the cylinder is largely suppressed. The field in the center of a N-segment circular Halbach array in this dipole configuration is given by [108]

$$\begin{aligned} |B_{\text{center}}| &= \frac{\sin(\frac{2\pi}{N})}{\frac{2\pi}{N}} B_{\text{r}} \left[\log(r_{\text{out}}/r_{\text{in}}) - \Delta\right], \qquad (4.8) \\ \Delta &= \frac{l_0}{2\sqrt{l_0^2 + r_{\text{out}}^2}} - \frac{l_0}{2\sqrt{l_0^2 + r_{\text{in}}^2}} + \log\left(\frac{l_0 + \sqrt{l_0^2 + r_{\text{out}}^2}}{l_0 + \sqrt{l_0^2 + r_{\text{in}}^2}}\right), \end{aligned}$$

where B_{r} is the remanent magnetic field of the cylinder shell material, $l_0 = l/2$ with the length l of the cylinder, r_{in} and r_{out} are the inner and outer radius of the cylinder shell, respectively. The factor Δ corrects for the finite length of the cylinder and vanishes in the limit $l_0 \to \infty$. Circular Halbach arrays with inner radii r_{in} as large as $r_{\text{in}} = 25\,\text{cm}$ at $B_{\text{center}} = 1\,\text{T}$[1] or with field field strengths exceeding 4 T [109] ($r_{\text{in}} = 6\,\text{mm}$) and 5 T [110] ($r_{\text{in}} = 2\,\text{mm}$) have been built using NdFeB, SmTe or SmCo based permanent magnets. For practical purposes,

---

[1] *Shin-Etsu develops the world's largest-class permanent magnet-type magnetic circuit* (April 8, 2008). Retrieved November 11, 2015, from https://www.shinetsu.co.jp/en/news/archive.php?id=156

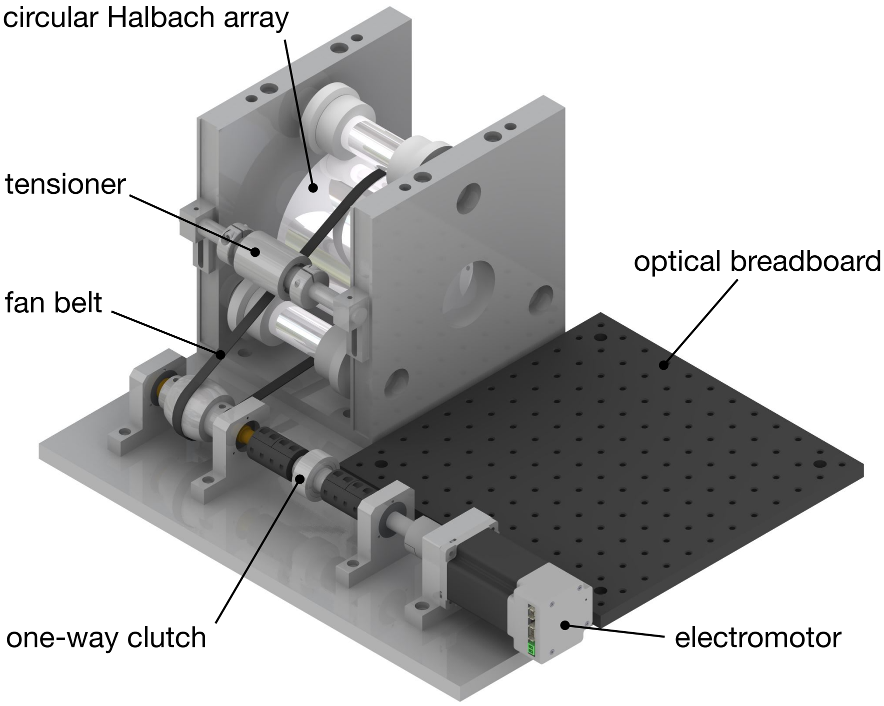

Figure 4.3.: Rotating Halbach cylinder assembly. CAD model kindly provided by Thomas Brenninger.

however, high field strengths and large r_{in} have to be balanced with size and weight of the magnet.

For the realization of the rotating magnetic fields in the following a circular, 8 segment Halbach array built from N45 grade NdFeB ($B_{\mathrm{r}} = 1.32\,\mathrm{T}$) with $r_{\mathrm{in}} = 20\,\mathrm{mm}$ and an outer diameter $r_{\mathrm{out}} = 55\,\mathrm{mm}$ at a length $l = 100\,\mathrm{mm}$ has been integrated into a custom built mechanical rotation stage. It provides an experimentally verified maximum field strength $B_{\mathrm{max}} = 1.15\,\mathrm{T}$, in good agreement with the theoretically expected value of $B_{\mathrm{center}} = 1.14\,\mathrm{T}$ obtained by inserting the parameters above into Eq. (4.8). Given the maximum shape anisotropy of yttrium iron garnet of $\mu_0 M_{\mathrm{s}} \approx 175\,\mathrm{mT}$ (almost) parallel orientation of external magnetic field and sample magnetization are guaranteed for rotations in any plane.

As depicted, in Fig. 4.3 the Halbach cylinder is fixed between three rollers and driven by an electric motor, to which it is connected by a fan belt via a gear rod. The motor speed can be tuned continuously via a PC interface. At full speed the Halbach cylinder rotates with a frequency of $\omega \approx 6\,\mathrm{Hz}$. Access to the inside of the cylinder is possible from both sides, allowing for e.g. laser illumination of a specimen placed inside the cylinder.

A sample holder (Fig. 4.4) has been designed to accept specimens

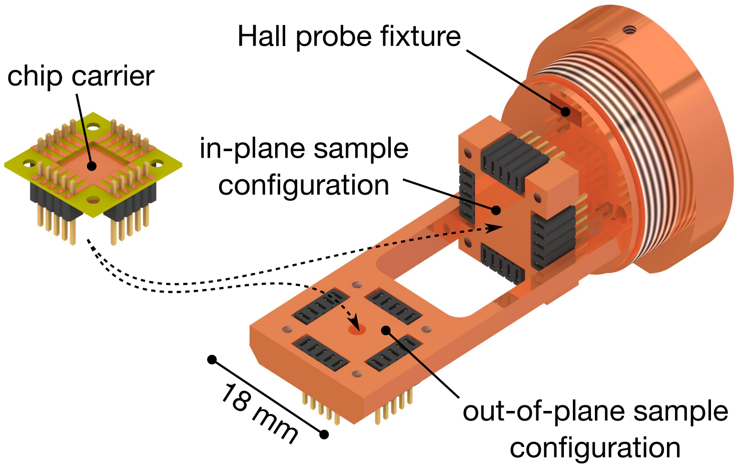

Figure 4.4.: Chip carrier and sample holder for use in the Halbach benchtop setup. Parts of the CAD model were kindly provided by Mathias Althammer and Thomas Brenninger.

mounted onto 20 pin chip carriers which can be placed in such a manner as to allow to rotate the magnetic field in three perpendicular planes. The sample holder also includes a fixture in which a Hall probe can be placed. The Hall probe provides a reference signal for the data acquisition via a lock-in amplifier.

4.3 EXPERIMENTAL RESULTS

Test measurements on two YIG/Pt samples were made to test the benchtop setup and verify the mathematical procedures outlined in Ch. 4.1. Both samples are patterned into Hall bar mesa structures with dimensions $80\,\mu\text{m} \times 950\,\mu\text{m}$ of the central bar. The spin Hall magnetoresistance hereby serves as the test effect for the data acquisition. The quantities of interest here are the spin Hall magnetoresistance magnitude $\Delta\rho/\rho$, as well as the magnetic field angles (φ, θ) that maximize ρ. Measurements are performed using a constant current source and a lock-in amplifier (Stanford Research SR830) with differential input to perform four terminal voltage (resistance) measurements. A multimeter, connected in parallel to the lock-in amplifier, measures the constant voltage drop ($\equiv \rho$), while the lock-in measures the variation of the voltage drop ($\equiv \Delta\rho$) at the second harmonic of the magnetic field rotation frequency. While the measured $\Delta\rho$ will always be positive due to the lock-in detection setting of magnitude and phase, the angles $(\varphi_{\text{max}}, \theta_{\text{max}})$ can be employed to determine the sign of $\Delta\rho$ in Eq. (4.5) as described above. For illustration purposes quite a large number of measurements for each particular sample and field configuration will be recorded here. The analysis will show, however, that one or two measurement

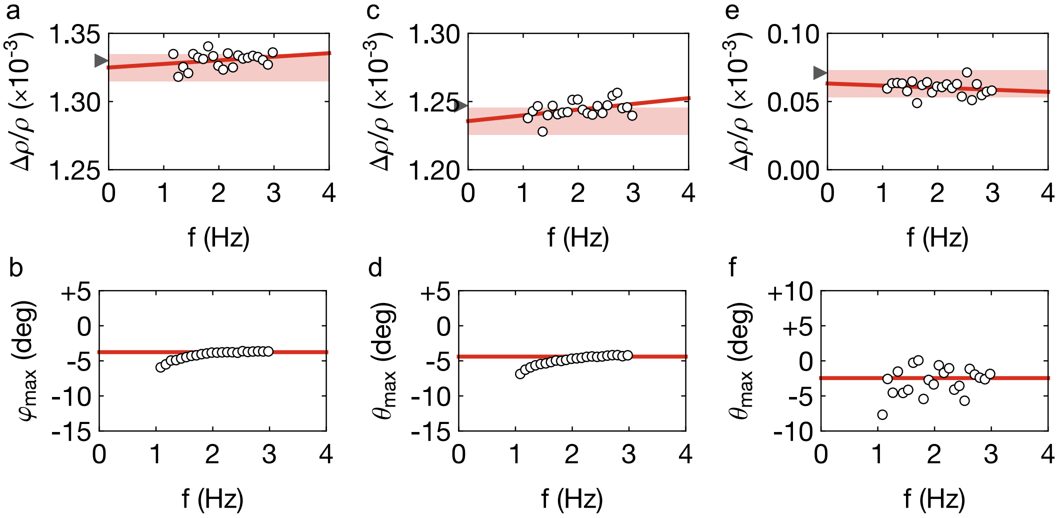

Figure 4.5.: **a** Magnitude of the spin Hall magnetoresistance $\Delta\rho/\rho$ in a 3 nm thick Pt film on YIG as determined from field rotations in the sample plane. The solid line is a linear interpolation of the data points and the shaded region indicates an error of $\pm 10^{-5}$ in $\Delta\rho/\rho$ for comparison. The gray triangle indicates the $\Delta\rho/\rho$ value as obtained by the conventional, field-orientation stepping method. **b** Corresponding angle $\varphi_{\max}$ that maximizes $\rho(\varphi)$, determined from the phase value by combining data for $+1$ mA and -1 mA applied current. The solid line indicates the average of the values $\varphi_{\max}(f) > 2$ Hz. **c,d** Values analogously determined for a rotation of the magnetic field in the plane perpendicular to the current. **e,f** Values analogously determined for a rotation of the magnetic field in the plane spanned by current direction and film normal.

points should generally suffice to yield robust results.

The first sample is a 64 nm thick YIG film covered by a 3 nm thin Pt layer, such that a spin Hall magnetoresistance magnitude $\Delta\rho/\rho$ of around 1.3×10^{-3} [48] can be expected. Figures 4.5a,b show the results of rotations of the magnetic field in the film plane, i.e. $\theta = 90°$ and $\varphi \rightarrow \varphi(t)$ in Eq. (4.4), at different field rotation frequencies f and an applied current of 1 mA. Slightly varying with the magnetic field rotation frequency the ratio $\Delta\rho/\rho$ shown in Fig. 4.5a is measured as approximately 1.31×10^{-3} when extrapolated to zero frequency. The shaded region is a $\pm 1 \times 10^{-5}$ region around the extrapolated value. All data points lie within this margin. Considering that the shaded region constitutes an error of about 1%, this demonstrates that a even a single measurement would be sufficient to determine $\Delta\rho/\rho$ with very reasonable precision. For the lock-in amplifier settings employed in the measurement (time constant: 3 s, roll off: 24 dB/oct) a single data point takes about 45 s to record. Using larger rotation frequencies allows to decrease the value of the time constant, which would further accelerate the measurement. The phase values converted to the angle $\varphi_{\max}$ that maximizes $\rho(\varphi)$ are shown in

Fig. 4.5b. To identify and eliminate the influence of spurious voltages the measurements were performed for both positive and negative currents and averaged subsequently. This eliminates, to first order, any discrepancy caused by the inductive contributions to the voltage signal. Immediately apparent is the drop in $\varphi_{\max}$ for $f \lesssim 2\,\mathrm{Hz}$ which appears to be an issue with the lock-in amplifier as it is present also in all subsequent measurements. When only considering the values above 2 Hz the resulting $\varphi_{\max}$ takes a value of about $-3.7°$, which can be attributed to the mechanical misalignment between the Hall probe providing the reference signal and the current path on the sample. Set aside the small misalignment this value requires ΔV ($\Delta\rho$) in Eq. (4.4) to be negative, which is indeed the case for the spin Hall magnetoresistance [11, 47, 48].

Magnitude and phase as obtained from rotations of the magnetic field in the plane perpendicular to the current direction [$\varphi = 90°,\ \theta \to \theta(t)$] are shown in Fig. 4.5c and Fig. 4.5d, respectively. The dependence on the magnetic field rotation frequency remains small also in this configuration, but surprisingly only reaches a value of $\Delta\rho/\rho = 1.24 \times 10^{-3}$, which is indicative of notable anisotropy in this particular sample. This point is expanded on later in the chapter. At any rate, the $\Delta\rho/\rho$ ratio is still maximized at a field angle $\theta_{\max} = -4°$ close to zero. It should be noted that, in principle, also the mechanical misalignment alone can cause a reduced $\Delta\rho/\rho$ by a rotation of the magnetic field in an irregular plane which then appears as "anisotropy" in the measurement. However, in several measurements with intentionally magnified misalignment a reduction as significant as observed here could not be reproduced.

The last field rotation plane spanned by current direction and film normal yields a finite $\Delta\rho/\rho$ ratio of 0.06×10^{-3} as shown in Fig. 4.5e, which is unexpected from Eq. (4.4), but qualitatively consistent with the notion of anisotropy in this particular sample. The voltage maximizing field angle is about $-2.5°$. Since $\Delta\rho/\rho$ does not show a pronounced dependence on the field rotation frequency, i.e. is not purely a consequence of electromagnetic induction, this field angle does indeed contain information on $\rho(\varphi, \theta)$.

This is unlike the second sample (Fig. 4.7) discussed below.

An unexpected anisotropy that leads to a deviation from the behavior described by Eq. (4.4) will introduce higher order terms in $\rho(\varphi, \theta)$. For symmetry reasons the anisotropy may only appear at integer multiples of 2ω in Eq. (4.4), i.e. in the 4ω, 6ω, ... signals. However, all but the values of the first harmonic $\Delta\rho^{4\omega}/\rho$ shown in Fig. 4.6 for the field rotating in the plane perpendicular to the current direction are below the noise floor in the experiment. Correcting for the moderate dependence on the rotation frequency $\Delta\rho^{4\omega}/\rho$ is obtained as 0.12×10^{-3} under an angle $\theta^{4\omega}_{\max} = -4.2°$. The finite value here supports the notion that notable magnetic anisotropy is present

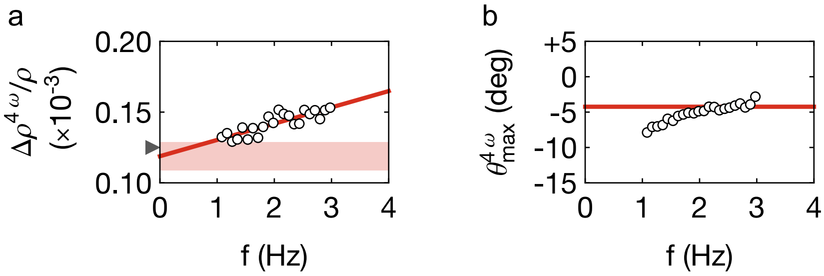

Figure 4.6.: **a** First harmonic $\Delta\rho^{4\omega}/\rho$ of the magnitude of the spin Hall magnetoresistance in a 3 nm thick Pt film on YIG as obtained from magnetic field rotation in the plane perpendicular to the current direction. **b** Corresponding phase data.

in this particular sample. These findings are further backed by a comparison with the $\Delta\rho/\rho$ values as obtained by the conventional method (gray triangles in Figs. 4.5 and 4.6), kindly provided by Sibylle Meyer.

In principle, the extracted $\Delta\rho/\rho$ and $\varphi(\theta)_{\mathrm{max}}$ values could also be used to quantitatively determine the magnetocrystalline anisotropy constants of a particular sample. To this end a simulation of the equilibrium magnetization orientation based on a free energy ansatz (e.g. Refs. [101, 111]) can be performed and compared with the experiment. This, however, is beyond the scope of this chapter.

The same set of measurements has also been performed on a sample with a thicker Pt layer (12.8 nm) resulting in a smaller magnitude $\Delta\rho/\rho$ of the spin Hall magnetoresistance. Another factor to take into account here is that the absolute voltage levels on this sample are only moderately larger than the inductive signal. The results of field rotations in the film plane, shown in Fig. 4.7a show a small slope in the $\Delta\rho/\rho$ data, which when extrapolated to zero frequency yields a value of $\Delta\rho/\rho = 2 \times 10^{-4}$. All data points lie within the $\pm 10^{-5}$ margin around the extrapolated value. The phase data shown in Fig. 4.7b show the same drop below $f \approx 2\,\mathrm{Hz}$ but are otherwise constant due to the combination of measurements with positive and negative applied current. As expected, φ_{max} is in the vicinity of zero, however, the mechanical alignment mismatch is slightly larger in this sample.

The field rotations in the plane perpendicular to the current (Fig. 4.7c,d) show a significantly stronger influence on the rotation frequency, which indicates that the sample holder in this position is much more prone to electromagnetic induction. The extrapolation to zero, however, yields almost the same value as for the field rotation in the film plane. The minor difference is explained by measurement

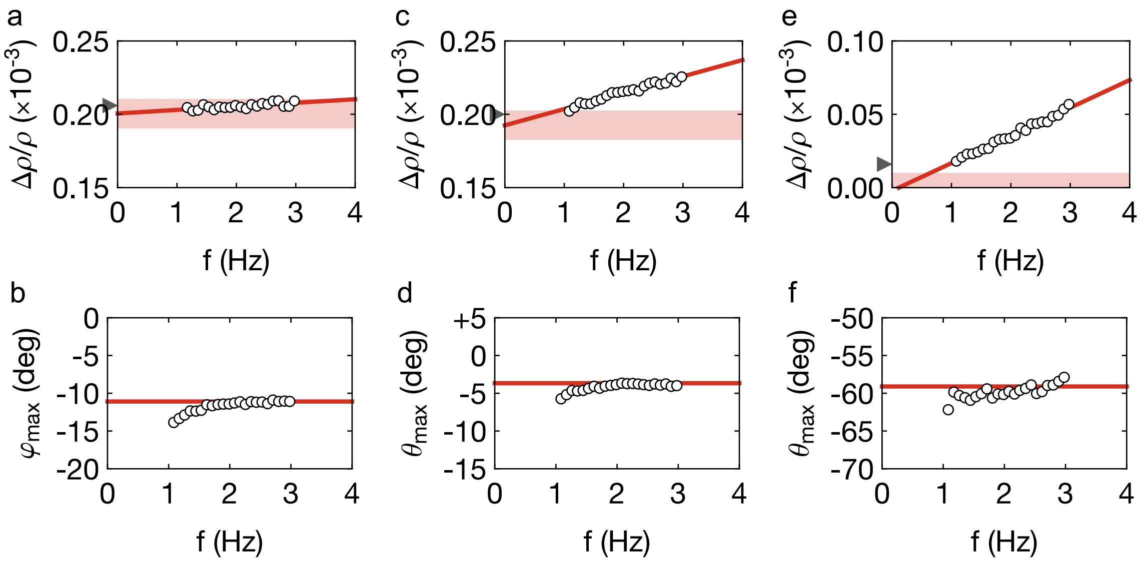

Figure 4.7.: **a** Magnitude of the spin Hall magnetoresistance $\Delta\rho/\rho$ in a 12.8 nm thick Pt film on YIG as determined from field rotations in the sample plane. The solid line is the average value of the data points and the shaded region indicates an error of $\pm 10^{-5}$ in $\Delta\rho/\rho$ for comparison. The gray triangle indicates the $\Delta\rho/\rho$ value as obtained by the conventional method. **b** Corresponding angle φ_{max} that maximizes $\rho(\varphi)$, determined from the phase value by combining data for $+7$ mA and -7 mA applied current. The solid line indicates the average of the values $\varphi_{\text{max}}(f) > 2$ Hz. **c,d** Values analogously determined for a rotation of the magnetic field in the plane perpendicular to the current. **e,f** Values analogously determined for a rotation of the magnetic field in the plane spanned by current direction and film normal.

errors or anisotropy as in the previous sample, or because the linear extrapolation is only an approximation that is, strictly speaking, only valid when the inductive signals are small compared to the voltage signal of interest. The misalignment (Fig. 4.7d) in this particular plane is smaller and θ_{max} is almost zero as expected.
Finally, the data for a field rotation in the plane spanned by current direction and film normal also show the significant electromagnetic induction in this sample holder position (Fig. 4.7e) and pin configuration. The extrapolation to zero frequency, however, yields the expected ratio $\Delta\rho/\rho \approx 0$ predicted by Eq. (4.4). Since the signal here is dominated by the inductive voltages the phase data in Fig. 4.7f give the angle θ_{max} that maximizes induction rather than ρ which explains the unusual value of $\theta_{\text{max}} = -59°$. Despite this issue, however, all $\Delta\rho/\rho$ values agree well with those obtained by the conventional method.

To further investigate the influence of the inductive voltages on both the $\Delta\rho/\rho$ and φ_{max} signal a set of measurements at $f = 2$ Hz as a

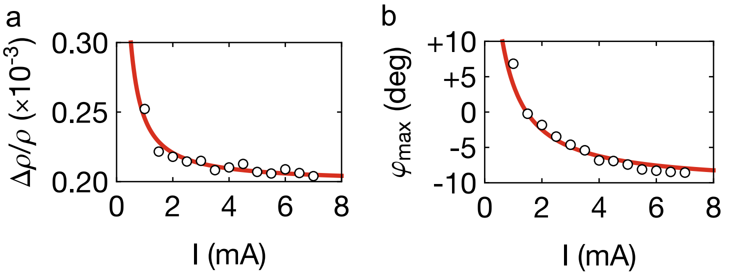

Figure 4.8.: **a** Magnitude of the spin Hall magnetoresistance $\Delta\rho/\rho$ in a 12.8 nm thick Pt film on YIG as a function of the applied current. For small current values the extracted $\Delta\rho/\rho$ is biased by inductive voltages. **b** Corresponding phase data. The solid line is a fit to both data sets simultaneously.

function of the applied current has been performed on the same sample in the configuration with the rotating field in the sample plane. Clearly, both magnitude (Fig. 4.8a) and phase (Fig. 4.8b) strongly depend on the applied current and saturate towards larger current values where V_{ind} eventually becomes negligible compared to $\Delta\rho$ (ΔV). As mentioned above the absolute voltage levels in this sample are only moderately larger than the inductive voltages even at the highest applied current value. To analyze the data also in this nonlinear regime the data have to be modeled using the full expressions for magnitude and phase. They read

$$\frac{\Delta\rho}{\rho} = \frac{\Delta V}{V} = \frac{1}{V}\sqrt{(\Delta V_{\text{x}}^{\text{SMR}} + \Delta V_{\text{x}}^{\text{ind}})^2 + (\Delta V_{\text{y}}^{\text{SMR}} + \Delta V_{\text{y}}^{\text{ind}})^2}, \tag{4.9}$$

$$\varphi^*_{\text{max}} = \arctan\left[\frac{\Delta V_{\text{y}}^{\text{SMR}} + \Delta V_{\text{y}}^{\text{ind}}}{\Delta V_{\text{x}}^{\text{SMR}} + \Delta V_{\text{x}}^{\text{ind}}}\right], \tag{4.10}$$

where $\Delta V_{\text{x(y)}}^{\text{SMR(ind)}}$ refer to the in-phase (x) and out-of-phase (y) components generated by the spin Hall magnetoresistance and electromagnetic induction, respectively. The asterisk in φ^*_{max} signifies the *pure* phase signal as given directly by the lock-in amplifier rather than the one converted to a field angle plotted in Figs. 4.5–4.8. At a given frequency $\Delta V_{\text{x(y)}}^{\text{ind}}$ are constant and $\Delta V_{\text{x(y)}}^{\text{SMR}}$ and V in Eq. (4.9) and Eq. (4.10) can be replaced by some constants times the applied current. Since Eq. (4.9) and Eq. (4.10) share the same fitting parameters, the data in Fig. 4.8 have to be fitted simultaneously, which yields the solid lines in the same figure. Inserting the fitted values for $\Delta V_{\text{x(y)}}^{\text{SMR}}$ into Eq. (4.9) and Eq. (4.10) and setting $\Delta V_{\text{x(y)}}^{\text{ind}} = 0$ gives the electromagnetic induction free $\Delta\rho/\rho = 0.20 \times 10^{-3}$ and $\varphi_{\text{max}} = -10.3°$ in very good agreement with the linear extrapolation performed in Fig. 4.7. The magnitude of the electromagnetic induction is extracted as $V_{\text{ind}} = 11\,\mu\text{V}$, maximized under an angle

$\varphi_{\max} = +46.8°$.

4.4 SUMMARY

Using transient magnetic fields rather than static ones can yield substantial speed-ups for measurements of e.g. the spin Hall magnetoresistance. The results presented in this chapter show that a single data point, which can be acquired within a few seconds, is sufficient to determine the correct magnitude and angular dependence, to within few percent. Using a combination of measurements at different frequencies, or with different effect stimuli, in many cases enables to cleanse the signals from spurious contributions and further increase the precision of the results. While the method is most conveniently employed for quantities that show a purely sinusoidal variation with the direction of the applied magnetic field, more complicated dependencies can also be reconstructed from the higher order harmonics.

As presently implemented the precision limit for the detection of the spin Hall magnetoresistance appears to be a few parts per million. In practice the accuracy of the method is often limited by the accuracy of the mechanical alignment which will often yield an error of a few percent, perhaps larger than the precision level given above. This point, however, is shared with conventional methods and not exclusive to the continuously rotating field approach.

Further improvements to the method can be achieved by a variety of means. Chapter 4.1 introduced how an additional modulation of the desired quantity can be employed to obtain contamination free signals from a single measurement. The challenge in implementing herein lies in the phase-correct acquisition and analysis of the voltage signals which, however, is mostly an instrumentation issue.

For the spin Hall magnetoresistance in particular the dynamic range of the detection circuit (e.g. the lock-in amplifier) is often a limiting factor. The separation of a few microvolt signal amidst a background of about a volt is already pushing the limits of 24-bit analog to digital conversion. A simple solution here is to, if perhaps only partly, compensate the background voltage using e.g. an operational amplifier to allow the detection device to run in a less taxing and therefore more precise regime.

Another crucial factor is the electromagnetic induction. In a perfectly homogeneous magnetic field all but the 1ω signal should not contain any inductive contributions. In practice, especially at field change rates of the order of a Tesla per second as in the experiments above, however, inductive voltages in at least the 2ω signal are hard to avoid entirely. The setup has already been designed with this in mind and measures such as twisted pair wiring were taken to reduce electromagnetic induction. Nevertheless, in practice the magnitude of the electromagnetic induction still appears to vary appreciably with sample position and chip carrier pin configuration in the experiment. Based on initial investigations it seems possible to suppress the present levels of electromagnetic induction by at least an order of magnitude by reorganizing the sample holder wiring to avoid loops which act as pick-up coils. Combined with a reduction of the background voltage as discussed above it appears possible, at least on paper, to reach a sensitivity level of below one part per million.

Presently the setup is limited to measurements under ambient conditions. Given the inner diameter of the Halbach array of 40 mm it appears feasible to design a fitting cryogenic sample holder that could also enable measurements at liquid nitrogen, if not liquid helium, temperatures. If the available space turns out to be an issue, Halbach arrays with the same magnetic field strength but with inner diameters of up to 60 mm are still relatively compact and not excessively expensive. A larger inner diameter would also allow the sample to be mounted on a gimbal head. A gimbal head allows to rotate the sample around two (in some cases three) axes and would make field rotations in arbitrary planes possible and also reorient the rotation plane in-situ, i.e. without remounting the chip carrier. One could thereby also reduce mechanical alignment errors to an absolute minimum.

The most severe limitation of the permanent magnet to overcome is its fixed magnetic field strength. While electromagnets are an obvious substitute that solve this issue, they will generally provide much smaller maximal field strengths. A solution to this challenge is to assemble a circular Halbach array based on two concentric cylinders. With each of them designed to provide the same field strength in their center, their relative orientation can be used to continuously vary the magnetic field strength from zero to twice the maximal field of each individual cylinder. This concept is also employed commercially, but these devices typically do not offer rotation speeds that satisfy the practical requirements of the method. Certainly, such a device is more challenging to integrate into a setup similar to the one employed here, but even if compromises in the maximum field strength or sample volume have to made this seems to be a promising approach.

5

STEADY STATE AND TRANSIENT SPIN SEEBECK EFFECT

Thermoelectricity is the study of the interaction between heat and charge currents. The pioneer in this field is arguably Thomas Seebeck with his discovery that charge and heat transport in conducting solids are intertwined [61]. It took about 60 years until Nernst and Ettingshausen realized that this relation could be further influenced by application of magnetic fields [112]. The magnetization in magnetic materials can play a role quite similar to that of an external magnetic field, eventually giving rise to a family of *spin dependent* thermoelectric effects [113], such as the *spin dependent Seebeck* [114] or the *spin dependent Peltier* [115] effect and are nowadays summarized in a field titled *spin caloritronics* [116]. Maybe the most prominent member of spin caloritronics, however, is the spin Seebeck effect introduced in Ch. 2.5.

Although firmly established experimentally [10, 80, 82, 117–119], the microscopic origin and details of the effect are still only partially understood. Verifying or refuting the large number [12, 62–69] of theoretical assumptions and propositions requires different experimental approaches. This chapter is dedicated to the experimental investigation of the spin Seebeck effect and organized as follows: Ch. 5.1 outlines a numerical technique to investigate the thermodynamic state of the coupled phonon, electron, and magnon systems in typical spin Seebeck experiments. While the calculations presented therein are tailored to the steady state spin Seebeck effect, they could also be applied to other coupled systems and even transient problems. An experimentally focused study of the transient, dynamic evolution of the spin Seebeck effect is discussed in Ch.5.2. Using time varying thermal excitation reveals information about the spectral composition of the magnon spectrum at the YIG/Pt interface. The results yield a consistent understanding of many other reports in the literature and corroborate the notion that mostly low-energy magnons are at the origin of the thermal spin currents measured in experiments. In Ch. 5.3, an experimental technique is presented that allows for simple operation of steady state spin Seebeck experiments with a minimum amount of experimental equipment. The chapter closes with a short summary of the state of affairs.

5.1 COUPLED PHONON, ELECTRON AND MAGNON TEMPERATURES IN NANOSTRUCTURES

In the spin Seebeck effect the application of a thermal gradient across a normal metal/magnet stack induces a spin current flow across the interface between the two. The established theory for the interaction between spin currents in normal metals and magnets was outlined in Ch. 2.3 and is based on a linear response formalism. In linear response a finite difference in the (spin chemical) potentials on both sides of the interface is required to stimulate the spin current flow. Although the spin chemical potential for non-conserved bosonic ensembles such as magnons is zero, a finite spin chemical potential can be utilized to parametrize a non-equilibrium magnon population. Provided the spectral composition of this non-equilibrium magnon population follows a Bose-Einstein-distribution, it can be assigned a magnon temperature which can be used equivalently to the (non-equilibrium) spin chemical potential. In magnetic insulators, only magnons and phonons need to be considered to describe the thermal transport. For metallic magnets also electrons become important. While the dominant source of energy for magnons in magnetic insulators is by influx from (or rather exchange with) the phonon reservoir they may also couple to electrons in an adjacent metal via the spin transfer torque described in Ch. 2.3. If the coupling between magnons and phonons is particularly strong, the two systems will both be thermally distributed at all times. For certain sets of inter and intra subsystem interaction times, however, a thermal gradient may introduce other types of population distributions. Ritzmann *et al.* [68] inferred from micromagnetic simulations that it is possible that high-frequency magnons thermalize with the lattice much faster than their lower energetic counterparts. Thus, when magnons move along a thermal gradient with the aim of establishing thermal equilibrium, the magnon population at the ends of the gradient will have an inflated low-frequency magnon population, i.e. the local magnon distribution deviates from a Bose-Einstein profile. This conclusion is boosted by experimental findings by Kehlberger *et al.* [75], Kikkawa *et al.* [120], Boona and Heremans [72], Jin *et al.* [121] and those presented in Ch. 5.2 that are all compatible with a spin Seebeck spin current dominated by the low-frequency end of the magnon spectrum. Thus, the question of whether or not the magnon population is Bose-Einstein like in typical experiments is still debated in literature and will be discussed further in Ch. 5.2.

A deviation from a Bose-Einstein profile as suggested in some of the literature appears to prevent a treatment of the magnon population on basis of a thermal ensemble. However, there is sufficient evidence to assume the deviation of the magnon spectrum to be small enough as to still warrant the term *magnon temperature* and a treatment on the basis of the heat diffusion equation. On the numeric side, the excess low-frequency magnon population calculated by Ritzmann *et al.* amounts to a few percent at best, signifying that also at the ends of the thermal gradient the magnon spectrum is still largely thermal. While it is crucial to distinguish between elastic an inelastic scattering processes this result is perhaps expected as also magnon-magnon interaction times, while numerical values are still largely speculative, are likely to be much shorter than other interaction mechanisms [22]. This conclusion is supported by Brillouin light scattering spectroscopy experiments by Agrawal *et al.* [122] who investigated the magnon temperature and found no evidence for the magnon temperature to deviate from the underlying, spatially varying phonon temperature. If the excess low-frequency magnon population was substantial one would have expected to observe notable temperature differences as will be discussed in the following.

The spin Seebeck theory developed by Xiao *et al.* [12] derives the spin current emitted into or from the normal metal under the assumption that the magnon spectrum is described by a Bose-Einstein distribution, and thus characterizable by a magnon temperature T_m, at all times. The paragraph above argues that this remains viable even in light of newer findings of an increased spectral weight of the low-frequency magnons. However, it appears possible that the measured spin current originates dominantly from these low-frequency magnons which is likely to require some corrections to the relation between measured voltage and the magnon temperature viz. magnon accumulation in the theory by Xiao *et al.*.

Despite potential issues with the derived spin Seebeck voltage, Xiao *et al.*'s approach enables to study in detail the intricate thermodynamic relation between phonons, electrons and magnons which will, in any case, exhibit the mutual relaxation described in the model. The thermal coupling between electrons and magnons by spin pumping, i.e. the spin transfer torque, in particular is of general interest for thermal transport in magnetic nanostructures. From a microscopic perspective, the theory also allows to infer the thermodynamic state at the normal/magnet interface, whereas in experimental publications the average *temperature gradient* across the entire sample is usually quoted. In the theory by Xiao *et al.* the thermodynamic state, parametrized by the *temperature difference* ΔT_me between the magnon and the electron systems at the normal metal/magnet interface, measures the degree of non equilibrium i.e. the spin (magnon) chemical potential difference that drives the spin Seebeck effect as discussed above. The temperature difference ΔT_me arises due to different thermal properties and boundary conditions for the magnons, phonons and electrons in the normal metal/magnet hybrids used in experiments. The phonon (T_p), electron (T_e) and magnon (T_m) temperature

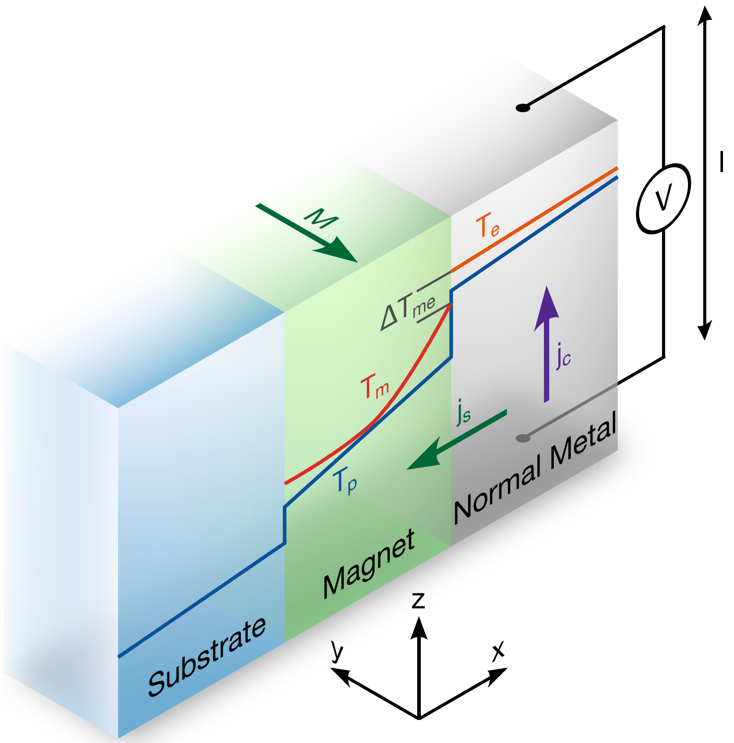

Figure 5.1.: The temperatures of phonons T_p, electron T_e and magnons T_m determine the magnitude of the spin current between the magnet and the normal metal and thereby the voltage measured in experiment (*cf.* Ch. 2.2). Due to the different materials, boundary conditions and couplings the temperature profiles can develop complex spatial profiles.

profiles in a normal metal/magnet/substrate multilayer structure are schematically depicted in Fig. 5.1. As detailed in the following, the temperature profiles can show discontinuities at the material interfaces due to interface properties such as the Kapitza resistance [123].

In this chapter, the phonon, electron and magnon temperature profiles in magnet/normal metal hybrid structures are modeled and calculated, by solving the heat transport equations with appropriate boundary conditions. In particular, the heat current carried by the pumped spin current through the interface is taken into account. The discussion here is limited to hybrids based on the ferrimagnetic insulator yttrium iron garnet, however, the approach can easily be extended to other material systems. The calculations are done analytically whenever possible, and are supplemented by three-dimensional finite element (3D FEM) analysis (COMSOL). The magnon temperature calculations are based on the work by Sanders

COMSOL Multiphysics 4.3a

and Walton [124] and Xiao *et al.* [12], with a focus on ultrathin films in which interfacial effects become important for the thermal transport. The temperature profiles thus obtained compare well with the experimental results by Agrawal *et al.* [122] who find no significant difference between magnon and phonon temperatures under a lateral thermal gradient. The T_p, T_e, and T_m profiles in Pt/YIG/substrate structures as used in most spin Seebeck experiments and the issues with the inferred spin Seebeck voltage are also discussed. The chapter expands on the results published in Phys. Rev. B 88, 094410 (2013) (Ref. [15]) and extensively reuses text and figures.

5.1.1 *Xiao* et al.*'s theory of the spin Seebeck effect*

In contrast to spin pumping (*cf.* Ch. 2.4), where magnons of a common frequency are considered, thermally excited magnons are distributed over all possible frequencies. By summing over all magnon states, weighted by the Bose-Einstein distribution, Xiao *et al.* [12] obtain the magnetic coherence volume

$$V_\mathrm{a} = \frac{2}{3\zeta(5/2)} \left(\frac{4\pi D}{k_\mathrm{B} T_\mathrm{m}} \right)^{3/2}, \tag{5.1}$$

where ζ is the Riemann Zeta function, D is the spin wave stiffness, k_B is the Boltzmann constant and T_m is the temperature of the magnetic system. At room temperature the magnetic coherence volume in YIG ($D \approx 5 \times 10^{40}\,\mathrm{Jm}^2$ [125, 126]) is about $V_\mathrm{a} \approx (1.3\,\mathrm{nm})^3$. V_a relates the magnon accumulation to the emitted spin current as

$$j_\mathrm{s,SSE} = \frac{g_\mathrm{r} \gamma \hbar k_\mathrm{B}}{2\pi M_\mathrm{s} V_\mathrm{a}} \Delta T_\mathrm{me}, \tag{5.2}$$

where $g_\mathrm{r} = \mathrm{Re}\left(g^{\uparrow\downarrow}\right)$ is the real part of the spin mixing interface conductance per unit area [127], $\gamma = g\frac{e}{2m}$ is the gyromagnetic ratio with g as the Landé g-factor and the electron mass m, k_B is the Boltzmann constant, $\hbar$ is the Planck constant, M_s is the saturation magnetization of the magnet and finally $\Delta T_\mathrm{me} = T_\mathrm{m} - T_\mathrm{e}$ is the temperature difference between the magnons in the magnet and the electrons in the normal metal at the magnet/normal metal interface. As evident from Eq. (5.2), the spin Seebeck effect crucially depends ΔT_me. T_e and T_m individually, however, are strongly coupled to the phonon temperature T_p. In the following, the coupling between the three systems is discussed in more detail and the equations governing the interaction are derived.

5.1.2 *Heat transport in solids*

On macroscopic scales, heat transport in a homogeneous material with a single heat carrier (e.g. phonons) is described by the heat diffusion equation [128]

$$\nabla^2 T - \frac{1}{\mathsf{k}}\frac{\partial T}{\partial t} = -\frac{Q}{\kappa}, \tag{5.3}$$

where Q is the heating power density, κ is the thermal conductivity, and $\mathsf{k} = \kappa/\varrho C$ is the thermal diffusivity, with ϱ as the mass density and C as the heat capacity of the material. For simplicity, κ, ϱ, and C are assumed to be spatially homogeneous and temperature independent. This assumption is valid as long as the considered temperature changes are small. In a heterostructure consisting of several layers stacked on top of one another, Eq. (5.3) has to be solved piecewise for each layer [129]:

$$\nabla^2 T_i - \frac{1}{\mathsf{k}_i}\frac{\partial T_i}{\partial t} = -\frac{Q_i}{\kappa_i}, \tag{5.4}$$

with boundary conditions for the temperatures T_i and T_{i+1} on both sides of an interface

$$\begin{aligned} -\kappa_i \frac{\partial T_i}{\partial x}\bigg|_{\text{interface}} &= \frac{1}{R_{\text{th},i}}[T_i - T_{i+1}]\bigg|_{\text{interface}}, \\ -\kappa_{i+1} \frac{\partial T_{i+1}}{\partial x}\bigg|_{\text{interface}} &= \frac{1}{R_{\text{th},i}}[T_i - T_{i+1}]\bigg|_{\text{interface}}, \end{aligned} \tag{5.5}$$

where i is the index for the individual materials (or layers, i.e. the normal metal, the magnet or the substrate), and $R_{\text{th},i}$ is the interfacial thermal resistance between layer i and $i+1$. In the steady state Eq. (5.4) reduces to

$$\nabla^2 T_i = -\frac{Q_i}{\kappa_i}. \tag{5.6}$$

Solving Eq. (5.6) together with the appropriate boundary conditions [Eq. (5.5)] leads to the temperature distribution.

There can be additional heat conduction channels such as via plasmons [130] which are not considered here.

It often suffices to consider phonons as the exclusive heat transportation channel in solids. In general, however, heat is not only carried by phonons, but by electrons and magnons as well. To draw a complete picture of the arising temperature profiles one therefore has to take the coupling between the individual systems into account. While both thermal magnons and electrons have relatively short interaction times with phonons [131–133], in few nanometer thick films, equilibration between the individual systems might be incomplete. The simulations in the following therefore treat phonons, electrons and magnons separately.

5.1.3 *Coupled magnonic and phononic heat transport*

The thermal interaction between two subsystems was first formalized by Kaganov *et al.* [134] for the coupled phonon-electron system.

Sanders and Walton [124] transferred the approach to magnetic excitations which serves as the basis for the generalization below.
Let ΔT_{mp} denote the difference between the magnon temperature T_{m} and the phonon temperature T_{p}, then the magnon-phonon relaxation time τ_{mp} is defined as

$$\frac{d}{dt}\Delta T_{\mathrm{mp}} = -\frac{\Delta T_{\mathrm{mp}}}{\tau_{\mathrm{mp}}}, \tag{5.7}$$

and the time evolution of T_{m} and T_{p} follows

$$\begin{aligned} \frac{dT_{\mathrm{p}}}{dt} &= \frac{c_{\mathrm{m}}}{c_{\mathrm{t}}}\frac{T_{\mathrm{m}} - T_{\mathrm{p}}}{\tau_{\mathrm{mp}}}, \\ \frac{dT_{\mathrm{m}}}{dt} &= \frac{c_{\mathrm{p}}}{c_{\mathrm{t}}}\frac{T_{\mathrm{p}} - T_{\mathrm{m}}}{\tau_{\mathrm{mp}}}, \end{aligned} \tag{5.8}$$

where c_{m}, c_{p} and $c_{\mathrm{t}} = c_{\mathrm{p}} + c_{\mathrm{m}}$ denote the magnon, phonon and total (sum of the two) heat capacity per unit volume. The heat flux Q_{mp} between the phonon and the magnon system is then given by

$$\begin{aligned} Q_{\mathrm{mp}}(x) &= c_{\mathrm{m}}\frac{dT_{\mathrm{m}}(x)}{dt} \\ &= \frac{c_{\mathrm{p}}c_{\mathrm{m}}}{c_{\mathrm{t}}}\frac{T_{\mathrm{p}}(x) - T_{\mathrm{m}}(x)}{\tau_{\mathrm{mp}}}, \end{aligned} \tag{5.9}$$

where x is the position along the thermal gradient (*cf.* Fig. 5.1 and Fig. 5.2). According to Eq. (5.6), the magnon temperature obeys

$$\frac{d^2T_{\mathrm{m}}(x)}{dx^2} + \frac{c_{\mathrm{p}}c_{\mathrm{m}}}{c_{\mathrm{t}}}\frac{1}{\kappa_{\mathrm{m}}\tau_{\mathrm{mp}}}\left[T_{\mathrm{p}}(x) - T_{\mathrm{m}}(x)\right] = 0, \tag{5.10}$$

where κ_{m} is the magnon thermal conductivity. The phonon temperature is given by

$$\frac{d^2T_{\mathrm{p}}(x)}{dx^2} + \frac{c_{\mathrm{p}}c_{\mathrm{m}}}{c_{\mathrm{t}}}\frac{1}{\kappa_{\mathrm{p}}\tau_{\mathrm{mp}}}\left[T_{\mathrm{m}}(x) - T_{\mathrm{p}}(x)\right] = 0. \tag{5.11}$$

The equations are now applied to an insulating magnet (YIG) of length d enclosed to the left L ($x = 0$) and right R ($x = d$) by two nonmagnetic materials (i.e., the substrate on the left and the normal metal on the right as shown in Fig. 5.2). To concentrate on the magnetic insulator the phonon temperatures $T_{\mathrm{L}}^{\mathrm{p}} = \text{const.}$ for $x = 0$ and $T_{\mathrm{R}}^{\mathrm{p}} = \text{const.}$ for $x = d$ in the following. Further, when the material on the left or right side of the insulating magnet is conducting, $T_{\mathrm{L/R}} = T_{\mathrm{L/R}}^{\mathrm{p}} = T_{\mathrm{L/R}}^{\mathrm{e}}$ for the sake of simplicity at this point. As noted at the end of Ch. 5.1.2 this constraint will not be utilized for the 3D FEM simulations in Ch. 5.1.6. According to Eq. (5.5) the boundary conditions for the phonon temperature are

$$\begin{aligned} -\kappa_{\mathrm{p}}\left.\frac{dT_{\mathrm{p}}(x)}{dx}\right|_{x=0} &= \frac{1}{R_{\mathrm{th,L}}^{\mathrm{p}}}\left[T_{\mathrm{L}} - T_{\mathrm{p}}(0)\right], \\ -\kappa_{\mathrm{p}}\left.\frac{dT_{\mathrm{p}}(x)}{dx}\right|_{x=d} &= \frac{1}{R_{\mathrm{th,R}}^{\mathrm{p}}}\left[T_{\mathrm{p}}(d) - T_{\mathrm{R}}\right], \end{aligned} \tag{5.12}$$

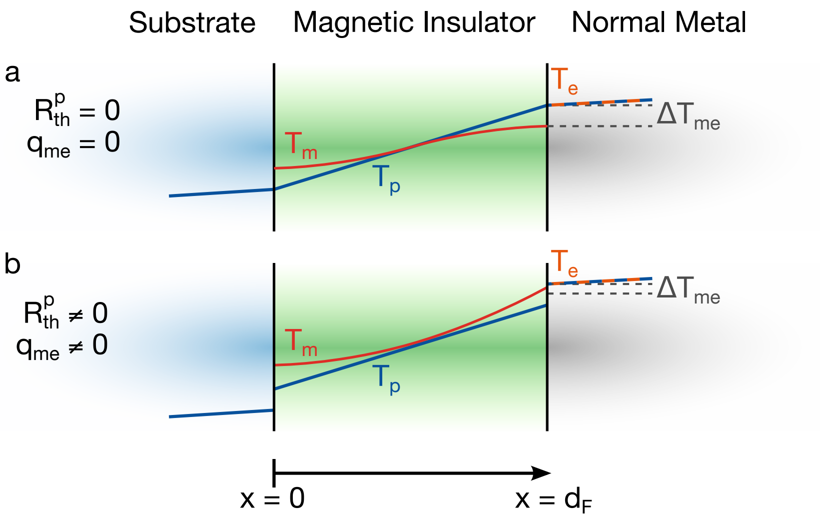

Figure 5.2.: Schematic phonon and magnon temperature profiles in a layered structure. Phonon and electron temperatures are assumed identical in the normal metal. **a** For vanishing interfacial thermal resistance $R^{\mathrm{p}}_{\mathrm{th}} = 0$ and no spin mediated heat current across the magnet/normal metal interface [12], the temperature difference $\Delta T_{\mathrm{me}} = T_{\mathrm{m}} - T_{\mathrm{e}} = T_{\mathrm{m}} - T_{\mathrm{p}}$ depends solely on the magnon-phonon interaction. **b** Taking into account finite interfacial thermal resistances for both spins and phonons results in a qualitatively different temperature profile.

with the appropriate interfacial thermal conductances $(R^{\mathrm{p}}_{\mathrm{th,L}})^{-1}$ and $(R^{\mathrm{p}}_{\mathrm{th,R}})^{-1}$ for the left and right interface (*cf.* Ch. 5.1.4). Magnons cannot exist in nonmagnetic materials. In spin pumping and spin Seebeck experiments, however, the spin current, i.e., the transfer of angular momentum (*cf.* Ch.2.3) across the magnet/normal metal interface, is accompanied by an energy transfer [135] and thus an interface magnetic heat current $q_{\mathrm{me}} = \left(R^{\mathrm{m}}_{\mathrm{th}}\right)^{-1} \Delta T_{\mathrm{me}}$ proportional to the interface magnetic heat conductance: [12, 64]

$$(R^{\mathrm{m}}_{\mathrm{th}})^{-1} = \frac{k_{\mathrm{B}} T}{\hbar} \frac{\mu_{\mathrm{B}} k_{\mathrm{B}} g_{\mathrm{r}} \eta}{\pi M_{\mathrm{s}} V_{\mathrm{a}}}, \tag{5.13}$$

where μ_{B} is the Bohr magneton and η is the spin backflow correction factor [*cf.* Eq. (5.35)]. In the macrospin approximation originally employed by Xiao *et al.* the characteristic energy in Eq. (5.13) is given by the ferromagnetic resonance (FMR) frequency of the spin system [12]. However, in a system of thermal magnons this should be the temperature of the magnons [64]. The boundary conditions for the magnon

$E = \hbar\omega_{\mathrm{FMR}}$

$E = k_{\mathrm{B}} T_{\mathrm{m}} = k_{\mathrm{B}} T_{\mathrm{p}}$

system are:

$$\begin{aligned} -\kappa_{\mathrm{m}} \left. \frac{dT_{\mathrm{m}}(x)}{dx} \right|_{x=0} &= \frac{1}{R^{\mathrm{m}}_{\mathrm{th,L}}} \left[T_{\mathrm{L}} - T_{\mathrm{m}}(0) \right], \\ -\kappa_{\mathrm{m}} \left. \frac{dT_{\mathrm{m}}(x)}{dx} \right|_{x=d} &= \frac{1}{R^{\mathrm{m}}_{\mathrm{th,R}}} \left[T_{\mathrm{m}}(d) - T_{\mathrm{R}} \right]. \end{aligned} \tag{5.14}$$

With these boundary conditions, $T_{\mathrm{m}}(x)$ and $T_{\mathrm{p}}(x)$ can be calculated from Eqs. (5.10) and (5.11). The same set of equations was solved by Xiao *et al.*, however, with identical interfaces L and R. The present approach enables the description of a large number of experiments with very different boundary conditions for the substrate/magnet and magnet/normal metal interface.

Fig. 5.2 sketches $T_{\mathrm{m}}(x)$ and $T_{\mathrm{p}}(x)$ profiles as obtained from Eqs. (5.10) and (5.11) in different limits. When the phonon interfacial thermal resistance and interface magnetic heat current are disregarded, the original result of Ref. [124] is recovered, in which ΔT_{me} is exclusively governed by the magnon-phonon interaction [Fig. 5.2a]. Taking into account the phonon interfacial thermal resistance and the interface magnetic heat conductance, qualitatively different temperature profiles emerge [Fig. 5.2b]. To calculate the temperature profiles for the coupled phonon-electron systems in the metallic layer Eqs. (5.10)–(5.12) and (5.14) can simply be modified by substituting the magnon parameters (T_{m}, c_{m}, κ_{m}, τ_{mp}, $R^{\mathrm{m}}_{\mathrm{th,L/R}}$) with the appropriate electron ones (T_{e}, c_{e}, κ_{e}, τ_{ep}, $R^{\mathrm{e}}_{\mathrm{th,L/R}}$). It is also conceptually simple to derive the temperature distributions in conducting magnets by considering also the electron temperature analogously to Eqs. (5.7)–(5.9) in the model.

5.1.4 *Thermal boundary resistance*

Equation (5.13) introduced an explicit expression for the heat exchange mediated by the emission of a spin current. However, even when considering only a single type of heat carrier there will be a finite thermal (interfacial) resistance whenever there is a sudden change in the heat transport parameters. For phonons the interfacial thermal resistance is also referred to as thermal contact or Kapitza resistance [123]. The heat flow q across an interface can be expressed in linear response ("Ohm's law") by:

$$q = \frac{1}{R_{\mathrm{th}}} \Delta T. \tag{5.15}$$

If the transmission probability of the heat carriers across the interface is Γ, the associated heat flow q, i.e. the amount of energy U transported across the interface per unit area A and unit time δt can be written as

$$q = \frac{U}{A\delta t}\Gamma \approx \frac{\frac{\partial U}{\partial T}\Delta T}{A\delta t}\Gamma. \tag{5.16}$$

Combining Eqs. (5.15) and (5.16) yields

$$\begin{aligned}(R_{\text{th}})^{-1} &= \frac{\partial U}{\partial T}\frac{1}{A\delta t}\Gamma \\ &= C\frac{l}{V}\frac{1}{\delta t}\Gamma \\ &= \frac{C}{V}v_{\text{g}}\Gamma, \end{aligned} \tag{5.17}$$

where $C = \frac{\partial U}{\partial T}$ is the heat capacity and $v_{\text{g}} = \frac{l}{\delta t}$ is the group velocity of the heat carriers.

The heat capacity per unit volume $c = C/V$ should be calculated for each acoustic branch j:

$$c_j = \frac{C_j}{V} = \frac{d}{dT}\int_0^\infty \hbar\omega D_j(\omega)n(\omega,T)d\omega, \tag{5.18}$$

where $D_j(\omega)$ is the phonon density of states and $n(\omega,T)$ is the Bose-Einstein distribution function. For the transmission probability Γ two models are generally used. The *acoustic mismatch model* [136] (AMM) assumes that the phonons are scattered according to Snell's law at the interface while the *diffusive mismatch model* [137] assumes diffuse scattering. The following adopts the acoustic mismatch model since epitaxially grown interfaces can be considered flat on a length scale corresponding to the wavelength of the relevant acoustic phonons. At any rate, the interfacial thermal resistance obtained from the acoustic and diffusive mismatch models agree with each other within one order of magnitude for all interfaces examined in this chapter such that choosing one over the other should not significantly alter the results presented here.

The interfacial thermal resistance in the acoustic mismatch model reads: [138]

$$\begin{aligned}\left(R^{\text{p}}_{\text{th}}\right)^{-1} &= \frac{1}{2}\sum_j v_{1,j}\Gamma_{1,j} \\ &\quad\times\int_0^\infty \hbar\omega\frac{d\left[D_{1,j}(\omega)n(\omega,T)\right]}{dT}d\omega, \end{aligned} \tag{5.19}$$

$$\Gamma_{1,j} = \int_0^{\pi/2}\alpha^{\text{AMM}}_{1\to 2}(\theta,j)\cos\theta\sin\theta d\theta, \tag{5.20}$$

$$\alpha^{\text{AMM}}_{1\to 2}(\theta_1,j) = \frac{\frac{4\varrho_2 v_{2,j}}{\varrho_1 v_{1,j}}\cdot\frac{\cos\theta_{2,j}}{\cos\theta_{1,j}}}{\left(\frac{\varrho_2 v_{2,j}}{\varrho_1 v_{1,j}}+\frac{\cos\theta_{2,j}}{\cos\theta_{1,j}}\right)^2}, \tag{5.21}$$

where $\theta_{2,j}$ is linked to $\theta_{1,j}$ (the angle of the outgoing and incident phonons) by Snell's law of acoustic waves [139]

$$v_{2,j}\sin\theta_{1,j} = v_{1,j}\sin\theta_{2,j}, \tag{5.22}$$

where $v_{i,j}$ is the speed of sound, and $j \in \{1,2,3\}$ denotes the pressure ($j = 1$) and shear wave ($j = 2,3$) phonon branches. The index $i \in$

$\{1,2\}$ denotes the materials on the left and right side of an interface. The full expression for $\alpha^{\mathrm{AMM}}_{1\to 2}(\theta_1, j)$ in Eq. (5.21) was adopted from Ref. [136]. At $T = 300\,\mathrm{K}$ and using the Debye approximation [140] the Debye frequencies $\omega_{\mathrm{c},i,j}$ are obtained from the longitudinal and transverse speeds of sound $v_{i,j}$ by [141]

$$\omega_{\mathrm{c},i,j} = (6\pi n_i)^{\frac{1}{3}}\, v_{i,j}, \tag{5.23}$$

where n is the atomic density of the material. The Debye model is a good approximation for simple crystal structures and should be appropriate for the long wavelength phonons, but is too crude to accurately describe the often complex phonon dispersion at large wave vectors.

Using Eq. (5.19) in the Debye approximation and the material parameters summarized in Table 5.1, the thermal contact resistances for the relevant interfaces are: $(R^{\mathrm{p,Pt/YIG}}_{\mathrm{th}})^{-1} = 2.79 \times 10^{8}\,\mathrm{W/(m^2\,K)}$ for the YIG/Pt interface, $(R^{\mathrm{p,YIG/GGG}}_{\mathrm{th}})^{-1} = 2.04 \times 10^{8}\,\mathrm{W/(m^2\,K)}$ for the YIG/GGG interface and $(R^{\mathrm{p,YIG/YAG}}_{\mathrm{th}})^{-1} = 1.27 \times 10^{8}\,\mathrm{W/(m^2\,K)}$ for the YIG/YAG interface, respectively. These results agree well with experimental data obtained for similar interfaces [142, 143], but should only be considered an approximation to the actual values for factors unaccountable for in the analytical treatment above.

5.1.5 *One dimensional temperature profiles*

In order to quantitatively calculate $T_{\mathrm{p}}(x)$ and $T_{\mathrm{m}}(x)$ in YIG thin films from Eqs. (5.10)–(5.14) the magnon parameters c_{m}, κ_{m}, and τ_{mp} are required. In YIG, unfortunately, they are only well established for temperatures $T \lesssim 10\,\mathrm{K}$.

The available low temperature data [72, 144–146] for the YIG magnon thermal conductivity show that the magnonic contribution to the total thermal conductivity [124] is of the order of a few percent at low temperatures. However, with the notable exception of spin ladder and spin chain systems [147, 148], it is generally assumed that the magnonic contribution to the total thermal conductivity at room temperature [12, 149] is very small. Theory [150, 151] indeed predicts κ_{m} to decay inversely proportional to T or even exponentially at elevated temperatures due to increasing scattering processes [152]. Additional support for very small κ_{m} in YIG comes from an analysis [153] of the total thermal conductivity that does not show any significant features around the Curie temperature where the relative change in the magnon thermal conductivity should be large. Due to the aforementioned reasons and for lack of better data κ_{m} is here assumed to be of the order of $10^{-2} - 10^{-3}\,\mathrm{W/(mK)}$, which is also supported by earlier theoretical estimates for κ_{m} at elevated temperatures [149], and the mean of the assumed range of $\kappa_{\mathrm{m}} = 3 \times 10^{-3}\,\mathrm{W/(mK)}$ is taken for the calculations. The expression for κ_{m} originally adopted by Xiao

et al. is limited to the low temperature regime and yields values at room temperature of $\kappa_\mathrm{m} > 1 \times 10^4\,\mathrm{W/(m\,K)}$ which appear odd based on the available data.
The magnon heat capacity is calculated [12, 154] from the spin wave stiffness $D = 8.5 \times 10^{-40}\,\mathrm{J\,m^2}$ (Ref. [22, 155]) as

$$c_\mathrm{m} = \frac{15\zeta(5/2)}{32}\sqrt{\frac{k_\mathrm{B}^5 T^3}{\pi^3 D^3}}, \tag{5.24}$$

which yields a value of $c_\mathrm{m} \approx 16\,750\,\mathrm{J/(m^3K)}$ at $T = 300\,\mathrm{K}$.
The magnon-phonon relaxation time τ_mp critically depends on the specific magnon mode. While it is relatively large for microwave magnons [156, 157] it decreases significantly for short wavelength magnons [131] with an energy comparable to $k_\mathrm{B}T_{(\mathrm{p})}$. Assuming that the majority of the magnetic damping in the YIG is due to the interaction with phonons, one can estimate τ_mp from a comparison with Eq. (2.9) by

$$\tau_\mathrm{mp} = (\alpha\omega)^{-1} \approx \frac{\hbar}{\alpha k_\mathrm{B} T}, \tag{5.25}$$

where α is the Gilbert damping parameter of the bare YIG film. As in Eq. (5.13), the expression for τ_mp differs for the macrospin-approximation employed in Ref. [12] and for a broad magnon ensemble, however, the above should be more appropriate in the case of thermal magnons in an extended magnet. While there is a large spread in of reported values for $\alpha \approx 10^{-3} - 10^{-5}$ (Ref. [59, 64, 99, 158–160]) higher values are generally found in thin films where two and three magnon scattering processes contribute to the damping. Adopting $\alpha = 10^{-4}$ in the following one obtains a magnon-phonon relaxation time for thermal magnons of $\tau_\mathrm{mp} = 255\,\mathrm{ps}$. This value is also supported by the results presented in Ch. 5.2.
The temperature profile obtained for a thermal magnon system is displayed in Fig. 5.3 for a 50 nm thick YIG film with $T_\mathrm{L} = 300\,\mathrm{K}$ and $T_\mathrm{R} = 301\,\mathrm{K}$ using the material parameters listed in Tab. 5.1 and taking $\left(R_\mathrm{th}^\mathrm{m}\right)^{-1}$ and τ_mp as estimated above. Due to the strong interaction between magnons and phonons ($\propto \tau_\mathrm{mp}^{-1}$) the magnon temperature approaches the phonon temperature even over very short length scales and the interface magnetic heat current notably affects the magnon temperature profile. In the formalism by Xiao *et al.*,[12] the magnetic coherence length $\sqrt[3]{V_\mathrm{a}} \approx 1.3\,\mathrm{nm}$ gives the length over which a given perturbation is felt, or in other words, the effective width of the interface and hence the length over which magnons can directly couple to the electron spins in the normal metal. This results in a ΔT_me of about 27 mK. The effect of the interface magnetic heat current q_me on ΔT_me scales inversely proportional with the thickness of the magnetic layer up to a critical thickness. For the chosen parameter set, however, this scaling is limited to few nm up to which any additional heat has fully relaxed with the magnon reservoir.

	ϱ [kg/(m^3)]	c_p^* [J/(kgK)]	c_e^* [J/(kgK)]	κ_p [W/(Km)]
Pt	21450 [a]	120 [a,e]	10 [e]	8 [a,f]
YIG	5170 [b]	570 [c]	-	6 [g]
GGG	7080 [c]	400 [c]	-	8 [h]
YAG	4550 [d]	625 [c]	-	9 [g]

	κ_e [W/(Km)]	v_long [m/s]	v_trans [m/s]
Pt	64 [a,f]	3300 [a]	1700 [a]
YIG	-	7170 [b]	3843 [b]
GGG	-	6545 [i]	3531 [i]
YAG	-	8600 [j]	4960 [j]

[a] Ref. [102] [b] Ref. [161] [c] Ref. [162] [d] Ref. [163] [e] Ref. [133] [f] Ref. [164]
[g] Ref. [153] [h] Ref. [165] [i] Ref. [166] [j] Ref. [167]

Table 5.1.: Mass density ϱ, phonon specific heat capacity c_p^*, electron specific heat capacity c_e^* (both at constant pressure), phonon thermal conductivity κ_p, electron thermal conductivity κ_e, longitudinal speed of sound v_long and transverse speed of sound v_trans used for the calculation of the phonon temperature distribution in YIG/Pt-type hybrids. Electronic contributions to the values for the phonon heat capacity and the phonon thermal conductivity in platinum have been separated using the quoted sources. Additionally $c_\mathrm{p}^* \gg c_\mathrm{m}^*$ and $\kappa_\mathrm{p} \gg \kappa_\mathrm{m}$ (Ref. [12]) so that heat capacity and thermal conductivity in the YIG can be considered essentially free from magnonic contributions.

The magnetic coherence length $\sqrt[3]{V_\mathrm{a}}$ is closely related with the thermal de Broglie length of the magnon system. In contrast to the bulk magnon model considered by Xiao *et al.* [12], Hoffman *et al.* [64] presented an approach based on a minimal Landau-Lifshitz-Gilbert treatment of films with arbitrary thickness. This approach proceeds from the assumption that the magnon-phonon relaxation is described by the Gilbert damping, but does not take into account the Kapitza resistance. For sufficiently thick magnetic layers Hoffman *et al.* find a spin current j_s across the magnet/normal metal interface of

$$j_\mathrm{s} = \frac{\hbar g_\mathrm{r} \gamma}{4\pi M_\mathrm{s}} \frac{\left(\frac{k_\mathrm{B} T}{D} - \frac{\gamma \hbar \mu_0 H_\mathrm{ext}}{D}\right)^{3/2}}{3\pi^2 \left(1 + \frac{2\hbar g_\mathrm{r} \gamma}{4\pi M_\mathrm{s} \alpha d_\mathrm{F}}\right)} k_\mathrm{B} \Delta T \tag{5.26}$$

where ΔT is the (phonon) temperature drop across the magnetic layer of thickness d_F and $\mu_0 H_\mathrm{ext}$ with the vacuum permeability $\mu_0 = 4\pi \times 10^{-7}\,\mathrm{Vs/(Am)}$ is the externally applied magnetic field. Using identical parameters, the theory by Hoffman *et al.* agrees with that of Xiao *et al.* within an order of magnitude. For the case discussed above, the theory by Hoffman *et al.* yields smaller values,

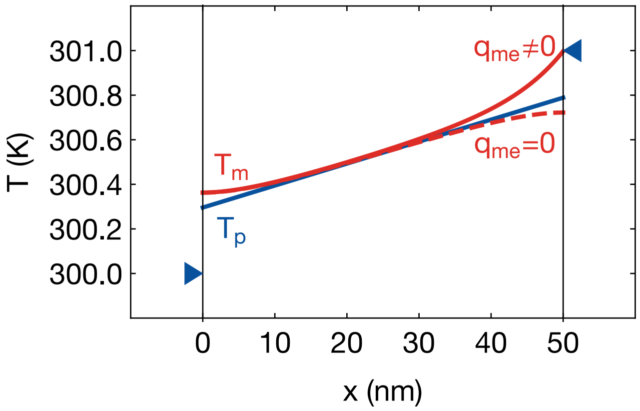

Figure 5.3.: Magnon and phonon temperature profiles for thermal magnons calculated from Eq. (5.10) and Eq. (5.11) for a 50 nm thick YIG film with $T_\mathrm{L} = 300\,\mathrm{K}$ and $T_\mathrm{R} = 301\,\mathrm{K}$, the material parameters from Tab. 5.1 and appropriate $(R_\mathrm{th})^{-1}$ for both phonons and magnons. The interface magnetic heat current q_me is limited to the right interface here. The dashed line depicts the case when the interface magnetic heat current q_me is not taken into account.

however, the calculations show that assuming equality between phonon and magnon temperatures at the magnet/normal metal interface is only an approximation.

In summary of this section, the interface magnetic heat conductance can have a substantial impact on T_m in thin films. A comparison of the theories by Hoffman *et al.* [64] and Xiao *et al.* [12] shows reasonable agreement and underlines the importance of the magnon-phonon interaction. The numerical values calculated in this section are certainly prone to some significant uncertainty as many crucial material parameters (c_m, κ_m and τ_mp) remain unknown at room temperature and had to be inferred from theoretical calculations. The fact that the magnon temperature profile varies notably over the magnetic coherence length could further indicate the limits of the diffusive Sanders and Walton [124] approach. Reszende *et al.* [168] improved on the theoretical derivation of c_m and κ_m and suggest that c_m is slightly smaller and κ_m larger than the values employed here. Although their absolute value for κ_m appears to be too large to be compatible with the heuristic arguments brought forward above, smaller c_m and larger κ_m, in general, reduce the coupling between magnons and phonons and thereby further diminish ΔT_me. On the other hand the employed damping value of 10^{-4} is rather generous for thin films grown at the Walther-Meißner-Institut as discussed in Ch. 3 and Ch. 7.2. Since the effect of the adjusted κ_m and c_m and the larger damping compensate each other to some degree, no substantially different results are expected when accounting for these newer findings.

5.1.6 *Comparison with experiments*

For a first check of consistency the set of equations in Ch. 5.1.3 are used to address the temperature profiles in a transverse measurement geometry, i.e. in which the externally applied thermal gradient lies within the YIG film plane.
To investigate claims by Uchida *et al.* [73] that this particular geometry also allows for a spin Seebeck effect, Agrawal *et al.* [122] performed Brillouin light scattering (BLS) experiments on a $3\,\mathrm{mm} \times 10\,\mathrm{mm} \times 6.7\,\mu\mathrm{m}$ YIG film (without normal metal stripes on top). Probing the magnon density along the direction of an applied thermal gradient via BLS enabled them to infer the magnon temperature and validate if sufficiently large temperature differences to observe a transverse spin Seebeck effect can be established. Based on their data these authors conclude that magnons and phonons have almost identical temperatures, as no systematic difference between T_m and T_p could be resolved in the BLS experiments. Figure 5.4 shows that by applying Eqs. (5.10) and (5.11) to a sample in this geometry this is a natural result: From the solution of the 1D heat transport equations, one would not expect a difference between T_m and T_p large enough to be detectable by BLS experiments. Using the material parameters for YIG and $T_\mathrm{R} - T_\mathrm{L} = 100\,\mathrm{K}$ as in the experiment by Agrawal *et al.*, a modeling based on the procedure outlined in this chapter shows that the temperature difference between the magnons and the phonons becomes substantial only very close to the edges of the sample, with $\Delta T_\mathrm{mp} \leq 20\,\mu\mathrm{K}$. However, this temperature difference is substantially smaller than the temperature stability of $\pm 0.3\,\mathrm{K}$ quoted by Agrawal *et al.*. Furthermore, according to the calculation, ΔT_mp is reasonably large only over a length of about 20 nm which is much less than the lateral resolution (40 µm) of the BLS experiment. The calculations thus corroborate the experimental observation that $T_\mathrm{m} \cong T_\mathrm{p}$ in this geometry. Turning the argument around, the agreement with the experiment supports the calculations presented in this chapter.

For many experimental geometries a 1D temperature model may not be sufficient. In this case it is appropriate to solve the temperature distribution purely numerically e.g by the 3D finite elements method (FEM). This is true in particular for a comparison with experiments at the Walther-Meißner-Institue, in which a focused laser beam is used to locally heat YIG/Pt hybrid samples [118, 170], covered in the following.

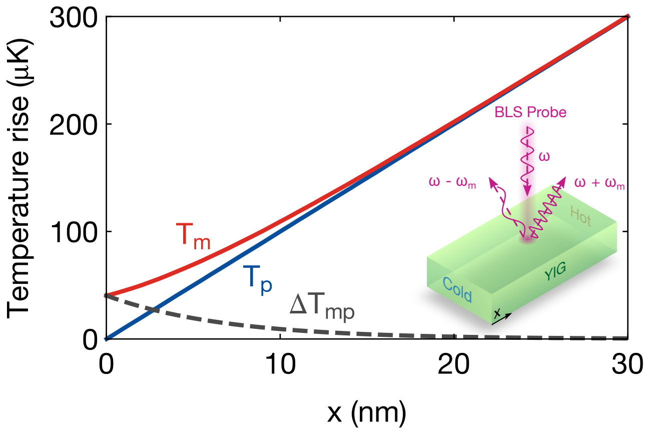

Figure 5.4.: Agrawal *et al.* [122] probed the magnon temperature in a YIG film along a longitudinal thermal gradient by Brillouin light scattering (BLS). In the BLS experiment light of frequency ω is scattered inelastically at the magnons in the YIG and reflected back to a detector. The separation $2\omega_\mathrm{m}$ of the Stokes and Anti-Stokes peaks in the reflected light spectrum is proportional to the magnon energy, from which the temperature of the magnon ensemble can be inferred [169]. The phonon and magnon temperature profiles calculated as detailed in Ch. 5.1.3 for the first 30 nm of the 10 mm long YIG film ($T_\mathrm{R} - T_\mathrm{L} = 100\,\mathrm{K}$) as investigated by Agrawal *et al.*. Only very close to the sample end at $x = 0$ (and $x = 10\,\mathrm{mm}$, not shown) a substantial temperature difference $T_\mathrm{m} - T_\mathrm{p}$ arises which is, however, still smaller than the experimental temperature stability of $\pm 0.3\,\mathrm{K}$in the BLS experiment.

The cylindrical symmetry of the problem is utilized to speed up the calculations.

In the 3D FEM, the geometry of the problem is set up first (Fig. 5.5). As with the purely analytical approach the 3D FEM allows to couple the heat equations for the phonons, electrons, and magnons as given by Eqs. (5.10) and (5.11) and calculate the temperature profiles for the three systems simultaneously. The heating by the laser light, which is here assumed to be exclusively absorbed by the electrons in the metal, is given by

$$
\begin{aligned}
P_{\mathrm{inc},i}(x,r) &= P_\mathrm{Laser}\left[\prod_{j=1}^{i}(1-R_j)\right]\exp\left[-\beta_i\left(x-\sum_{j=1}^{i-1}t_j\right)-\sum_{j=1}^{i-1}\beta_j t_j\right] \\
&\quad\times\exp\left(-2\frac{r^2}{a^2}\right), \qquad (5.27) \\
P_{\mathrm{ref},i}(x,r) &= P_{\mathrm{inc},i}(t_i,r)R_{i+1}\exp\left[\beta_i\left(x_i-\sum_{j=1}^{i}t_j\right)\right], \qquad (5.28) \\
Q_i(x,r) &= \frac{2}{\pi a^2}\left[-\frac{\partial P_{\mathrm{inc},i}(x,r)}{\partial x}+\frac{\partial P_{\mathrm{ref},i}(x,r)}{\partial x}\right], \qquad (5.29)
\end{aligned}
$$

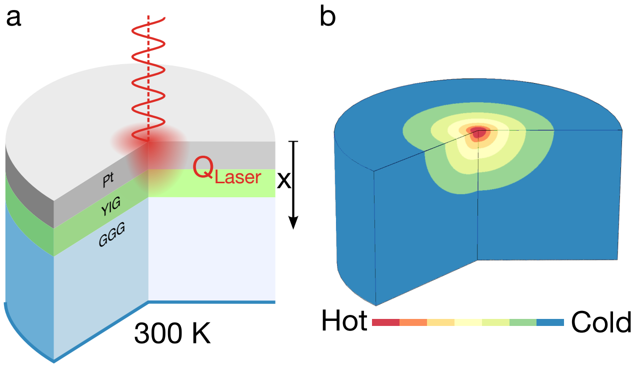

Figure 5.5.: **a** Depiction of the initial setup of the problem in the 3D FEM (not to scale). The bottom of the substrate is fixed at $T = 300\,\text{K}$, whereas the other outer borders are thermally insulating. At the Pt/YIG and YIG/GGG interfaces the interfacial thermal resistances calculated in Ch. 5.1.4 are applied. **b** Cut through a typical result obtained from a steady state simulation of the heat transfer problem with a logarithmic and capped scale of the phonon temperature rise in the simulated sample.

which is a modified version of the expression found in Ref. [129] that accounts for both the incident (P_{inc}) and reflected (P_{ref}) parts of the laser light. Here P_{Laser}, R_i, β_i, t_i, a, x and r denote the initial (optical) laser power, the reflectivity of the individual surfaces, the optical absorption coefficients (*cf.* Tab. 5.2), the layer thicknesses, the laser spot radius and the two coordinates (x, r) of cylindrical symmetry, respectively. The reflectivity R_i at the interface of the layers $i-1$ and i is computed using the Fresnel equation for normal incidence [171, 172]

$$R_i = \left| \frac{n_{i-1} - n_i}{n_{i-1} + n_i} \right|^2 , \tag{5.30}$$

where n_i denotes the complex refractive index (cf. Table 5.2) in layer i. The laser spot radius in the experiments is $a = 2.5\,\mu\text{m}$. However, as long as the laser spot is fully contained within the metalized area, i.e. the total deposited optical power remains the same, the measured voltage signals do not depend on a.

As an additional boundary condition, the lower end of the substrate is set to a fixed temperature of 300 K to simulate the effect of the copper heat sink the samples are attached to in experiment [118]. Black body radiation and convective cooling are not taken into account as their contributions in this particular geometry are much smaller than the effect of heat flow within the sample, as evident from the follow-

	absorption coefficient β (m^{-1})	refractive index n
Pt	82×10^{6} [a]	$2.41 + 4.3i$ [a]
YIG	0.5×10^{5} [b]	$2.27 + 0.003i$ [b]
GGG	$\approx 0 \times 10$ [c]	$1.96 + 0.0i$ [d]
YAG	$\approx 0 \times 10$ [a]	$1.83 + 0.0i$ [a]

[a] Reference [173] [b] Reference [91]
[c] Reference [174] [d] Reference [175]

Table 5.2.: Optical material parameters at $\lambda_{\text{Laser}} = 660\,\text{nm}$. The small absorption coefficient of YIG has been neglected in the simulations.

ing estimations based on the Stefan-Boltzmann law and Newton's law of cooling: [176]

$$\begin{aligned} P_{\text{rad}} &= \sigma A (T_{\text{sample}}^4 - T_{\text{env}}^4), && (5.31)\\ P_{\text{conv}} &= hA(T_{\text{sample}} - T_{\text{env}}). && (5.32) \end{aligned}$$

Using the Stefan-Boltzmann constant $\sigma = 5.67 \times 10^{-8}\mathrm{W}/(\mathrm{m}^2\,\mathrm{K}^4)$, the Hall bar surface $A = 80 \times 950\,\mu\mathrm{m}^2$, the heat transfer coefficient for air $h \leq 30\,\mathrm{W}/(\mathrm{m}^2\mathrm{K})$ [176] and $T_{\text{sample}} \lessapprox 400\,\mathrm{K}$ less than 0.1 mW are lost due to radiation and convective cooling which is less than 1% of the power absorbed by the sample for the typical experimental values quoted above.

Figure 5.6 shows the phonon, electron, and magnon temperature profiles at the center of the laser spot along the film normal. The inclusion of interfacial thermal resistance and the separate treatment of electrons and phonons in the platinum lead to a substantial increase in ΔT_{me} by about an order of magnitude, however, ΔT_{me} still remains at a rather low level of the order of a few millikelvins at the center of the laser spot which is barely visible in Fig. 5.6. The modeling also reveals that in spite of the strong interaction between electrons and phonons in the Pt the two are not at the exact same temperature, even in the steady state.

The simulation further show that it is unlikely that the voltages measured in experiments stem from a proximity induced anomalous Nernst effect as suggested by Huang *et al.* [79]. Using

$$V_{\text{ANE}} = -N_{\text{Nernst}}\mu_0 M_{\text{s}} \frac{2\pi}{w} \int \frac{\partial T_{\text{e}}(x,r)}{\partial x} r dr, \tag{5.33}$$

with the Nernst coefficient N_{Nernst}, the simulation shows that a Nernst coefficient of about $N_{\text{Nernst}} \approx 1 \times 10^{-3}\,\mathrm{V}/(\mathrm{KT})$ is needed to explain the measured voltage of about 100 nV in e.g.

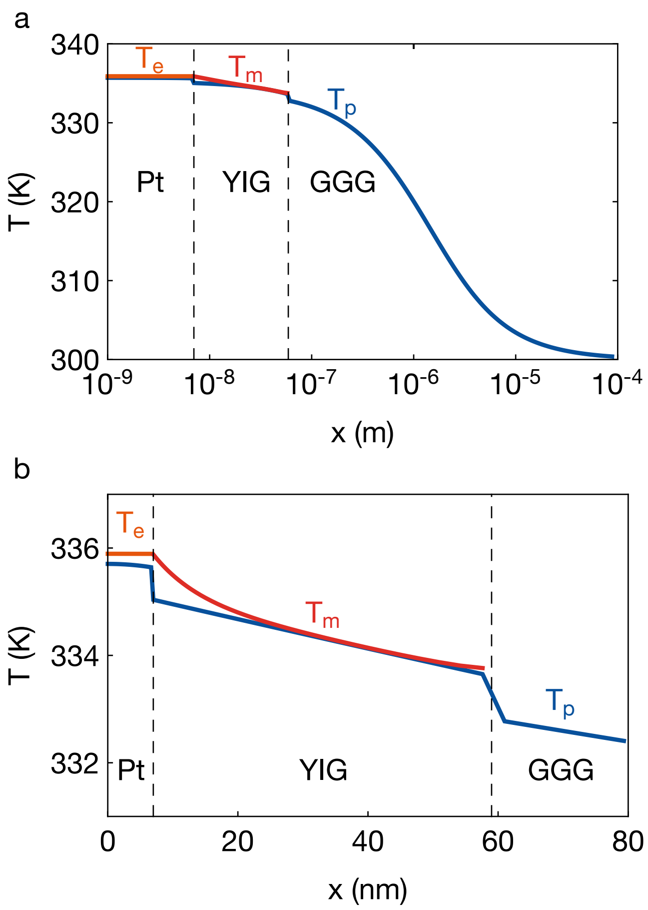

Figure 5.6.: **a** Phonon, electron and magnon temperature distributions along the optical axis of the laser beam at 10 mW laser power in a GGG(500 µm)/YIG(54 nm)/Pt(7 nm) sample calculated via 3D FEM. **b** Closeup of the thin film region.

a YIG(56.5 nm)/Pt(1.5 nm) sample at $P_{\text{Laser}} = 1\,\text{mW}$. To exaggerate the anomalous Nernst effect it is here also assumed that the entire platinum layer is evenly magnetized identical to the YIG, i.e. $M_s^{\text{Pt}} = M_s^{\text{YIG}} = 140 \times 10^3\,\text{A/m}$ and does not decay exponentially within the first few monolayers as one would expect for a static proximity polarization [177]. A Nernst coefficient of $N_{\text{Nernst}} = 1 \times 10^{-3}\,\text{V/(KT)}$ is, however, orders of magnitude larger than for instance the Nernst coefficient in bulk nickel of about $N_{\text{Nernst}}^{\text{Ni}} = 5 \times 10^{-7}\,\text{V/(KT)}$ (Ref. [178]) and cannot be motivated for magnetized platinum. It should therefore be safe to assume that potential contributions from the anomalous Nernst effect do not play any significant role in such measurements as already predicted in Ref. [118] and confirmed experimentally in Ref. [82].

Lastly, the ΔT_{me} extracted from the calculated temperature profiles can also be used to predict the experimentally measured voltages. It is important to note that the following hinges on the assumption that magnons of all frequencies contribute to the measured spin currents in the manner expected by Xiao *et al.*. The pitfalls and potential issues with this approach have already been discussed above and are further elaborated on in Ch. 5.1.7. Nevertheless, the evaluation in terms of Xiao *et al.*'s assumptions, allows a further, if only approximate, comparison between simulation (theory) and experiment.

The samples in these experiment were fabricated as described in Ch. 3, subsequently patterned into Hall bar mesa structures (width $w = 80\,\mu\mathrm{m}$, length $l = 950\,\mu\mathrm{m}$) using optical lithography and Argon ion beam milling, mounted in a chip carrier system, and inserted into a home-built 2D vector magnet. Here, a scanning focused, laser beam is used to locally heat the samples [118]. All spin Seebeck effect experiments were performed at room temperature.

To connect the experimentally measured voltages with the numerically calculated temperature profiles Eq. (5.2) is adjusted to account for the inverse spin Hall effect (Ch. 2.2) and spin diffusion in the Pt (Ch. 2.1) and then reads

$$V_{\mathrm{SSE}} = \frac{g_{\mathrm{r}}\gamma\hbar k_{\mathrm{B}}}{2\pi M_{\mathrm{s}} V_{\mathrm{a}}}\Delta T_{\mathrm{me}} \cdot \frac{2e}{\hbar}\theta_{\mathrm{SH}}\rho l \cdot \eta \cdot \frac{\lambda}{d_{\mathrm{N}}}\tanh\left(\frac{d_{\mathrm{N}}}{2\lambda}\right), \tag{5.34}$$

where the backflow correction factor [28, 47]

$$\eta = \left[1 + 2g_{\mathrm{r}}\rho\lambda\frac{2\pi e^2}{\hbar}\coth\left(\frac{d_{\mathrm{N}}}{\lambda}\right)\right]^{-1} \tag{5.35}$$

is taken from spin pumping as an expression for the spin Seebeck effect has not been established yet. The notation in the equations above follows that introduced in Ch. 2, i.e. θ_{SH} is the spin Hall angle [179], ρ is the electrical resistivity of the sample, l is the length of the sample (the distance between the voltage contacts, *cf.* Ch. 6.2), $g_{\mathrm{r}} = \mathrm{Re}\left(g^{\uparrow\downarrow}\right)$ is the real part of the spin mixing interface conductance per unit area [127], $\gamma = g\frac{e}{2m}$ is the gyromagnetic ratio with g as the Landé g-factor and the electron mass m, $e = |e|$ is the elementary charge, k_{B} is the Boltzmann constant, $\hbar$ is the Planck constant, M_{s} is the saturation magnetization of the magnet λ is the spin diffusion length in the normal metal, and d_{N} is the thickness of the normal metal film.

Since only a small area is heated in these experiments a single ΔT_{me} can not be given, due to the lateral spread of the temperature distributions. Additionally, the charge current that is eventually created by the spin Seebeck and inverse spin Hall effect is effectively short-circuited by the non-heated region such that one needs to substitute the term $l\Delta T_{\mathrm{me}}$ in Eq. (5.34) by the integral expression

$$l\Delta T_{\mathrm{me}} \equiv \frac{2\pi}{w}\int \Delta T_{\mathrm{me}}(r) r dr, \tag{5.36}$$

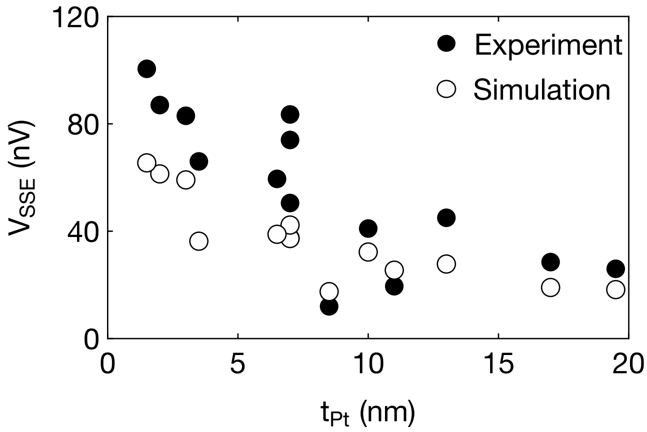

Figure 5.7.: Comparison of the observed and computed spin Seebeck voltages under local laser heating. Experimental and simulated data are normalized to an incident laser power of 1 mW. The ΔT_{me} in Eq. (5.34) is calculated with the sample parameters from Tabs. 5.1–5.3 and the magnon properties outlined in Ch. 5.1.5.

where $w = 80\,\mu\mathrm{m}$ is the width of the Hall bar. Using this $l\Delta T_{\mathrm{me}}$, where ΔT_{me} is averaged over the magnetic coherence length, just as in the one-dimensional case, one can now compare the spin Seebeck effect expected from theory with experiment. Note that $l\Delta T_{\mathrm{me}} = |l\Delta T_{\mathrm{me}}|$ is adopted in the following for clarity.

Figure 5.7 shows a comparison between the voltages measured in the local laser heating setup and theoretical values obtained from Eq. (5.34) for the YIG/Pt heterostructures listed in Table 5.3. For e.g. a YIG(54 nm)/Pt(7 nm) sample (also shown in Fig. 5.7), a voltage $V_{\mathrm{SSE}} = 74\,\mathrm{nV}$ is observed for $P_{\mathrm{laser}} = 1\,\mathrm{mW}$ at the sample surface. Using $g_{\mathrm{r}} = 1 \times 10^{19}\,\mathrm{m}^{-2}$ [47, 48], $\theta = 0.11$ [47, 48], $\lambda = 1.5\,\mathrm{nm}$ [47, 48], $M_{\mathrm{s}} = 140 \times 10^{3}\,\mathrm{A/m}$ [180], and the value $l\Delta T_{\mathrm{me}} = 1.35 \times 10^{-9}\,\mathrm{Km}$ obtained for 1 mW optical laser power from the numerical calculations, yields $V_{\mathrm{SSE}} = 37\,\mathrm{nV}$ from Eq. (5.34) in good agreement with the experiment. Generally this approach seems to slightly underestimate V_{SSE}, but generally gives values that agree with experiment to within a factor of two. Considering the uncertainties in the determination of the magnon parameter set and the issues with the magnon spectral distribution, the modeling seems to generate realistic temperature profiles.

5.1.7 *Summary*

The calculations presented in this chapter enable to investigate temperature profiles of several interacting subsystems on a nanometer scale also in magnetic materials. The model has subsequently suc-

Sample	$\rho(\mathrm{n\Omega m})$	$l\Delta T_{\mathrm{me}}(10^{-9}\,\mathrm{Km})$
GGG/YIG(50)/Pt(7)	409.4	1.35
GGG/YIG(54)/Pt(7)	406.5	1.35
GGG/YIG(46)/Pt(3.5)	306.6	0.96
GGG/YIG(58)/Pt(2)	761.7	0.78
GGG/YIG(56.5)/Pt(1.5)	1089.9	0.73
GGG/YIG(61)/Pt(11)	334.5	1.63
GGG/YIG(53)/Pt(8.5)	348.3	0.85
GGG/YIG(52)/Pt(17)	331.7	1.90
YAG/YIG(59)/Pt(7)	487.7	1.36
YAG/YIG(64)/Pt(3)	622.2	0.92
YAG/YIG(61)/Pt(19.5)	358.7	1.97
YAG/YIG(63)/Pt(6.5)	412.0	1.31
YAG/YIG(60)/Pt(10)	429.0	1.58
YAG/YIG(60)/Pt(13)	434.9	1.75

Table 5.3.: Samples used in this study. Numbers in parentheses indicate layer thickness in nm (rounded to the next 5 Å). $l\Delta T_{\mathrm{me}}$ denotes the integrated temperature difference between the magnons and the electrons at the YIG/Pt interface at $P_{\mathrm{Laser}} = 1\,\mathrm{mW}$.

cessfully been used to investigate the spin Peltier effect [181] and time resolved spin Seebeck experiments [182] by other authors. It should be noted again that the modeling of thermally coupled heat reservoirs had originally been devised decades ago and was only complemented with spin current based heat transport by Xiao *et al.* [12]. Nevertheless, the coupled magnon-phonon(-electron) system had not been studied in complex, realistic geometries or implemented in a manner that respects the details of spin current based heat transport. Further, the significance of the spin current based heat transport was originally dismissed by Xiao *et al.* but found to be essential when realistic material parameters are employed. While the coupling in the YIG/Pt samples investigated here is mostly restricted to two coupled systems (with the coupling to the third realized via an interface effect), terms of the form of Eq. (5.9) can easily be added for an arbitrary number of interacting subsystems. While this may render a analytic solutions of even simple cases impossible, numeric procedures will only suffer some moderate increase in computational cost. This makes the results particularly interesting for futures studies on e.g. conducting magnets or materials with exotic forms of heat transport. Numeric procedures, in principle, also allow to investigate the transient evolution of the temperature profiles. When the timescales approach the magnon phonon interaction time, however, a treatment in terms of temperatures may not be appropriate anymore. Since the magnon phonon interaction time is not independent of the magnon energy [*cf.* Eq. (5.25)] low-energy magnons will behave differently from high-energy ones as discussed further in Ch. 5.2. Instead of temperatures one would then need to consider the evolution of arbitrary distributions that relax towards a Bose-Einstein (Fermi-Dirac) profile for $t \to \infty$. To account for the energy dependence of the interaction constants the governing differential equations will then form a system of integro-differential equations. While all this appears feasible to do numerically, the lack of reliable information on the (energy dependent) interaction times requires further theoretical modeling. The micro magnetics approach by Ritzmann *et al.* [68] avoids some of these issues and yields similar information, but is limited to the simulation of small scale systems due to the rather extensive computational cost.

At the beginning of this chapter it was pointed out that more recent results suggest that the inverse spin Hall voltage measured in experiments originates from the low-energetic end rather than from the whole magnon spectrum. Indeed, also the calculated temperature profiles show that the absolute temperature difference between magnons and electrons at the magnet/normal metal interface is very small. Thus additional care is required regarding the comparison of experimental data with model predictions. By only considering low-energy magnons the temperature gradient induced spin current and, in turn, the predicted spin Seebeck voltage would be reduced considerably. At the same time, however, the *effective* ΔT_{me} (i.e. the accumulation of low-energetic magnons) is likely to be much higher in this case due to the influx of additional low-energetic magnons driven by the temperature gradient in the magnet. It is clear that a more robust knowledge of the precise composition of the magnon spectrum at the interface is required before further attempts to model experimental voltages are to be undertaken. Current efforts aimed at obtaining such information are discussed in the following chapter.

5.2 TRANSIENT SPIN SEEBECK EFFECT

The resonant excitation of the magnetization dynamics in a solid is only possible for selected magnetic field-frequency combinations [*cf.* Eq. (2.10)]. By the same argument, the magnons in spin pumping experiments can unambiguously be identified from the experimental conditions and their wave vector can be inferred from the dispersion relation [Eq. (2.3)]. In a non-resonant excitation scheme used in spin Seebeck experiments, however, magnons of all frequencies and wave vectors contribute to the spin currents measured in experiment. The model employed in Ch. 5.1 assumed the magnon distribution to be described by a Bose-Einstein distribution, but it was pointed out that this assumption may not be valid at the edges of a magnet, i.e. at an interface. In the steady state it is difficult to distinguish between magnons of different frequencies and thus infer the magnon distribution from measurement data. This severely limits the significance of most of the experiments performed to date as they were performed on time scales corresponding to the static regime. To get insight into the spectral distribution of the involved magnons therefore requires experiments in a transient regime, where the relevant relaxation times become larger, or at least comparable to, the time scale probed in the measurement.

Two independent studies aimed at quantifying the magnon-phonon interaction time relevant for the spin Seebeck effect. They employed a modulated laser heating scheme, similar to that presented in Ch. 5.1, allowing for the generation of temperature gradients on a sub-microsecond scale. Unfortunately the results of these experiments on yttrium iron garnet (YIG)/Pt samples were not conclusive. On the one hand, Agrawal *et al.* [182] observed a roll-off frequency of the spin Seebeck voltage below 1 MHz in a several micrometer thick film and attributed it to a finite "effective thermal magnon diffusion length". On the other hand, the experiments by Roschewsky *et al.* [183] in much thinner YIG films suggest that the spin Seebeck effect should be robust even beyond several 10 MHz.

To resolve this apparent disagreement an experimental study of the transient behavior of the spin Seebeck effect on a series of samples with YIG thicknesses $50\,\mathrm{nm} \leq d_\mathrm{F} \leq 53\,\mu\mathrm{m}$ has been performed in collaboration with the Technische Universität Kaiserslautern. The investigation reveals that the characteristic decay time of the spin Seebeck effect changes as a function of the YIG layer thickness. The spin Seebeck voltages in the experiments show 3 dB cut-off frequencies as high as 0.35 GHz in the thinnest investigated YIG films, but drop to below 1 MHz when the thickness of the YIG films exceeds 1 µm. This is consistent with the notion that the energies of the magnons generating the measured spin Seebeck voltage increase with decreasing the YIG film thickness due to confinement [120]. Furthermore,

the evolution of the measured spin Seebeck voltage with the heating modulation frequency and the thickness of the YIG layer provides further evidence to reports in the literature [120] that the magnon spectrum stimulating the spin current emission characteristically changes with the YIG thickness. The results strengthen the impression raised throughout Ch. 5.1 that a simple diffusion model can only approximate the magnon distribution in systems with strongly wave vector dependent interaction mechanisms.
This chapter is based on a manuscript on the same topic prepared for submission for peer-review and adopts much of its text and figures.

5.2.1 *Preparation of the experiment*

The YIG films used in the experiments were fabricated using two complementary methods which allow to cover a large range of YIG film thicknesses. The growth of the thinner films ($d_F \leq 200\,\mathrm{nm}$) follows the description outlined in Ch. 3 (pulsed laser deposition of the YIG) with yttrium aluminium garnet (YAG) used as a substrate. The Pt coverage ($\approx 10\,\mathrm{nm}$) varies by a few nanometer from sample to sample, but is not expected to have a significant impact on the analysis. Thicker YIG films are commercially fabricated by means of liquid phase epitaxy on gadolinium gallium garnet (GGG) substrates and were subsequently covered with Pt. For the analysis in the following potential spurious contribution due to the anomalous Nernst effect are disregarded, in agreement with the notion that the proximity polarization in Pt is negligible [81], i.e. at least two orders of magnitude smaller than the spin Seebeck effect in YIG/Pt [82].

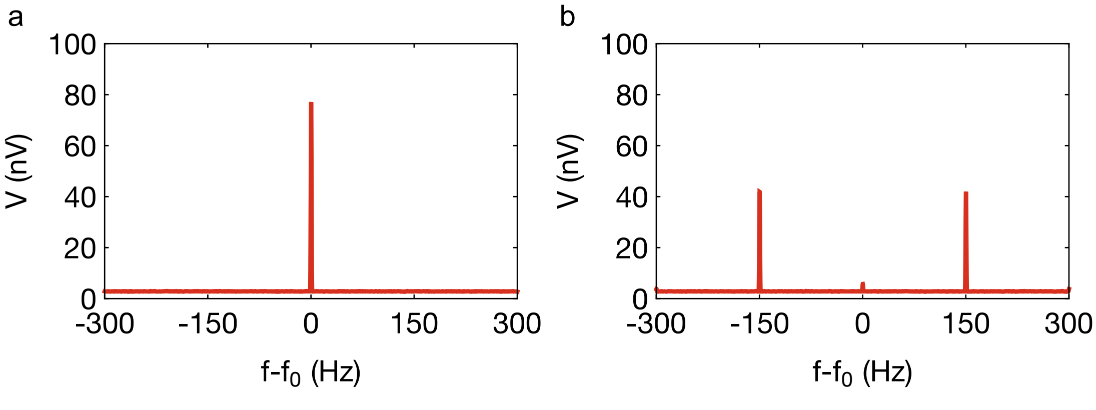

Figure 5.8.: **a** Spin Seebeck voltage spectrum of the YIG(50 nm) sample recorded by the spectrum analyzer for a microwave frequency $f_0 = 2\,\mathrm{MHz}$ and a static magnetic field $\mu_0 H_{\mathrm{ext}} \approx 20\,\mathrm{mT}$. **b** Voltage spectrum for a continuously rotating ($f_{\mathrm{mod}} = 150\,\mathrm{Hz}$) magnetic field of the same strength. The formerly single peak splits into two peaks of half the original height.

Two different experimental approaches were employed to investigate the spin Seebeck effect dynamics. At the Walther-Meißner-Institut a continuous wave solid-state laser with a wavelength of 1550 nm is modulated at a frequency f by an electro-optical modulator to generate a sinusoidal intensity modulation of the laser beam with a peak-to-peak amplitude of about 30 mW and thus generates a time-varying temperature gradient in the samples. The induced time-varying spin Seebeck voltage is detected and averaged by a spectrum analyzer. The amplifier used to drive the electro-optical modulator, unfortunately, emits a large amount of electromagnetic radiation at the microwave frequency f, which is picked up by the wiring connected to the spectrum analyzer and contaminates the measurement of the spin Seebeck signal detected at the same frequency. To circumvent this issue the double modulation method derived in Ch. 4 is employed. More specifically, in addition to a modulation of the spin Seebeck voltage signal at the microwave (laser heating) frequency f the magnetic field applied to the samples is rotated continuously during the measurements at a frequency f_{mod}. In the same fashion as demonstrated in Eq. (4.7), the rotation of the magnetic field splits the spin Seebeck voltage peak into two sidebandes at $f \pm f_{\mathrm{mod}}$, but leaves the frequency of the inductive signal unaffected. This is exemplarily shown in Fig. 5.8 for the YIG(50 nm) sample at a microwave frequency $f(\equiv f_0) = 2\,\mathrm{MHz}$. While a single peak is observed for a static magnetic field in Fig. 5.8a, the spectrum is composed of two peaks of half the original height in Fig. 5.8b for a magnetic field rotating at $f_{\mathrm{mod}} = 150\,\mathrm{Hz}$. The reamining voltage detected at the microwave frequency is the inductive pick-up signal, which is small here, but can exceed several dozens of microvolts at larger microwave frequencies. In addition to the separation from spurious voltages the integrity of the voltage signals is further validated via S-parameter measurements. The latter ensure that bandwidth limitations of the electric circuit are not at the origin of the observed frequency dependence.

At the Technische Universität Kaiserslautern (UniKL) samples are placed on top of a microstrip line, covered by an insulating layer. By application of 30 dBm microwave ($f_{\mathrm{mw}} = 6.875\,\mathrm{GHz}$) pulses to the microstrip line, eddy currents are induced in the Pt, which, in turn, generate a time-varying temperature gradient across the YIG/Pt interface [184]. After passing a low-pass filter, the voltages are detected by a spectrum analyzer at the microwave modulation frequency f.

Both experiments, upon repeating the procedure for different modulation frequencies, directly yield the characteristic frequency response transfer function $|V_{\mathrm{SSE}}|(f)$, i.e. the magnitude of the voltage response as a function of the frequency of the applied temperature gradient. With applied magnetic fields of the order of 25 mT the experiments are performed far below ferromagnetic resonance and parametric excitation conditions.

5.2.2 *Experimental results*

The transfer functions $|V_{\mathrm{SSE}}|(f)$ for samples YIG (50 nm), YIG(270 nm), YIG(2800 nm) and YIG(30 000 nm) are exemplarily shown in Fig. 5.9. The absolute voltage levels scale with the thickness of the YIG layer as reported in Refs. [75, 120], however, here the data have been normalized to the respective DC value for each sample for clarity. Evidently, the spin Seebeck voltage on the 50 nm film remains at its DC level up to much higher frequencies as compared to the other samples. Moreover, the voltage response for frequencies above the 3 dB point is markedly different for the various samples. For the 50 nm and 270 nm films the transfer function resembles a classical first order low-pass, decaying as $1/f$ for $f \gg f_{3\,\mathrm{dB}}$. In contrast, $|V_{\mathrm{SSE}}|(f)$ measured for the 2800 nm and 30 000 nm film decays at a much lower rate. A gradual change of both the cut-off frequency as well as the shape of the transfer function is observed as a function of YIG thickness in the sample series.
Since the transfer functions of the investigated samples clearly cannot all be modeled with the same approach (e.g. a low-pass as above), the cut-off (3 dB) frequencies $f_{3\,\mathrm{dB}}$ for all samples are determined solely by the frequency at which $V_{\mathrm{SSE}}(f_{3\,\mathrm{dB}}) = V_{\mathrm{SSE}}(f \to 0)/\sqrt{2}$. The result is plotted in Fig. 5.10 and indicates a power-law like behavior of the cut-off frequency $f_{3\,\mathrm{dB}} \propto d_{\mathrm{F}}^{\beta}$ as a function of the YIG film thickness d_{F} with an exponent $\beta \simeq -1$.

The interpretation of the experimental results requires reiterating some theoretical concepts. Within the spin mixing interface conductance formalism [38] an energy imbalance [185] between the two sides of a magnet/normal metal interface leads to the flow of angular momentum across the latter. For the spin Seebeck effect this energy difference may be formulated in terms of a temperature difference between electrons in the normal metal and magnons in the ferromagnet as detailed in Ch. 5.1. While the temperature difference in Ch. 5.1 was assumed to originate from diffusive [12] transport, other scenarios, such as stochastic transport [68] or "subthermal" magnons [64, 66, 72], have also been proposed in the literature. Irrespective of the modeling employed, however, low temperature measurements [72] and the relatively long lifetime time of the small wave number k magnons [156] even at room temperature suggest that the thermalization process between magnons and phonons is the limiting factor for high-frequency spin Seebeck excitations. It is important to realize that the calculations in Ch. 5.1 are concerned

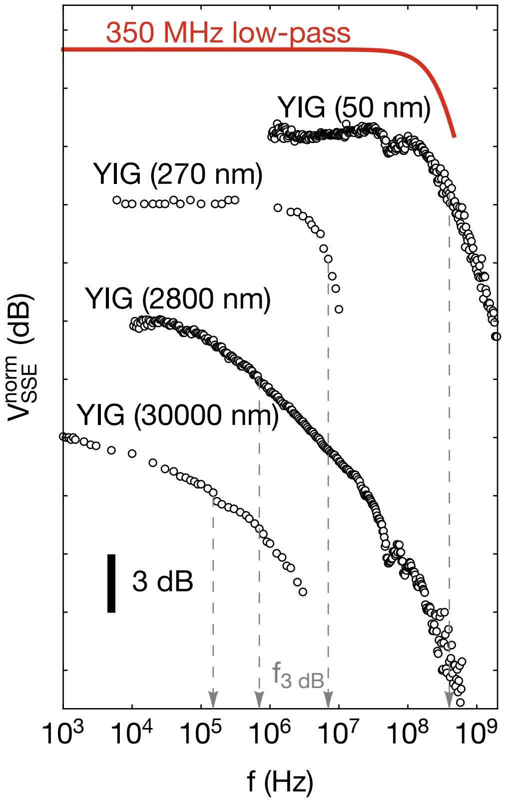

Figure 5.9.: Normalized spin Seebeck voltage $V_{\mathrm{SSE}}(f)/V_{\mathrm{SSE}}(0)$ as a function of the modulation frequency of the applied temperature gradient for the 50 nm and 2800 nm thick YIG films recorded at the WMI and the 270 nm and 30 000 nm thick YIG films recorded at the UniKL. Offsets have been added to the data for clarity. The dashed lines indicate the 3 dB points and the solid line depicts the behavior of a 350 MHz low-pass for comparison.

exclusively with the steady state, where the shorter lifetimes of high-energy magnons are much more relevant due to the mutual coupling between magnons of different energy. The interaction with the other thermal reservoir, the electrons in the normal metal, can be assumed instantaneous in the experimentally accessed frequency range as spin current emission has been demonstrated for much higher frequencies, e.g. in spin pumping [56] or spin Hall magnetoresistance [186] experiments.

To explain the observed frequency dependence of the spin Seebeck voltage a steady-state model [64, 181] as in Ch. 5.1 is considered first. The energy supplied to the Pt layer by the laser heating raises the temperature of the Pt layer. Energy and angular momentum are then transferred by the spin transfer torque from the electrons in the Pt to the magnons in the YIG, raising the magnon temperature T_{m}. Due

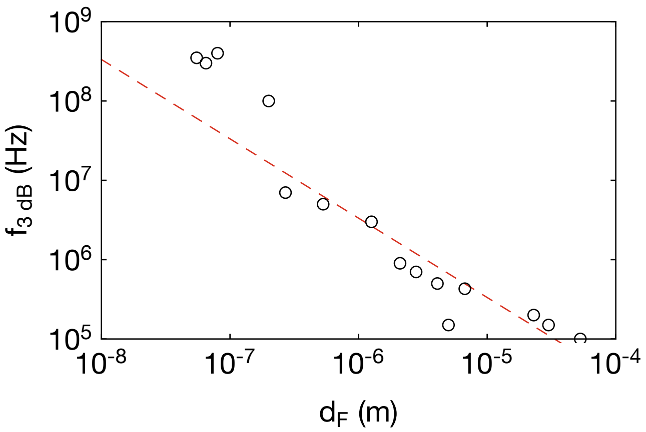

Figure 5.10.: 3 dB roll-off frequency as a function of the YIG film thickness. $f_{3\,\mathrm{dB}}$ gradually decreases as approximately d_F^{-1} indicated by the dashed line.

to magnon-phonon scattering the energy is finally transferred to the phonon system and the heat sink. In the stationary situation a steady-state spin current is generated across the YIG/Pt interface which is proportional to the temperature difference $\Delta T = \Delta T_\mathrm{me} = T_\mathrm{e} - T_\mathrm{m}$ of the electrons in Pt and the magnons in YIG. It is obvious that a finite ΔT and, hence, a finite spin Seebeck voltage is obtained only if the magnons couple to the phonons as magnons and electrons would equilibrate almost instantaneously otherwise ($\Delta T \to 0$). This is important for the non-stationary case. A finite ΔT_me is obtained only on time scales longer than the characteristic magnon-phonon interaction time τ_mp in YIG. On shorter time scales, the energy cannot be transferred from the magnon to the phonon systems resulting in $\Delta T \to 0$. Following the derivation in Ch. 5.1, and disregarding any spatial variation, the time evolution of the temperature difference ΔT_mp between the magnons and phonons in YIG can be expressed in a relaxation time approach as [124]

$$\frac{d}{dt}\Delta T_\mathrm{mp} = -\frac{\Delta T_\mathrm{mp}}{\tau_\mathrm{mp}}. \tag{5.37}$$

This is trivially solved by $\Delta T_\mathrm{mp}(t) \propto e^{-\frac{t}{\tau_\mathrm{mp}}}$, which transforms to

$$\left|\Delta T_\mathrm{mp}(\omega)\right| \propto \frac{1}{\sqrt{1+\left(\omega\tau_\mathrm{mp}\right)^2}} \tag{5.38}$$

in the frequency domain. The transfer function derived from this model indeed describes the data of the 50 nm and 270 nm film reasonably well. Following this reasoning the cut-off frequency in the 50 nm film thus corresponds to a characteristic interaction time between magnons and phonons of $\tau_\mathrm{mp} = 1/(2\pi f_{3\,\mathrm{dB}}) \approx 450\,\mathrm{ps}$. This is consistent with the estimate in Ch. 5.1 and others the literature [168] which put τ_{mp} at a few hundred picoseconds for high-energy magnons. It should be pointed out, however, that the extracted τ_{mp} is a weighted average over the entire magnon spectrum contributing to the emission of the measured spin current. Keeping in mind that τ_{mp} is expected to be strongly frequency dependent, further explains why the transfer function for the thicker films deviates significantly from Eq. (5.38).

In thermal equilibrium and in absence of any spatial variation of the temperature, the magnon population is distributed according to Bose-Einstein statistics and can be described with a single magnon temperature T_{m}, as done in Ch. 5.1 where the YIG film thicknesses did not exceed a few ten nanometers. A thermal gradient, however, is accompanied by a flow of magnons along the same direction, with the diffusion length of individual magnons decreasing with their energy [15]. The different diffusion lengths become important at the edges (interfaces) of the magnetic layer at which only magnons closer than their respective diffusion length can accumulate. Increasing the magnetic layer thickness then favors lower energetic magnons with their longer diffusion lengths in the interface accumulation. This also implies that increasing the thickness of the ferromagnet leads to a growing deviation from Bose-Einstein statistics right at the interface and the concept of a single temperature is no longer well defined [187]. According to numerical simulations [68] this effect is small for our thinnest films but should be more significant in thicker ones. At any rate, the magnon spectrum is expected to show an exponential relaxation, similarly to Eq. (5.37). The lowest energetic magnons (i.e. those with frequencies close to the ferromagnetic resonance frequency) feature interaction times with phonons exceeding a microsecond. The shift of the effective cut-off frequency to lower values in thicker YIG films observed in the experiment is thus expected from the model. More specifically, Etesami *et al.* [69] derive the functional dependence of the 3 dB roll-off frequency $f_{3\,\mathrm{dB}}$ for a given magnon mode $n \in \mathbb{N}_0$ on d_{F} as

$$f^{n}_{3\,\mathrm{dB}} = \alpha \frac{\gamma}{2\pi} \left[B_0 + \frac{2A_{\mathrm{ex}}}{M_{\mathrm{s}}} \left(\frac{2n\pi}{d_{\mathrm{F}}} \right)^2 \right] , \tag{5.39}$$

where α is the magnetization (Gilbert) damping, γ is the gyromagnetic ratio, B_0 is the external magnetic field, A_{ex} is the exchange constant, M_{s} is the saturation magnetization and $n \in \mathbb{N}_0$ determines the magnon wavenumber. The full transfer function is then a linear combination of the low-pass behavior of the individual magnon modes. As d_{YIG} increases, the mode number n for magnons still effective at a given energy increases and more lower energetic modes become available. Since these lower energetic modes feature smaller $f^{n}_{3\,\mathrm{dB}}$ values [*cf.* Eq. (5.39)] the total $f_{3\,\mathrm{dB}}$ shifts downwards, at a rate determined by the mode occupation number, i.e. the composition of the magnon spectrum. The d_{F}^{-1} behavior observed in Fig. 5.9 is qualitatively consistent with an increased weight of the lower energetic end of the magnon spectrum in thicker films. In any case, the $f_{3\,\mathrm{dB}}$ values plotted Fig. 5.10 may be understood as approximate values of the dominant magnon mode. It is important to emphasize that this approximation becomes increasingly crude when many modes with different $f^{n}_{3\,\mathrm{dB}}$ values contribute similarly to the total signal in thicker YIG films. With this caveat in mind $f_{3\,\mathrm{dB}}$ in Fig. 5.10 is related to the characteristic magnon energy stimulating the spin current emission via

$$E = \hbar\omega = \frac{2\pi\hbar}{\alpha} f_{3\,\mathrm{dB}}. \tag{5.40}$$

Considering the different damping characteristics of the films grown by pulsed laser deposition ($\alpha \approx 10^{-3}$ [99], Ch. 7.2) and liquid phase epitaxy ($\alpha \approx 10^{-4}$ [59, 64, 158, 159]) characteristic energies of the order of 1 meV are obtained in the thinnest films. Converting the energy into an *effective* temperature yields $T_{\mathrm{eff}} \approx 17\,\mathrm{K}$ in the 50 nm YIG film. This is in good agreement with the results by Boona and Heremans [72] and Jin *et al.* [121] who give an upper temperature limit for the magnons contributing to the spin current of 30 K to 40 K. From a didactic perspective, however, it appears questionable to refer to a subset of the magnon spectrum by means of its "temperature", rather than its energy. Although themed "low-energy magnons" here, the characteristic frequencies of the magnons (up to few THz) are substantially larger than those typically investigated in ferromagnetic resonance experiments (few GHz). Still, the characteristic energies of the order of 1 meV at best renders these magnons rather low energetic compared to the energy scale suggested by the room temperature measurements and considered in the calculations in Ch. 5.1.

Finally, it is important to note that caution is required regarding the values derived from the experiments. It is clear that there is some leeway in the interpretation of the raw experimental data and that the different sample fabrication methods and related variations in e.g. magnetic damping in the films affect the accuracy of the derived numerical values. Additionally the possible influence of a thermal skin effect [188], i.e an attenuation and confinement of the heating to the surface of the sample at high frequencies, is not explicitly accounted for in the above analysis. The thermal skin effect arises from the finite size and specific heat of the sample and attenuates the magnitude of the temperature modulation with increasing the heating frequency (which itself is left unaffected) as a function of the distance to sample surface. If one takes the average heating within the YIG layer as a measure for the magnitude of the spin Seebeck effect then the larger heat capacity in thicker (more voluminous) magnetic films alone may be sufficient to qualitatively explain the observed $1/d_{\mathrm{F}}$ dependence. However, the thermal properties of the underlying and much thicker YAG or GGG substrates are not all that different from those of YIG (*cf.* Tab. 5.1) and thicker magnetic layers should thus only marginally affect the significance of the thermal skin effect. Hence, the magnitude of the attenuation at each point should be agnostic to the YIG film thickness and thus fundamentally the same for all samples. Similarly the characteristic diffusion length $l_\mathrm{k} = 2\sqrt{\mathrm{k}\tau}$ [189], quantifying the penetration depth of the heating within a given time frame τ for a material with diffusivity k ($\mathrm{k}_\mathrm{YIG} = 5.6 \times 10^{-5}\,\mathrm{m^2 s^{-1}}$ [190]), is larger than the magnetic film thickness for all samples and their respective 3 dB time constants. This estimate, however, is rather coarse and it may still be possible that some of the observed attenuation in YIG films thinner than the magnon mean free path [182] could be a residue of the above phenomenon. All these issues aside, however, the extracted values appear to be consistent with literature and are further supported by the $f_{3\,\mathrm{dB}}(500\,\mathrm{nm})$ value of some ten megahertz inferred from numerical simulations in Ref. [69].

5.2.3 *Summary*

Chapter 5.2 investigated the frequency dependence of the spin Seebeck effect and identified characteristic response times which depend on the thickness of the YIG layer. Specifically, it was found that the characteristic response time scales approximately as the inverse thickness of the films. This is consistent with recent experimental and theoretical studies and supports the notion that high-frequency magnons dominate the effect in thin films but are less important for its absolute magnitude and frequency dependence in thicker ones. The results allow to develop a consistent picture of the physics behind the spin Seebeck effect, providing a link between several recent experimental [72, 75, 120, 121, 182, 183] and theoretical [68, 69, 168] results. They could further help to refine the modeling by Xiao *et al.* [12] employed in Ch. 5.1 and in the literature [168, 181], in a manner that it also correctly predicts the temperature (magnon distribution) at the interface of thick magnetic films and promotes a more robust understanding of the conversion into the voltages measured in experiments.

Going beyond the scope of the experiments presented here, further insights might be gained by systematically studying the effect of large magnetic fields and low temperatures on the dynamics. Large magnetic fields have already been demonstrated to affect the DC properties [120], an effect which should also translate to the transient response. The approach presented here could also provide further insight into the spectral composition of the thermally induced spin currents in compensated garnets [71] with non-trivial contributions from different magnetic sublattices.

5.3 CURRENT HEATING INDUCED SPIN SEEBECK EFFECT

In most spin Seebeck experiments, the controlled generation and quantification of temperature gradients represents a challenge. The temperature gradients are most often established by clamping the sample between two heat reservoirs, acting as heat source and sink [10, 80, 82, 117, 119]. An important issue in this type of spin Seebeck effect setup is good thermal coupling between the heat reservoirs and the sample. The laser heating technique [118] employed in Ch. 5.1 and Ch. 5.2 circumvents this issue and brings along some other benefits. However, the temperature gradients thus generated can be quantified only by numerical methods as demonstrated in Ch. 5.1. A fundamental issue with both techniques is that they require dedicated, often custom made or expensive, equipment to perform the experiments. This is particularly challenging when the experiments are not to be performed at ambient conditions, e.g. in a cryostat. Scaling these techniques towards larger or smaller samples than what they were originally designed for is also not always possible.

This chapter presents an alternative, very simple technique to generate the temperature gradients required in spin Seebeck experiments. The main idea is to use the normal metal layer (e.g. the Pt layer in YIG/Pt) itself as an on-chip resistive heater. Although a large heating current is driven through the normal metal, it is possible to simultaneously record the spin Seebeck magnetothermal (i.e. spin Seebeck) voltage, by exploiting its dependence on an external magnetic field and the heating current polarity.

This technique will be used for some of the data acquisition in Ch. 6 and has already found widespread adoption in the community [71, 76, 77, 191, 192]. This chapter is based on the results published in Appl. Phys. Lett. 103, 242404 (2013) with extensive reuse of text and figures.

5.3.1 *Theoretical concept*

As outlined in Ch. 2.5 and Ch. 5.1, the spin Seebeck effect is generated by the flow of heat in a magnet and through the magnet/normal metal interface. By driving a large heating current I_d through the normal metal the latter can act as a resistive heater and generates the required thermal gradient (Fig. 5.11). For most experimental configurations, the associated (resistive) voltage drop V_d along the direction of current flow will, however, be far larger than the ensuing spin Seebeck voltage. On the other hand, most of V_d will be insensitive to external magnetic fields, while the spin Seebeck effect voltage V_iSSE is connected to the external magnetic field via the inverse spin Hall effect as given in Eq. (2.7). A complication arises in the form of an

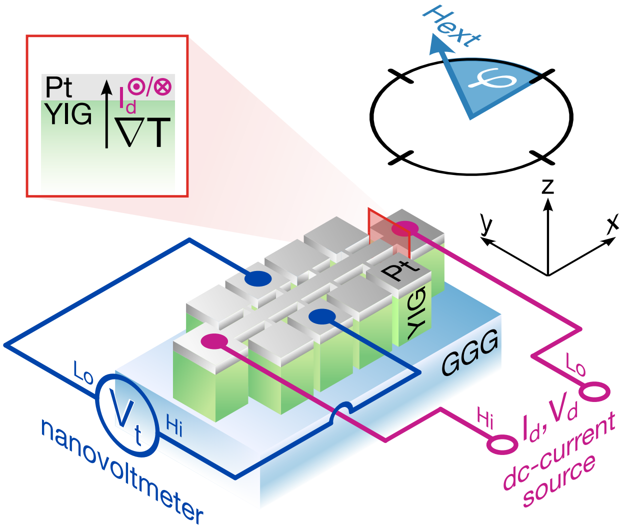

Figure 5.11.: Sketch of the setup used for the current heating induced spin Seebeck experiments. The samples consists of magnetic insulator (YIG) thin films on single crystalline GGG or YAG substrates covered by a thin normal metal (Pt) film. The YIG/Pt bilayer is patterned into a Hall bar mesa structure. A DC-current source is used to drive a large current I_d through the Hall bar while the voltage drop V_t transverse to the current direction is measured with a nanovoltmeter. An external, in-plane, magnetic field is applied at an angle φ to the current direction. Due to the resistive (Joule) heating by I_d a temperature gradient across the magnet/normal metal interface emerges, giving rise to the spin Seebeck effect.

additional magnetic field dependent contribution V_res due to magnetoresistive effects such as the spin Hall magnetoresistance (see Ch. 2.3 and Ch. 4) Typically, these magnetoresistive voltages will be much larger than the V_iSSE of interest. A method to increase the visibility of V_iSSE with respect to V_d is to measure V_iSSE in the direction transverse (along $\boldsymbol{y}$) to the heating current, where V_d (along $\boldsymbol{x}$) vanishes. However, even in this case the longitudinal voltage V_d can contribute to V_t due to a slight misalignment of the transverse contacts, as will the magnetoresistive voltages.
To eventually single out V_iSSE from V_res (which is taken to include the cross coupling of V_d from here on out) individually the dependence on the current density I_d can be employed. Since the spin Seebeck voltage V_iSSE depends on the dissipated electrical power (the Joule heating) $P_\mathrm{Joule} = V_\mathrm{d} I_\mathrm{d} = I_\mathrm{d}^2 R$ where R is the sample resistance it is

proportional to the square of the driving current, while V_{res} is linear in I_{d}. To summarize, one expects

$$V_{\mathrm{iSSE}} \propto I_{\mathrm{d}}^2 \cos\varphi, \tag{5.41}$$
$$V_{\mathrm{res}} \propto I_{\mathrm{d}} \cos 2\varphi, \tag{5.42}$$

for a measurement in the transverse direction (i.e. $V_{\mathrm{t}} = V_{\mathrm{iSSE}} + V_{\mathrm{res}}$) and where it was assumed that V_{res} originates from the spin Hall magnetoresistance. Equations (5.41) and (5.42) show that the resistive contributions and the cross-coupling obey $V_{\mathrm{res}}(+I_{\mathrm{d}}) = -V_{\mathrm{res}}(-I_{\mathrm{d}})$ while the spin Seebeck voltage obeys $V_{\mathrm{iSSE}}(+I_{\mathrm{d}}) = +V_{\mathrm{iSSE}}(-I_{\mathrm{d}})$. V_{iSSE} can thus be obtained by adding $V_{\mathrm{iSSE}}(+I_{\mathrm{d}})$ to $V_{\mathrm{iSSE}}(-I_{\mathrm{d}})$ such that

For magnetic fields in the film plane the resistive voltages from an anomalous Hall effect in conducting magnets share the same symmetry with respect to I_{d}.

$$\begin{aligned} V_{\mathrm{t}}(+I_{\mathrm{d}}) + V_{\mathrm{t}}(-I_{\mathrm{d}}) &= V_{\mathrm{res}}(+I_{\mathrm{d}}) + V_{\mathrm{res}}(-I_{\mathrm{d}}) + \\ &\quad V_{\mathrm{iSSE}}(+I_{\mathrm{d}}) + V_{\mathrm{iSSE}}(-I_{\mathrm{d}}) \\ &= V_{\mathrm{res}}(+I_{\mathrm{d}}) - V_{\mathrm{res}}(+I_{\mathrm{d}}) + \\ &\quad V_{\mathrm{iSSE}}(+I_{\mathrm{d}}) + V_{\mathrm{iSSE}}(+I_{\mathrm{d}}) \\ &= 2V_{\mathrm{iSSE}}(+I_{\mathrm{d}}) \end{aligned} \tag{5.43}$$

and analogously

$$V_{\mathrm{t}}(+I_{\mathrm{d}}) - V_{\mathrm{t}}(-I_{\mathrm{d}}) = 2V_{\mathrm{res}}(+I_{\mathrm{d}}). \tag{5.44}$$

Eq. 5.41 and Eq. 5.42 are, strictly speaking, only first order approximations, since with increasing I_{d}, the sample's resistance $R = R(T)$ will also increase due to the induced temperature changes. The higher order terms, however, remain even (V_{iSSE}) and odd (V_{res}) powers of I_{d} even in the limit of significant current heating induced resistance modulation. As long as linear relations between resistance and temperature as well as temperature and dissipated power, i.e. $R(T) = R_0 + \delta R \cdot T$ and $T(P_{\mathrm{Joule}}) = T_0 + \delta T \cdot P_{\mathrm{Joule}}$ hold, then

$$\begin{aligned} V_{\mathrm{iSSE}} &\propto \frac{I_{\mathrm{d}}^2 (R_0 + T_0 \delta R)^2}{(1 - I_{\mathrm{d}}^2 \delta R \delta T)^2} \cos\varphi \\ &= \left[(R_0 + T_0 \delta R)^2 \sum_{n=1}^{\infty} n (\delta R \delta T)^{n-1} I_{\mathrm{d}}^{2n} \right] \cos\varphi, \end{aligned} \tag{5.45}$$

$$\begin{aligned} V_{\mathrm{res}} &\propto \frac{I_{\mathrm{d}} (R_0 + T_0 \delta R)}{1 - I_{\mathrm{d}}^2 \delta R \delta T} \cos 2\varphi \\ &= \left[(R_0 + T_0 \delta R) \sum_{n=1}^{\infty} (\delta R \delta T)^{n-1} I_{\mathrm{d}}^{2n-1} \right] \cos 2\varphi \end{aligned} \tag{5.46}$$

and Eq. (5.43) and Eq. (5.44) remain correct also in the limit of large I_{d}. The linear relation between resistance and temperature is a good approximation of the behavior of most metals such as Pt over fairly large temperature ranges, as is the linear relation between temperature and power in most solids. Equations (5.45) and (5.46) obviously break down when $I_{\mathrm{d}}^2 \delta R \delta T \geq 1$ which is satisfied for $I_{\mathrm{d}} \gtrsim 0.5\,\mathrm{A}$ in the

The Pt film will simply burn for currents well below this value.

structured thin film sample investigated here and thus far beyond any value one might sensibly apply in an experiment.

For an even larger signal-to-noise ratio an AC-current can be applied instead of the DC-current discussed in this chapter. Taking $I_\mathrm{d} = I_0 \sin \omega t$, with current magnitude I_0 and the modulation frequency ω in Eq. (5.41) and Eq. (5.42) it is found that $V_\mathrm{res} \propto \omega$ and $V_\mathrm{iSSE} \propto 2\omega$ to first order, which can be detected rather conveniently using a lock-in amplifier [183, 191]. For large driving currents some of the spin Seebeck (resistive) voltage will, however, be shifted into the higher order terms as evident from Eq. (5.45) [Eq. (5.46)]. Again this is only relevant for large driving currents but since the lock-in is sensitive to only a single summand in Eq. (5.45) [Eq. (5.46)] rather than their total this comes into effect a bit earlier when I_d is of the order of a few ten milliamperes.

It should be noted that current (on-chip) heating techniques have already been employed previously for spin Seebeck effect experiments [193, 194] but the detection mechanism in these cases is unlike the one discussed in this chapter. In much the same fashion as presented here, the different symmetries with respect to the driving current I_d are also used in some spin torque studies [195] to distinguish between Oersted field and spin torque induced magnetization manipulation.

5.3.2 *Experimental verification*

The sample used in this study is a Pt/YIG/GGG thin film heterostructure, grown via pulsed laser deposition and subsequent Pt evaporation as described in Ch. 3. The thickness of the YIG and Pt layers are 61 nm and 11 nm, respectively. As depicted in Fig. 5.11 the Pt and the YIG layers were patterned into a Hall bar mesa structure (central bar length 950 µm, width 80 µm) using optical lithography and argon ion beam milling. Afterwards the samples were mounted onto copper heat sinks.

The measurements in this chapter have all been performed in a low pressure environment ($p \lesssim 10\,\mathrm{mbar}$) in a cryostat with variable temperature insert. If not noted otherwise, the sample was stabilized at a base temperature of 250 K. While the controlled environment of a cryostat yields better signal to noise ratio and abates thermal drift, measurements under ambient conditions in an electromagnet at room temperature are equally possible. By comparing the measured voltages with a separately recorded ρ_Pt the Pt resistance can also be used for on-chip thermometry [196, 197].

The V_iSSE extraction procedure is visualized in Fig. 5.12 for a fixed angle $\varphi = 45°$ between the Hall bar and the external magnetic field (*cf.* Fig. 5.11). Here the transverse voltage is recorded as a function of

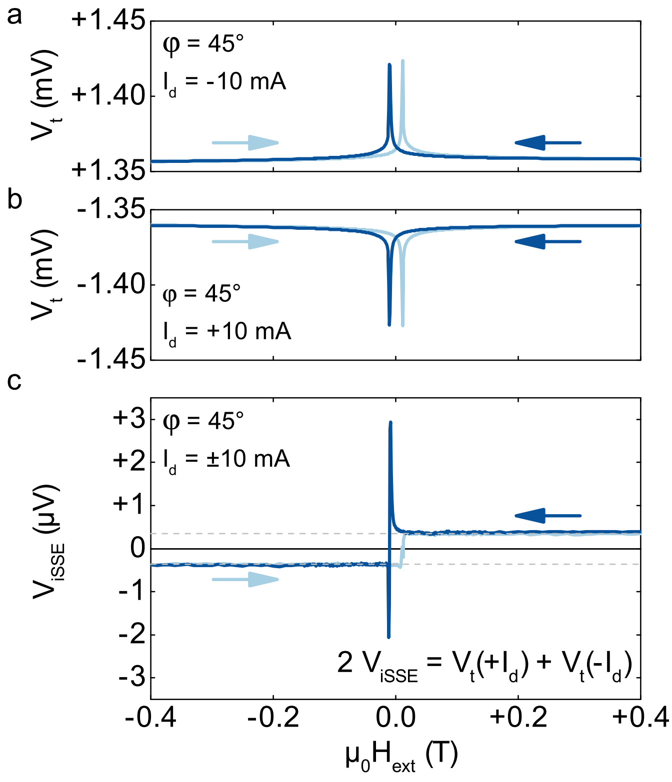

Figure 5.12.: Recorded transverse voltage as a function of the external magnetic field strength for $\varphi = 45°$. **a** For $I_\mathrm{d} < 0$ a positive offset voltage signal is recorded that exhibits the typical features of the spin Hall magnetoresistance. **b** Reversing the direction of I_d also inverts the observed voltage signal. **c** Adding $V_\mathrm{t}(+I_\mathrm{d})$ and $V_\mathrm{t}(-I_\mathrm{d})$ reveals the much smaller, thermal (spin Seebeck) component.

the external magnetic field magnitude, which is varied from $+0.4\,\mathrm{T}$ to $-0.4\,\mathrm{T}$ and back to $+0.4\,\mathrm{T}$. For a pure spin Seebeck signal one would expect the observed signal's shape to closely mimic that of the magnetic hysteresis loop of YIG, but apparently this is not the case. Clearly the signal shown in Fig. 5.12a is dominated by the transverse component of the in-plane spin Hall magnetoresistance [48], which changes sign upon changing the current direction (Fig. 5.12b). Upon adding the two curves, however, the hysteresis loop becomes visible (Fig. 5.12c). The large additional peaks close to the coercive fields are residues of V_res due to influence of the Oersted field generated by I_d. As evident from Eqs. (5.41) and (5.42) both V_iSSE and V_res depend on the angle φ between the external magnetic field and the current path through the sample. The analysis further assumes φ to be identical for $\pm I_\mathrm{d}$. The external magnetic field that determines φ, however, is superimposed by the Oersted field generated by I_d.

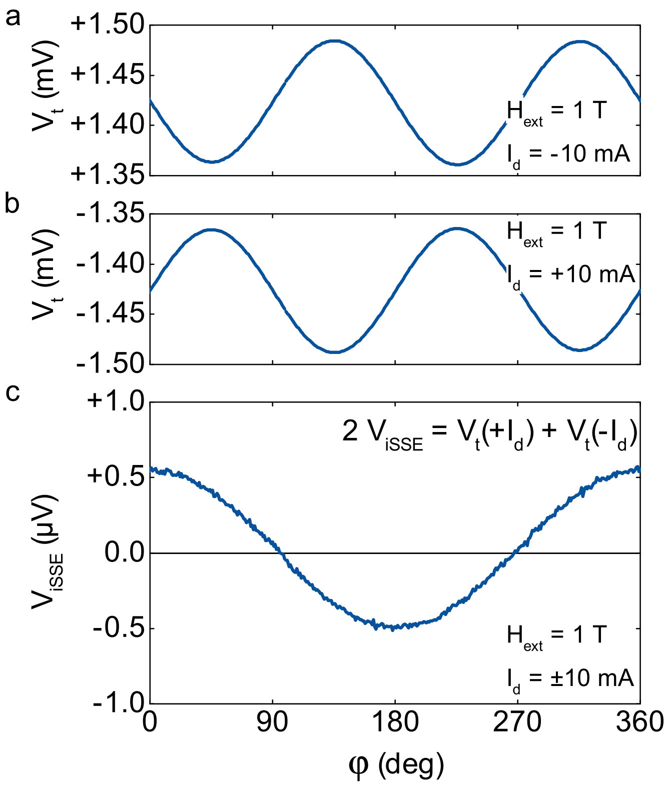

Figure 5.13.: Thermal voltage as a function of the external magnetic field direction φ. The magnitude of the external magnetic field remains fixed at 1 T throughout the entire measurement. **a** For $I_d < 0$ a positive offset voltage is recorded with the visible $\sin^2 \varphi$ variation stemming from the spin Hall magnetoresistance. **b** Inverting the current ($I_d > 0$) also reverses the voltage signal, but upon adding up $V_t(+I_d)$ and $V_t(-I_d)$ and dividing the result by two (**c**) a $\cos \varphi$ component remains, consistent with the spin Seebeck effect as predicted by Eq. (5.41).

When the external magnetic field becomes small enough that the Oersted field generated by I_d affects the total magnetic field the magnetic layer is exposed to appreciably then φ is a function of I_d as well. In that case adding the measured voltages for positive and negative driving currents will no longer entirely cancel out V_{res}. Since $V_{res} \gg V_{iSSE}$ even small changes in φ due to the polarity of I_d then become visible as residues of V_{res}. This topic is further expanded on in Refs. [183, 191].

To investigate the expected $\cos \varphi$ dependence of V_{iSSE} the applied magnetic field is kept at a fixed value of 1 T and the transverse voltage V_t is recorded while varying the field orientation with respect to the Hall bar. The field value of 1 T is chosen large enough to rule

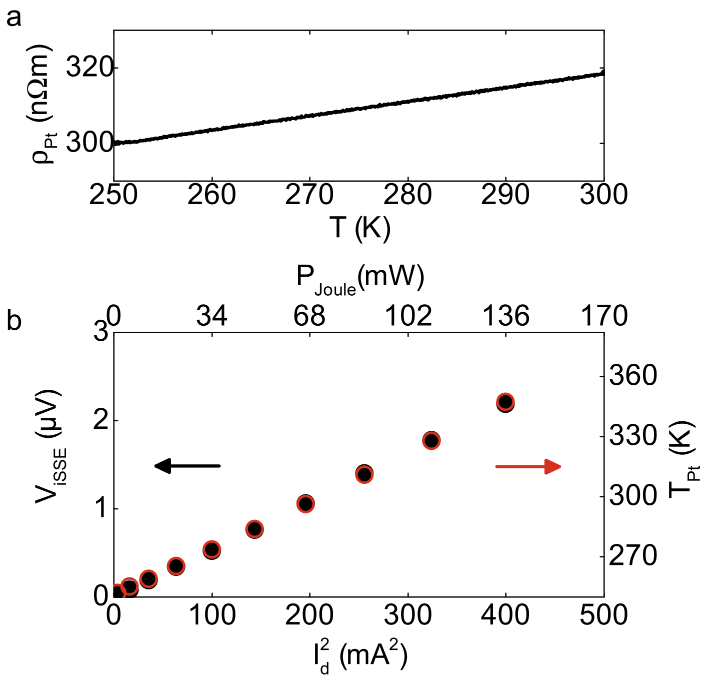

Figure 5.14.: **a** The resistivity of the Pt film of as a function of temperature. The slope is almost constant as expected for Pt [198]. **b** Thermal component (V_{iSSE}) of the recorded voltage (full symbols) and Pt temperature (open circles) as a function of the square of applied current. To obtain the individual $V_{iSSE}(I_d)$ data points the external magnetic field was rotated at a fixed field strength of 1 T, from which the spin Seebeck voltage is extracted [$V_{iSSE} \equiv V_{iSSE}(\varphi = 0°)$] for each value of the driving current $\pm I_d$. The observed V_{iSSE} scales quadratically with I_d as does T_{Pt}. Note that the T_{Pt} value for the two rightmost data points is an extrapolation.

out any remanent magnetic features of the YIG and ensure that its magnetization is truly parallel to the external magnetic field. As in Fig. 5.12a,b the measured signal in Fig. 5.13a,b is dominated by the spin Hall magnetoresistance, featuring its characteristic $\sin^2\varphi$ dependence, which reverses sign as the current direction is inverted. Once again, by adding the signals obtained for opposite current polarity the resistive effects cancel out and only the spin Seebeck component remains (Fig. 5.13c). As predicted by Eq. (5.41) the signal follows a $\cos\varphi$ dependence.

As a final check to confirm that the recorded signals indeed stem from a thermal effect this procedure is repeated as a function of the applied current. Figure 5.14b shows $V_{iSSE} = \frac{1}{2}[V_t(+I_d) + V_t(-I_d)]$ as a function of I_d^2. V_{iSSE} clearly shows a quadratic dependence on the applied current, supporting the notion of Eq. (5.41) that the measured spin Seebeck effect should scale quadratically with I_d. Moreover, the effect quickly drops below the noise floor for small currents for which the spin Hall magnetoresistance is still clearly visible in V_t. Furthermore, by simultaneously measuring the resistance of the Pt Hall bar along the current direction its temperature can also be inferred by comparing the measured resistance value to a $R(T)$ calibration curve recorded separately at a small current value depicted in Fig. 5.14a. As expected, the temperature increase of the Pt film is directly proportional to I_d^2 as well. In other words, V_iSSE is directly proportional to the temperature increase of the Pt film as suggested above.

5.3.3 *High field and variable temperature data*

With the measurements above performed in a cryostat it becomes possible to also investigate the spin Seebeck effect at large external magnetic fields and at low temperatures.

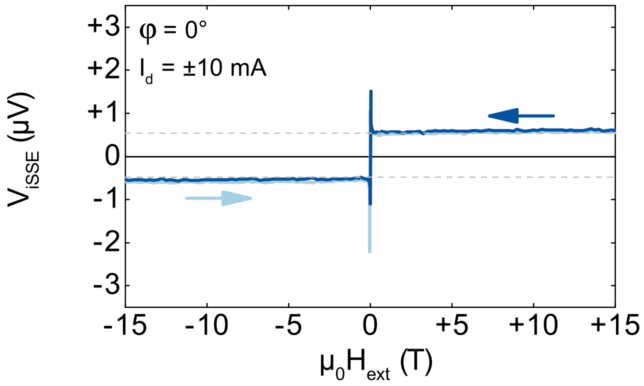

Figure 5.15.: Recorded spin Seebeck voltage as a function of the external magnetic field strength for $\varphi = 0°$. V_iSSE stays constant for fields of up to 15 T.

As mentioned in Ch. 5.1 and Ch. 5.2, Kikkawa *et al.* [120] showed that the spin Seebeck effect is attenuated at large magnetic fields. The attenuation, however, depends on the thickness of the magnetic layer with thicker films showing a stronger attenuation at a given magnetic field. Indeed, the data in Fig. 5.15 show that even at 15 T external magnetic field no attenuation can be observed in the 61 nm YIG film. 15 T are equivalent to an energy of about 1.7 meV ($\equiv$ 20 K). In light of the model put forward in Ch. 5.2 these values then represent the lower limit for the dominant magnon species in this sample. Considering that the dominant magnon energy in a comparably thin sample in Ch. 5.2 was found to be above 1 meV as well this result should be expected, although it is surprising to observe no

$E = k_\mathrm{B}T = \hbar\gamma B$

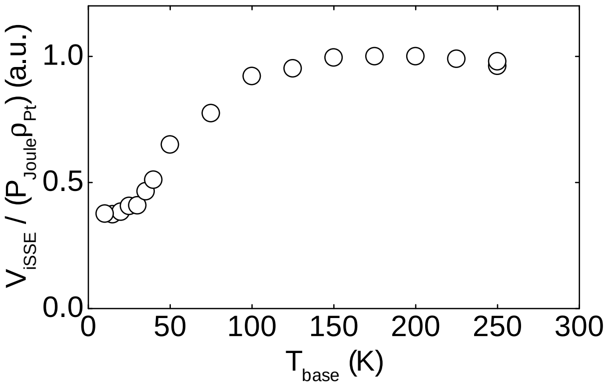

Figure 5.16.: Spin Seebeck voltage as a function of the cryostat base temperature. The values are normalized to the product of heating power and Pt resistivity to eliminate the temperature dependent influence of the electrical properties of the Pt layer on the results. The normalized voltage drops to about half its 250 K at low temperatures. The lowest temperature values are likely compromised by insufficient thermal coupling to the heat sink and hence do not accurately represent the sample (YIG) temperature.

attenuation at all in Fig. 5.15. On the other hand, the magnetization damping in these two samples might be rather different and the exact relation of the attenuation and the applied magnetic fields is not yet fully (in particular qualitatively) understood. It is possible that the attenuation has a rather abrupt onset that prevents detection below some critical thickness or field value.

Finally, Fig. 5.16 depicts the spin Seebeck voltage as a function of the cryostat base temperature, normalized by the heating power P_{Joule} and sample resistivity ρ_{Pt}, which largely eliminates the influence of the Pt layer properties on the measurement. Here, the normalized spin Seebeck signal stays approximately constant (or increases slightly) down to 150 K but drops to about half the room temperature level by 50 K. The saturation observed for $T_{\text{base}} \lesssim 40\,\text{K}$ is most likely an artifact of a discrepancy between sample and measured (cryostat) temperature, although the result does not change appreciably if the Pt temperature instead of the cryostat base temperature is taken for the analysis. Neglecting these few data points, however, the behavior is otherwise consistent with that reported in the literature [119, 120, 200] for thin films. In general, the decreased response of the spin Seebeck effect at low temperatures is commonly [12, 120, 200] explained by the diminishing number of magnons when $T \to 0\,\text{K}$. The interaction with the lattice can, however, significantly affect the low temperature response in thicker

This neglects potential changes in the spin transport parameters of Pt at low temperatures [199].

films [120].

5.3.4 *Summary*

The current heating induced spin Seebeck effect technique demonstrated in this chapter allows spin Seebeck effect measurements with a minimal set of lab equipment. In principle, an appropriate sample, a magnet and multimeter suitable for four point measurements are sufficient to implement the technique. While labs are typically more sophisticatedly equipped than the minimal example above, the simplicity of the approach also allows to integrate spin Seebeck measurements into a large variety of other setups. In particular, the possibility to perform temperature dependent measurements has proven [71] to be an invaluable tool in the study of compensated magnetic garnets. As a side benefit, the technique also cuts measurement time in that e.g. spin Hall magnetoresistance and spin Seebeck effect can be recorded simultaneously on the same device.

An issue in many spin Seebeck experiments is the precise determination of the temperature drop across the magnetic layer. By using the Pt layer as a resistive thermometer it is possible to infer the temperature on one end of the magnetic layer with much larger accuracy than in experiments where e.g. copper heaters are used. Although only the phonon temperature, rather than the magnon temperature, can be measured this way this quantity still represents a crucial parameter to infer the state of the magnetic system as demonstrated in Ch. 5.1. Determining the temperature on the other side of the magnet remains a challenge. However, Uchida *et al.* [70] presented measurements on a Pt/YIG(bulk)/Pt sample that allow to infer the temperature on both ends of the YIG film. For further quantitative studies it is thus desirable to fabricate also thin film samples this way. In particular, this would allow a far more robust extraction of the spin Seebeck voltage at very low temperatures.

5.4 SYNOPSIS

While the origin of the spin Seebeck effect is still not fully understood, in the course of this thesis a consistent picture has been developed. In particular the generation and spectral composition of the magnon accumulation at the interface between the magnet and the normal metal has been investigated intensively. In this context, the experiments presented in Ch. 5.1 and Ch. 5.2 constitute crucial results.

The analytical and numerical studies in Ch. 5.1 suggest that the magnon temperature in most of the magnet is close to that of the phonons, but that the coupling between magnons and electrons via the spin pumping process notably affects the magnon distribution at the interface. More precisely, the effective magnon temperature follows that of the electrons much more stringently than assumed previously. While the magnon-phonon coupling, by virtue of the modeling employed, is presently understood as a process that preserves the specific magnon distribution, it is intrinsically frequency-dependent and likely to distort the magnon distribution. It appears, however, that the distortion of the magnon spectrum is small and does not lead to significant deviations from a Bose-Einstein distribution. Adding a correction term to the standard thermal distribution may indeed be sufficient to describe the magnon system as a whole. In summary, the modeling is able to account for all coupling channels in the correlated phonon-electron-magnon-system and correctly reproduces a number of experimental results [118, 122]. Nevertheless, more efforts are necessary to make this approach a fully quantitative tool.

Although the distortion of the magnon spectrum is expected to be small, it appears reasonable to assume that these small deviations are, in fact, the most relevant for the spin currents measured in experiments. To this end the study of the transient properties of the magnon spectrum presented in Ch. 5.2 provides important insight into the composition of the magnons that spawn the spin current flow between the magnet and the normal metal. The dependence of their dynamic response on the thickness of the magnetic layer demonstrates that indeed the thermal state at the interface is more complicated and not fully described by the simplest diffusion models. Rather it is suggested that an energy resolved approach is necessary to correctly model the magnon transport in all details. In particular, the overrepresentation of low-energy magnons and the experimental determination of the magnon-phonon coupling of high energy magnons are crucial results.

With tools such as laser (Ch. 5.2) or direct current (Ch. 5.3) heating established, in parts, in this thesis an obvious next step is to extend the material system from almost exclusively yttrium iron garnet, to other magnetic insulators as well. This may either be compensated garnets on which experiments [71] uncovered quite unusual behavior, or, at low temperatures in particular much simpler materials such as europium oxide.

Additional methods such as time resolved Kerr [201] or Faraday [202] effect could also be employed to investigate the magnon spectra on timescales even shorter than accessible via laser heating. An alternative approach might also be nanostructuring of the samples, employing artificial lattices or Bragg reflectors to single out individual magnon bands. This would enable a much deeper understanding of how magnons interact with phonons and among themselves and may even be sufficient to quantitatively determine the role of different magnetic sublattices - both of which are necessary for a truly complete picture of the spin Seebeck effect.

Methods to increase the figure of merit have already been proposed [203].

At any rate, the poor figure of merit of spin-caloritronic devices and the poor controllability of thermal compared to e.g. electric transport suggests that the spin Seebeck effect should be employed foremost in cases where its broadband character of the excitation is an advantage. In certain materials some magnetization modes might be in- or poorly accessible by other means but of interest for applications or fundamental research. In terms of practical applications in the near future it is, however, likely that the spin Seebeck effect will mostly play the role of a spurious effect that needs to be considered when designing and characterizing devices.

6

SIGN CONVENTION FOR THE SPIN HALL ANGLE

In Ch. 2.2 the spin Hall effect [30–32, 53, 204–209] and the spin Hall angle θ_{SH} relating the magnitude of spin and charge currents to each another have been introduced. As evident from the subsequent chapters, the (inverse) spin Hall effect is quite often essential for spin current based phenomena. Since the sign of θ_{SH} determines the sign of the induced transverse voltage in experiments in which the inverse spin Hall effect is used to detect spin currents [53] such as for spin pumping [56, 58, 210–213] or the spin Seebeck effect [10, 16, 73, 80, 214], the interpretation of experimental data hinges on knowledge of the *absolute* sign of θ_{SH}.

In practice, however, the only convention with respect to the sign of θ_{SH} had been to assume a positive value for Pt and thus a negative value for e.g. Mo [56], Ta [215], and W [216]. The lack of a proper definition for $\operatorname{sgn}\theta_{\mathrm{SH}}$ challenges scientists and authors to needless additional care when conducting and interpreting experiments. The issue is further amplified by a lack of care in manuscripts, missing or glossing over the sign of other crucial parameters such as spin and charge currents, magnetic field direction or simply measurement device polarity which are all required to infer $\operatorname{sgn}\theta_{\mathrm{SH}}$.

To address this issue a collaboration between research groups from the Institute for Materials Research, Tohoku University (IMR), Technische Universität Kaiserslautern (UniKL), Zernike Institute for Advanced Materials, University of Groningen (RUG), and the Walther-Meißner-Institut in Garching (WMI) was formed to establish a solid definition of the sign of θ_{SH}. To this end, a theoretical toy model is formulated and compared with experiment. The results have been published in J. Phys. D: Appl. Phys. 48, 025001 (2015) (Ref. [17]) from which this chapter bountifully borrows text and figures.

6.1 THE MODEL DEFINITION

A practical definition of $\operatorname{sgn}\theta_{\mathrm{SH}}$ has to be applicable to both theory and experiment. To satisfy the former requirement and give actual physical meaning to the definition a toy model is developed in the following that relates $\operatorname{sgn}\theta_{\mathrm{SH}}$ to electron scattering at charged impurities. While the toy model phenomenologically describes the extrin-

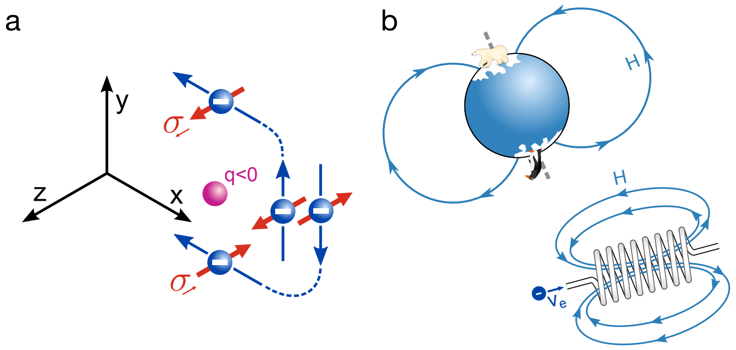

Figure 6.1.: **a** The transverse deflection of polarized electrons generated by a fixed point charge $q < 0$ is associated with a positive spin Hall angle. In the coordinate system employed here, electrons polarized along $+\boldsymbol{z}$ and moving in the $+\boldsymbol{y}$ direction are deflected in the $-\boldsymbol{x}$ direction. This corresponds to a conventional current in the $+\boldsymbol{x}$ direction. **b** A magnetic field is positive when aligned with the Earth's magnetic field or as the magnetic field generated by a negatively charged particle current flowing through a coil when configured as sketched.

sic contribution to the spin Hall effect it is too crude to describe real materials.

As introduced in Ch. 2 angular momentum is related to magnetic moment by the relation $\boldsymbol{\mu}_l = \boldsymbol{l}q/(2m)$ [217]. This magnetic moment direction is also generated by two monopoles on the $\mathbf{l}$-axis, the negative (south pole) just below and the positive (north) pole just above the origin. The magnetic moment of the Earth points to the south, so the geographic north pole is actually the magnetic south pole. Hence, the geomagnetic fields on the surface of the Earth as measured by a compass needle point to the north pole. For non-relativistic electrons [218] whose charge is generally taken to be negative, i.e. $q = -e < 0$, with spin $\mathbf{s} = \frac{\hbar}{2}\boldsymbol{\sigma}$ the corresponding magnetic moment $\boldsymbol{\mu}_s = -\boldsymbol{s}ge/(2m) = -\gamma\boldsymbol{s}$. In solids, the Landé-$g$-factor g depends on both $\boldsymbol{s}$ and $\boldsymbol{l}$ and may take either sign. In most cases, however, g and therefore γ are positive.

Chapter 2.1 introduced spin currents $\boldsymbol{j}_\mathrm{s}$ as the (linear) response to a force given by the spatial derivative of the spin chemical potential. The direction of $\boldsymbol{j}_\mathrm{s}$ therefore represents the flow direction of the angular momentum (spin) current. The mathematical treatment of spin currents often further requires knowledge of the polarization direction $\boldsymbol{\sigma}_{j_\mathrm{s}}$ as demonstrated e.g. in Ch. 2.2. Both quantities can be combined to form the spin current tensor $\overleftrightarrow{\boldsymbol{J}_\mathrm{s}}$ consisting of column vectors $\mathbf{J}_\mathrm{s}^{\alpha}$ that represent the polarization of (spin) angular momentum currents in the Cartesian α-direction and the row vectors $\mathbf{J}_{\mathrm{s},\beta}$

represent the flow direction of angular momentum along β. $\mathbf{J}_{\mathrm{s},\beta}$ is identical to a $\boldsymbol{j}_{\mathrm{s}}$ when $\boldsymbol{\sigma}_{j_{\mathrm{s}}} = \boldsymbol{\beta}$, except for dimensionality, as $\mathbf{J}_{\mathrm{s},\beta}$ and correspondingly $\boldsymbol{J}_{\mathrm{c}}$ are both defined as particle flow (units s^{-1}) here to avoid ambiguity. In this notation the spin Hall angle is the proportionality factor in the phenomenological relations

$$\mathbf{J}_{\mathrm{s},\beta} = \theta_{\mathrm{SH}} \quad \boldsymbol{\beta} \wedge \mathbf{J}_{\mathrm{c}} \tag{6.1}$$

$$\mathbf{J}_{\mathrm{c}} = \theta_{\mathrm{SH}} \sum_{\alpha} \mathbf{J}_{\mathrm{s}}^{\alpha} \wedge \boldsymbol{\alpha} \tag{6.2}$$

where the $\boldsymbol{\alpha}, \boldsymbol{\beta} \in \{\mathbf{x}, \mathbf{y}, \mathbf{z}\}$ are Cartesian unit vectors.

The physical significance of $\operatorname{sgn} \theta_{\mathrm{SH}}$ is demonstrated in the following. For an external point charge q at the origin in the weakly relativistic electron gas the bare Coulomb potential at distance r is

$$\phi_0(r) = \frac{1}{4\pi\epsilon_0} \frac{q}{r}, \tag{6.3}$$

where ϵ_0 is the vacuum permittivity. In metals $\phi_0(r)$ is screened by the mobile charge carriers to become the Yukawa potential $\phi = \phi_0 e^{-r/\lambda}$. The screening length λ serves to regularize the expectation values, but drops out of the final results. The spin-orbit interaction of an electron in the potential ϕ can be expressed in terms of an effective magnetic field [219]

$$\mathbf{B}_{\mathrm{so}} = \frac{-e}{2m^2c^2\gamma} \left(\boldsymbol{\nabla}\phi \wedge \mathbf{p} \right), \tag{6.4}$$

where c is the velocity of light. The force on the electron then reads

$$\mathbf{F}_{\mathrm{so}} = -\boldsymbol{\nabla}(-\boldsymbol{\mu}_{\mathrm{s}} \cdot \mathbf{B}_{\mathrm{so}}) = \frac{e\hbar}{4m^2c^2} \boldsymbol{\nabla} \left[\sigma \cdot (\boldsymbol{\nabla}\phi \wedge \mathbf{p}) \right]. \tag{6.5}$$

Focussing on a free electron moving in the y-direction ($\boldsymbol{p} = p_y \boldsymbol{y}$) with its spin pointing in the z-direction ($\boldsymbol{\sigma} = \mathbf{z}\sigma_z$) in an ensemble of randomly distributed identical point charges with density n, the expectation value $\langle \sigma_z \rangle = 1$ and the average force is

$$\langle \mathbf{F}_{\mathrm{so}}^{yz} \rangle = \frac{n}{4\pi\epsilon_0} \frac{4eq\hbar\pi^2}{3m^2c^2} p_y \mathbf{x}. \tag{6.6}$$

To define the positive spin Hall angle the charge is now chosen to be negative ($q < 0$, repulsive). This then yields the following right-hand rule: The electron with its spin pointing in the z-direction (thumb) and moving in the y-direction (forefinger) drifts to the negative x-direction (middle finger) [Fig. 6.1a]. A comparison with Eq. (6.1) and using

$$\boldsymbol{J}_{\mathrm{s},z} = -\frac{C}{e^2\rho} \nabla \mu_{\mathrm{s}} = \frac{C}{e^2\rho} \langle \mathbf{F}_{\mathrm{so}}^{yz} \rangle \tag{6.7}$$

and

$$\boldsymbol{J}_{\mathrm{c}} = \frac{p_y}{m} n_{\mathrm{e}} C \mathbf{y} \tag{6.8}$$

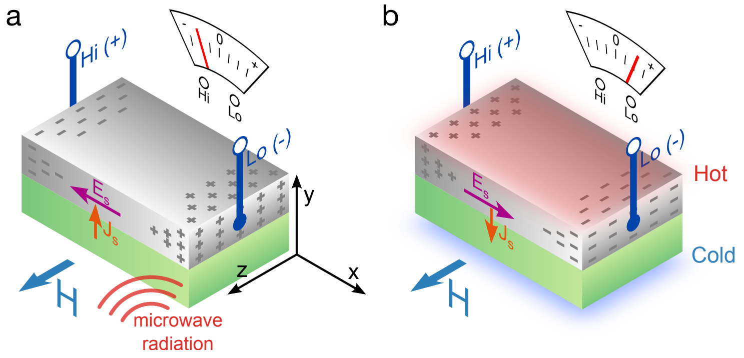

Figure 6.2.: **a** Typical setups for spin pumping experiments. An rf-microwave field excites magnetization precession that relaxes by emitting a spin current into the adjacent Pt layer. **b** In spin Seebeck experiments the spin current from the YIG to the Pt is negative when the latter is hotter. In both cases, the inverse spin Hall effect leads to a voltage between the contacts *Hi* and *Lo*.

where μ_s is the spin chemical potential, ρ is the resistivity, C is the cross sectional area the currents are flowing through, and n_e is the carrier density, leads to a spin Hall angle

$$\theta_{SH} = -\frac{n}{4\pi\epsilon_0}\frac{4eq\hbar\pi^2}{3m^2c^2}\frac{m}{e^2\rho n_e}. \tag{6.9}$$

Inserting numbers for fundamental constants yields $\theta_{SH} \cong \pm 3 \times 10^{-10}\,\Omega\mathrm{m} \times n/(n_e\rho)$ for $q = \mp e$.

For the experimentalist a more hands-on formulation of the above is, however, more appropriate. The time-averaged spin current injected by a steady precession around the equilibrium magnetization with unit vector **m** is polarized along **m**. This spin pumping process [9] is associated with energy relaxation of the magnetization dynamics that increases the magnetic moment in the direction of the effective magnetic field. When the g-factor is positive, the spin pumping current through the interface is positive as well. *Positive* hereby refers to the emission of a spin current polarized along $\boldsymbol{m}$ by the magnet. In the spin Seebeck effect, when the temperature of the magnetization is *lower* than that of the electrons in the metal, the energy imbalance and, if $g > 0$, the spin current are opposite to that under ferromagnetic resonance [12], leading to an opposite sign in the inverse spin Hall effect voltage compared to the ferromagnetic resonance. Under open circuit conditions the inverse spin Hall effect [Eq. (6.2)] leads to a charge separation and an electrostatic field

$$\boldsymbol{E}_s = \frac{-e\rho}{A}\theta_{SH}\left[\boldsymbol{J}_{s,\boldsymbol{m}} \wedge \boldsymbol{m}\right], \tag{6.10}$$

where A is the area of the normal metal/magnet interface and ρ is the resistivity of the metal layer. This corresponds to an electromotive

university	t_{GGG}	t_{YIG}	t_{Pt}	l	w
Garching	500 µm	160 nm	7 nm	3 mm	1 mm
Kaiserslautern	500 µm	4.1 µm	10 nm	4 mm	1 mm
Sendai	500 µm	4 µm	10 nm	6 mm	1 mm
Groningen	500 µm	200 nm	6 nm	600 µm	30 µm

Table 6.1.: Substrate (t_{GGG}), magnet (t_{YIG}), and normal metal (t_{Pt}) layer thicknesses as well as sample length l and width w for the specimen employed in the study.

force $\mathcal{E} = -\boldsymbol{E}_{\mathrm{s}} \cdot \boldsymbol{l}$, where $\boldsymbol{l}$ is the length vector from the *Lo* to the *Hi* contact in Fig. 6.2a,b. This figure sketches typical experimental setups for spin pumping [Fig. 6.2a] and spin Seebeck experiments [Fig. 6.2b] on yttrium iron garnet/platinum thin film (YIG/Pt) bilayers. In the former, a normal metal/magnet stack is exposed to microwave radiation with frequency f (typically in the GHz regime), while in spin Seebeck experiments the bilayer is exposed to a thermal gradient as demonstrated in Ch. 5. The direction or sign of the applied magnetic field is related to the current direction according to Ampere's right hand law as depicted in Fig. 6.1b. In practice, it is convenient to use a compass needle for comparison with the Earth's magnetic field. Fig. 6.1b defines the positive field direction from the antarctic to the arctic, i.e. along the geomagnetic field introduced above.

6.2 EXPERIMENTAL VALIDATION

To validate that the definitions derived in the previous section are indeed consistent with the de facto standard of a positive spin Hall angle in platinum spin pumping and spin Seebeck experiments were performed by the participating experimental groups. The study was performed using differently fabricated YIG/Pt samples for details on which the reader is referred to Ch. 3 (WMI), Ref. [213] (RUG), Refs. [220, 221] (UniKL) and Ref. [222] (IMR) and Tab. 6.1.

Fig. 6.3 summarizes the results of the participating groups. Note that in each group both the spin pumping and spin Seebeck experiments were performed on the same sample, without changing the setup in measurement configurations equivalent to those depicted in Fig. 6.2.

At the WMI, spin pumping experiments (first row) were carried out in a microwave cavity with fixed frequency $f_{\mathrm{res}} = 9.82\,\mathrm{GHz}$ as a function of an applied magnetic field H_{ext} leading to resonance at $\mu_0 H_{\mathrm{ext}} \cong 270\,\mathrm{mT}$. The current heating induced spin Seebeck technique presented in Ch. 5.3 is used to generate a temperature gradient (hot Pt, cold YIG) [16]. The inverse spin Hall effect voltages for both

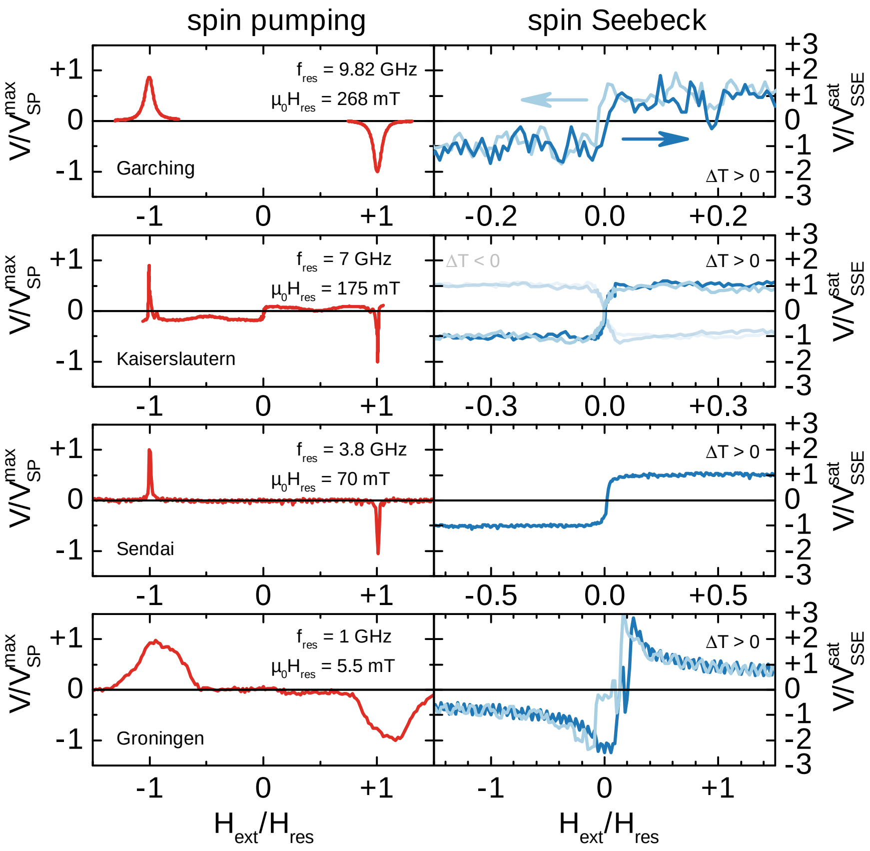

Figure 6.3.: Measured voltage signals for the FMR spin pumping (left) and spin Seebeck (right) experiments obtained by the contributing groups. The voltage signals have been normalized to a maximum modulus of unity while the applied magnetic fields are in units of the FMR resonance field H_{res} given in the insets. The temperature difference $\Delta T = T_{Pt} - T_{YIG}$ is positive. Sample parameters are given in Tab. 6.1.

spin pumping and the spin Seebeck experiments were measured by the same, identically connected nanovoltmeter with microwave and heating current separately turned on.

Results from the UniKL are shown in the second row in Fig. 6.3. A microwave with $f_{res} = 7\,\text{GHz}$ fed into a Cu stripline on top of the Pt film excites the FMR at an external magnetic field of $\mu_0 H_{ext} \cong 175\,\text{mT}$. The microwave current amplitude was modulated at a frequency of $f_{mod} = 500\,\text{Hz}$ to allow for lock-in detection of the induced voltages [221]. The spin pumping data show a small offset between positive and negative magnetic fields, which stems from Joule heating in the Pt layer by the microwaves. Peltier elements on the top and bottom (separated by an AlN layer) generated a thermal gradient for the spin Seebeck experiments that were reversed for cross checks, as shown in the right graph.

The third row in Fig. 6.3 shows the results obtained at the IMR. Here, the sample is placed on a coplanar waveguide such that at $f_{\text{res}} = 3.8\,\text{GHz}$ ferromagnetic resonance condition is fulfilled for $\mu_0 H_{\text{ext}} \cong 70\,\text{mT}$. The thermal gradient for the spin Seebeck measurements was generated by an electrically isolated separate heater on top of the Pt.

The fourth row in Fig. 6.3 shows the RUG results. A coplanar waveguide on top of the YIG was used to excite the ferromagnetic resonance at a magnetic field of $\mu_0 H_{\text{ext}} \cong 6\,\text{mT}$. The spin Seebeck effect was detected using the AC-variant of the current heating induced spin Seebeck scheme introduced in Ch. 5.3.1.

In spite of differences in samples and measurement techniques, all experiments agree on the sign for spin pumping and spin Seebeck effect. All experiments measure *negative* spin pumping and *positive* spin Seebeck voltages for positive applied magnetic fields that all change sign when the magnetic field is reversed, consistent with the theoretical expectations [9, 12, 30, 31].

These results now allow to infer the *absolute* sign of the spin Hall angle. With external magnetic field $\boldsymbol{H}_{\text{ext}}$ pointing in the $\boldsymbol{z}$ direction $\boldsymbol{m} \parallel \boldsymbol{z}$ and $\boldsymbol{J}_{\text{s}} \parallel \boldsymbol{y}$ for FMR spin pumping. According to Eq. (6.1), when $\theta_{\text{SH}} > 0$ $\boldsymbol{E}_{\text{s}} \parallel -\mathbf{x}$, which leads to a negative (positive) charge accumulation at the $-x$ $(+x)$ edge of the Pt film and a negative spin pumping voltage is expected as well as observed. In the spin Seebeck experiments with Pt hotter than YIG, the spin current flows in the opposite direction ($\boldsymbol{J}_{\text{s}} \parallel -\boldsymbol{y}$), and the voltage is inverted. Therefore, the spin Hall angle of Pt is positive if defined as above. The nature of the spin Hall effect in Pt is likely to be governed by its electronic band structure [223], but it should be a helpful to know that the sign is identical to that caused by negatively charged impurities.

The operator $\parallel$ is meant to signify that the quantities to its left and right are parallel and *their dot product is positive.*

6.3 SUMMARY

This chapter presented spin pumping and spin Seebeck experiments for various samples and experimental conditions leading to gratifying agreement of the results obtained by different groups. By carefully accounting for the signs of all experimental parameters and definitions relative and absolute signs of both effects could be determined. The positive spin Hall angle of Pt was linked to a simple physical model of negatively charged scattering centers, e.g. dopants, impurities or defects. The relative signs of spin pumping and spin Seebeck effect are consistent with theoretical predictions [12, 62, 64, 210]. The techniques and samples used in this chapter are representative for a large number of spin pumping and spin Seebeck experiments and may serve as a reference for other materials or sample geometries. With similar figures in the literature often incomplete or wrong, Fig. 6.2 in particular has proven a handy helper for quick validation of measurement results.

7

SPIN ORBIT TORQUE DRIVEN FERROMAGNETIC RESONANCE

The previous chapters demonstrated that spin transfer torques enable a convenient interfacing between collective spin excitations in a magnet and the conduction electrons' spin in a normal metal. Via the spin Hall effect this also affects the electric transport in the normal metal. All effects discussed so far covered the spin transfer torque mediated conversion of the spin excitations in the magnet into a measurable (voltage) signal in an adjacent normal metal. However, the generation of the spin excitations was left to other means, e.g. magnetic fields generated by external coils, heating of the sample or exposition to microwave radiation.

On the other hand, Ch. 2.3 already established that the spin transfer between magnets and normal metals is realized by the manipulation of the magnetization through a torque, i.e. a change of the magnetization vector $\boldsymbol{M}$. This implies that the flow of a spin current from a magnet into a normal metal (or the other way around) has to be reflected in a change of the magnetization state in the magnet. A change of the projection of $\boldsymbol{M}$ on the quantization axis thereby is equivalent to the creation or destruction of spin excitations polarized along the same. Other than the heat transfer examined in Ch. 5.1, the changes in $\boldsymbol{M}$ were small and could be neglected without impacting the final outcome of the experiments. However, in some configurations the impact of the spin transfer torque on $\boldsymbol{M}$, or its unit vector $\boldsymbol{m} = \boldsymbol{M}/|\boldsymbol{M}|$ is crucial for the experiment. When the Slonczewski-like torque described in Eq. (2.8) is taken into account in the Landau-Lifshitz-Gilbert equation [Eq. (2.9)] the Landau-Lifshitz-Gilbert-Slonczewski equation[1] [40]

$$\dot{\boldsymbol{m}} = -\gamma\mu_0(\boldsymbol{m} \wedge \boldsymbol{H}_{\text{eff}}) + \alpha\, \boldsymbol{m} \wedge \dot{\boldsymbol{m}} - \frac{\gamma\mu_{\text{s}}\, \text{Re}\left(g^{\uparrow\downarrow}\right)}{2M_{\text{s}}d_{\text{F}}} \boldsymbol{m} \wedge (\boldsymbol{m} \wedge \boldsymbol{\sigma}_{\mu_{\text{s}}}), \quad (7.1)$$

is obtained. Here, d_{F} is the thickness of the magnetic layer and μ_{s} is the amplitude of spin accumulation (i.e. proportional to the number of spin excitations) in the normal metal at the interface with the magnet. The spin transfer torque induced changes in $\boldsymbol{m}$ can also

See also Ch. 2.1.

---

[1] For a comparison of units recall that $[\gamma] = 1/\text{Ts}$, $[\mu_{\text{s}}] = \text{J}$, $[g^{\uparrow\downarrow}] = 1/\text{m}^2$, $[M_{\text{s}}] = \text{A/m}$ and $[d_{\text{F}}] = \text{m}$, totaling a unit of s^{-1} for the spin transfer torque term.

be parametrized in terms of an effective magnetic field generated by the spin accumulation μ_s in the $\boldsymbol{\sigma}_{\mu_\mathrm{s}}$-direction. The $\boldsymbol{m} \wedge \boldsymbol{H}_\mathrm{eff}$ and $\boldsymbol{m} \wedge \boldsymbol{\sigma}_{\mu_\mathrm{s}}$ terms in Eq. (7.1) are thus equivalent in terms of symmetry and the $\boldsymbol{m} \wedge (\boldsymbol{m} \wedge \boldsymbol{\sigma}_{\mu_\mathrm{s}})$ term may also be written as $\boldsymbol{m} \wedge \dot{\boldsymbol{m}}$ (since $\boldsymbol{m} \wedge \boldsymbol{H}_\mathrm{eff} \propto \dot{\boldsymbol{m}}$). In other words, accounting for the spin transfer torque adds an additional magnetization (anti-)damping term to the description of the magnetization dynamics. For this reason the Slonczewski-like torque is also often referred to as *damping-like torque* (*cf.* Ch. 2.4). Generating a spin accumulation μ_s in the normal metal thereby affects the transient properties of the magnetization and e.g. allows to tune the linewidth in ferromagnetic resonance experiments. When the Slonczewski-like torque is understood as a time-varying effective magnetic field instead, it is straight forward to understand that the modulation of this field at the resonance frequency of $\boldsymbol{m}$ can be used to directly excite magnetization dynamics. For static spin currents one generally considers the damping like character of the spin transfer torque, which can also be used to stimulate magnetization dynamics by overcompensation of the Gilbert damping [224].

The above makes the spin transfer torque attractive for spintronics applications, such as torque-induced magnetization control in nanodevices [215, 216, 225], for sensing, data storage, interconnects, and logics. Realization of these proposals, however, has mostly been limited to metallic magnets [226–230], while magnetic insulators received much less attention [160, 224, 231]. As highlighted in this thesis (e.g Ch. 3), however, yttrium iron garnet in particular offers many intriguing properties for spin (magnon) current based applications.

This chapter deals with the resonant excitation and detection of spin orbit torque induced magnetization dynamics in yttrium iron garnet. Chapter 7.1 details the proof of the excitation and detection of the fundamental (uniform precession) resonance mode via the spin transfer torque in a magnetic insulator. Ch. 7.2 expands these fundamental results and covers the excitation of higher order perpendicular standing spin wave mode.

7.1 EXCITATION OF THE UNIFORM PRECESSION MODE

Magnetization dynamics are typically investigated by application of an external, macroscopic and oscillating electromagnetic field to the magnet. Since keeping magnetic fields fully local is rather challenging on the nanometer-scale, conventional strategies to generate magnetic fields may be considered rather clumsy. An alternative, more elegant approach is to employ an oscillating spin transfer torque to induce the magnetization dynamics [232]. The latter is restricted to the (arbitrarily small) interface area between magnet and normal metal by nature of the spin transfer torque. To this end, a microwave-frequency (GHz) charge current is applied to the Pt layer of a YIG/Pt sample, which drives ferromagnetic resonance by the combined action of Oersted fields and spin transfer torque. The ensuing magnetization dynamics in turn generates a DC voltage, which can be accounted for by considering electrically detected DC spin pumping [9] (Ch. 2.4) and rectification mediated by the AC spin Hall magnetoresistance (SMR) [11, 233] (Ch. 2.3). Since the action of Oersted fields and spin transfer torques on spin pumping and spin Hall magnetoresistance rectification are intertwined in a nontrivial fashion, a comparison of samples with different YIG film thicknesses enables to discern and quantify the magnetization dynamics driven by the two aforementioned excitation processes and single out the spin transfer torque contribution of interest here. The experimental data can be modeled quantitatively using spin diffusion theory and quantum mechanical interface boundary conditions [234, 235]. The analysis shows that in very thin YIG films, magnetization dynamics indeed is driven by spin transfer torque. In the thinnest investigated YIG film the latter are, in fact, substantially more efficient than the Oersted fields at actuating magnetization dynamics.

This chapter adopts the results published in Phys. Rev. B 92, 144411 (2015) (Ref. [18]) and shares much of the same text and figures.

7.1.1 *Theoretical concepts*

In conventional magnetic resonance studies with coplanar waveguides the Oersted field B_{ac} generated by a high-frequency current is the exclusive generator of the magnetization precession in a nearby magnet. In contrast, the high-frequency current in the experiments discussed in this chapter is fed directly to the Pt layer of a YIG/Pt sample, as depicted in Fig. 7.1, and enables another excitation mechanism. The conventional high-frequency (Oersted) magnetic field generated by the charge current can be calculated as $B_{\mathrm{Oe}} = j_{\mathrm{c}} d_{\mathrm{N}} \mu_0 / 2$, where j_{c} is the charge current density, d_{N} is the thickness of the Pt film, and μ_0 is the vacuum permeability. The derivation of B_{Oe} assumes a placement on the surface of a laterally infinitely extended

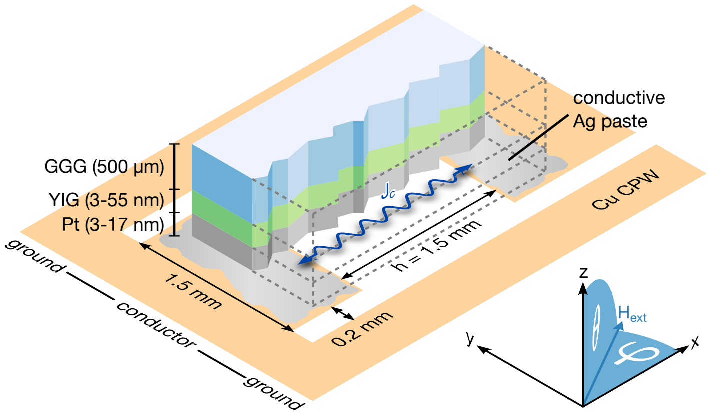

Figure 7.1.: Samples are placed across a gap in the center conductor of a coplanar waveguide and contacted with conductive Ag paste.

film and notably neglects any variation of B_{Oe} as function of the distance to surface, i.e. throughout the thickness of the magnet. As demonstrated in Ch. 7.2, however, the deviations from the actual field values are insignificant for the geometry and sample size employed here. Owing to the spin Hall effect [30, 31] a charge current in Pt is, however, accompanied by a transverse spin current (Ch. 2.2). At the magnetic insulator/normal metal interface, this spin current exerts an oscillating spin transfer torque on the magnetization [47] that can drive a magnetization precession as discussed above. An effective magnetic field, localized at the interface between the magnet and the normal metal, can be employed to parametrize the (anti-)damping torque [234] that varies with the angle between spin accumulation and magnetization. Its maximum value is $B_{\mathrm{STT}} = \theta_{\mathrm{SH}} j_{\mathrm{c}} \hbar / (2eM_{\mathrm{s}} d_{\mathrm{F}})\eta$, where θ_{SH} is the spin Hall angle, d_{F} is the thickness of the YIG film and M_{s} is its saturation magnetization. Furthermore, $\eta = 2\lambda\rho\,\mathrm{Re}(G^{\uparrow\downarrow})\tanh\frac{d_{\mathrm{N}}}{2\lambda} / [1 + 2\lambda\rho\,\mathrm{Re}(G^{\uparrow\downarrow})\coth\frac{d_{\mathrm{N}}}{\lambda}]$ describes the spin absorption efficiency [28] with the spin diffusion length λ, electrical resistivity ρ in the normal metal and the spin mixing interface conductance $G^{\uparrow\downarrow}$ (in units of $\Omega^{-1}\mathrm{m}^{-2}$. Note that $g^{\uparrow\downarrow}$ is in units of m^{-2}, i.e. $G^{\uparrow\downarrow} = g^{\uparrow\downarrow} \cdot 2\pi e^2/\hbar$).

Conversely, when magnetization dynamics in the magnet is excited, the normal metal provides an additional magnetization damping channel via spin pumping as described in Ch. 2.4. The inverse spin Hall effect makes detection of this spin current generated by spin pumping possible in terms of a DC inverse spin Hall voltage V_{SP} [57]. V_{SP} is a measure of the power absorbed by the magnetic system and therefore yields a purely symmetric resonance line shape [57], irrespective of the origin of the magnetization precession [236].

The spin transfer torque in addition also couples the magnetization orientation of the magnet to the electrical resistivity of the normal metal via the spin Hall magnetoresistance introduced in Ch. 2.3. Owing to spin Hall magnetoresistance the resistivity of the Pt film is modulated by $\Delta\rho_1 = \rho\theta_{\mathrm{SH}}^2(\lambda/d_{\mathrm{N}})\eta \tanh\frac{d_{\mathrm{N}}}{2\lambda}$ as a function of the magnetization orientation in YIG. In magnetic resonance, the high-frequency precession of the magnetization induces a high-frequency oscillation of ρ at the same frequency f_{mw} as j_{c}, which generates a DC rectification voltage [237] (V_{SMR}). In contrast to the symmetric line shape of V_{SP}, V_{SMR} also depends on the specifics of the phase relation between microwave current and magnetization precession [236], such that both symmetric and antisymmetric resonance line shapes are possible. For spin torque actuated magnetization dynamics the rectification voltage (i.e. the part of V_{SMR} depending on B_{STT}) resonance line shape is purely symmetric [234], while for Oersted field induced dynamics it is, in general, at least partially antisymmetric. Oersted fields, however, are affected by the local sample configuration. This may introduce a (DC magnetic field independent) phase offset δ between j_{c} and ρ which can render also the Oersted field induced V_{SMR} largely symmetric [233, 236, 238]. Therefore, a line shape analysis of the DC voltage detected in magnetic resonance in terms of symmetric and antisymmetric contributions alone does neither allow to distinguish the individual contributions from spin pumping and spin Hall magnetoresistance rectification, nor whether the dynamics stem from Oersted fields or the spin transfer torque. In particular, the variation of V_{SP} and V_{SMR} with the orientation of $\boldsymbol{B}_{\mathrm{ext}}$ can not be employed to distinguish between Oersted field and spin transfer torque actuated dynamics as is commonly done for anisotropic magnetoresistance based rectification [236]. Thus, in order to assess the importance of the spin torque actuated dynamics, a more careful and elaborate, quantitative analysis has to be performed. The corresponding expressions for V_{SP} and V_{SMR} are discussed below. As a general guideline, however, the spin transfer torque manifests itself as an increasingly symmetric resonance line shape of $V_{\mathrm{DC}} = V_{\mathrm{SP}} + V_{\mathrm{SMR}}$ for decreasing thickness of the magnetic layer (since $B_{\mathrm{STT}} \propto 1/d_{\mathrm{F}}$). The spin torque induced spin Hall magnetoresistance rectification resonance voltage peak is of opposite polarity compared to that origination from spin pumping.

The mathematical modeling of the AC-DC conversion mechanism is discussed in detail in Refs. [234, 235]. Converting notation to SI units, the DC spin pumping and rectification voltage read:

$$V_{\mathrm{SP}} = S_{\mathrm{SP}} \frac{\Delta B^2}{(B_{\mathrm{ext}} - B_{\mathrm{res}})^2 + \Delta B^2} \cos\varphi \sin 2\varphi, \tag{7.2}$$

$$\begin{aligned} V_{\mathrm{SMR}} = \Bigg[\quad & S_{\mathrm{SMR}} \frac{\Delta B^2}{(B_{\mathrm{ext}} - B_{\mathrm{res}})^2 + \Delta B^2} \\ & + A_{\mathrm{SMR}} \frac{(B_{\mathrm{ext}} - B_{\mathrm{res}})\Delta B}{(B_{\mathrm{ext}} - B_{\mathrm{res}})^2 + \Delta B^2} \Bigg] \cos\varphi \sin 2\varphi, \end{aligned} \tag{7.3}$$

where

$$\begin{aligned} S_{\mathrm{SP}} &= \frac{l\rho J_{\mathrm{r}}^{\mathrm{P}} C}{4\Delta B^2} \Bigg[\quad C_+ B_{\mathrm{Oe}}^2 + C_- B_{\mathrm{STT}}^2 \\ &\qquad + C \left((2+\alpha^2)\sin\delta - \frac{\alpha}{\tilde{\omega}_{\mathrm{a}}} \cos\delta \right) B_{\mathrm{Oe}} B_{\mathrm{STT}} \Bigg], \\ S_{\mathrm{SMR}} &= -\frac{l\Delta\rho_1 j_{\mathrm{c}}}{4\Delta B} \left[C B_{\mathrm{STT}} + (C_+ \sin\delta + \alpha C \cos\delta)\, B_{\mathrm{Oe}} \right], \\ A_{\mathrm{SMR}} &= -\frac{l\Delta\rho_1 j_{\mathrm{c}}}{4\Delta B} \left(C_+ \cos\delta - \alpha C \sin\delta \right) B_{\mathrm{Oe}}. \end{aligned}$$

Before going into details below, it is advisable to point out some general features of Eq. (7.2) and Eq. (7.3). The DC spin pumping voltage V_{SP} takes the form of a symmetric Lorentzian with magnitude S_{SP} governed by the Oersted field B_{Oe} as well as the effective magnetic field parameterizing the (anti-)damping torque B_{STT}. On the other hand, the DC rectification voltage V_{SMR} is composed of a symmetric and an antisymmetric Lorentzian with magnitude S_{SMR} and A_{SMR}, respectively; the former depends on both B_{Oe} and B_{STT} while the latter only depends on B_{Oe}.

The remaining parameters in Eqs. (7.2) and (7.3) are as follows: l is the length of the sample, φ is the angle between the current and the applied in-plane magnetic field (*cf.* Fig. 7.1) with modulus $B_{\mathrm{ext}} = \mu_0 H_{\mathrm{ext}}$, δ is the constant phase offset between microwave current and magnetization precession [233, 236, 238] as discussed above, and the magnetic field $\Delta B = \alpha\omega_{\mathrm{a}}/\gamma$ is the half width (half maximum) of the resonance governed by the Gilbert damping constant α and the excitation angular frequency $\omega_{\mathrm{a}} = 2\pi f_{\mathrm{mw}}$. $C = \tilde{\omega}_{\mathrm{a}}/\sqrt{1+\tilde{\omega}_{\mathrm{a}}^2}$ and $C_\pm = 1 \pm 1/\sqrt{1+\tilde{\omega}_{\mathrm{a}}^2}$ where $\tilde{\omega}_{\mathrm{a}} = 2\omega_{\mathrm{a}}/(M_{\mathrm{s}}\gamma\mu_0)$ with the gyromagnetic ratio γ. Furthermore, $J_{\mathrm{r}}^{\mathrm{P}} = \hbar\omega_{\mathrm{a}}/(2ed_{\mathrm{N}}\rho)\theta_{\mathrm{SH}}\eta$ and $B_{\mathrm{res}} = -M_{\mathrm{s}}\mu_0/2 + \sqrt{(M_{\mathrm{s}}\mu_0/2)^2 + (\omega_{\mathrm{a}}/\gamma)^2}$. Finally, the total damping is given by $\alpha = \alpha_0 + \gamma\hbar^2/(2e^2 M_{\mathrm{s}} d_{\mathrm{F}})\,\mathrm{Re}[G^{\uparrow\downarrow}/(1+2\rho\lambda G^{\uparrow\downarrow}\coth\frac{d_{\mathrm{N}}}{\lambda})]$, where the parameter α_0 combines the intrinsic Gilbert damping of the YIG film with its inhomogeneous broadening. Throughout this chapter (Ch. 7.1) α_0 will thus be treated as a fitting parameter. A more elaborate discussion and analysis of the damping in thin YIG films is found in Ch. 7.2.

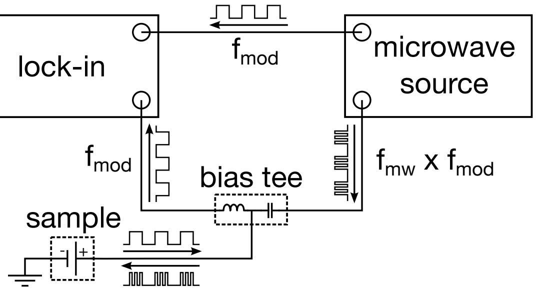

Figure 7.2.: Circuit schematic used for the ferromagnetic resonance experiments. Equipment used: Rohde & Schwarz SMF100A microwave source, Stanford Research SR830 lock-in amplifier, Inmet/Aeroflex 8810EMF2-50 bias-tee.

7.1.2 *Experimental methods*

For the experiments YIG/Pt samples (*cf.* Ch. 3) are integrated into a coplanar waveguide (CPW) structure with a characteristic impedance of $50\,\Omega$ and placed onto a 1.5 mm wide gap in the center conductor [186] as depicted in Fig. 7.1. The sample dimensions are designed to, as far as possible, impedance match the microwave circuitry, leading to an effective sample area of about $1.5\,\mathrm{mm} \times 1.5\,\mathrm{mm}$. The CPW with the integrated sample is placed between the pole shoes of a rotatable electromagnet. In the experiments, an intensity modulated microwave source ($f_{\mathrm{mw}} = 7\,\mathrm{GHz}$) is used to feed the samples with an AC charge current. The ensuing DC voltages are detected by a lock-in amplifier as depicted in Fig. 7.2. All experiments were performed under ambient conditions.

For a detailed schematic see Fig. A.1.

7.1.3 *In-plane measurements and simulations*

Ferromagnetic resonance studies have been performed for three samples with strategically chosen film thicknesses [YIG(55 nm)/Pt(17 nm), YIG(55 nm)/Pt(4 nm) and YIG(4 nm)/Pt(3 nm)] which allows to disentangle Oersted and spin transfer torque contributions to V_{DC}. As shown in Fig. 7.3a a mostly symmetric *negative* voltage peak is observed at the resonance magnetic field $\mu_0 H_{\mathrm{ext}} \approx 0.18\,\mathrm{T}$ for the YIG(55 nm)/Pt(17 nm) sample. To evaluate the importance of the spin transfer torque, the experimentally observed voltages are simulated using the model described in Ch. 7.1.1 [Eqs. (7.2) and (7.3)]. The term *simulation* thereby signifies that the data are not fitted numerically but that the free parameters in the simulation are chosen by hand, as Eqs. (7.2) and (7.3) are not well-behaved with respect to typical minimization algorithms such as the Newton or Levenberg-Marquardt [239, 240] method. It is also important to acknowledge that the accuracy of the numerical values

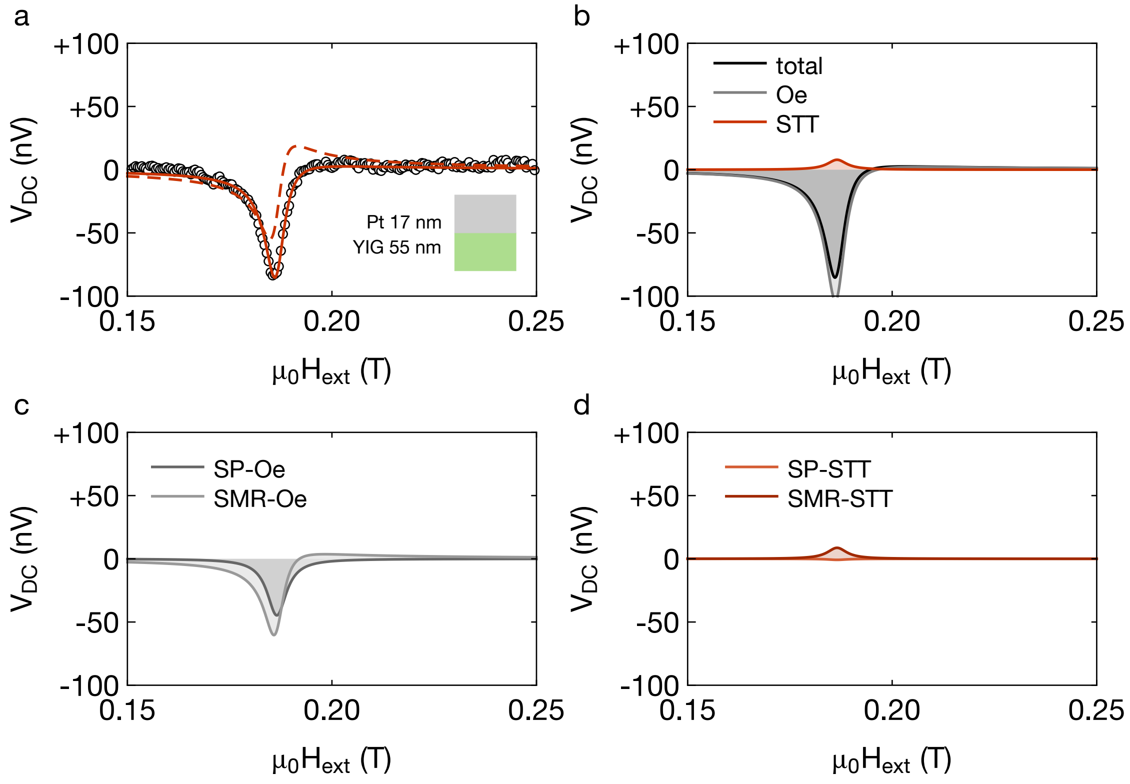

Figure 7.3.: **a** Measured DC voltage V_{DC} of YIG(55 nm)/Pt(17 nm) under an AC current bias (full symbols). The solid/dashed red line is calculated from a simulation based on Eqs. (7.2) and (7.3) using $\delta = -63°/\delta = 0$, respectively. The angle between the (in-plane) external magnetic field and the microwave current is $\varphi \cong -35°$ [$\theta = 90°$, Fig. 7.1]. **b** Contributions to the excitation by Oersted field and spin transfer torque to V_{DC}, according to the simulation. The Oersted fields dominate the magnetization actuation. **c** Oersted field induced contributions to V_{SP} and V_{SMR}. **d** Spin transfer torque induced contributions to V_{SP} and V_{SMR}.

given in the following is adversely affected by the large and partly correlated parameter space of Eqs. (7.2) and (7.3). Nevertheless, any plausible parameter set will qualitatively yield very similar and thus robust results regarding the contributions of Oersted field and spin transfer torque. Moreover, most parameters are constrained (by literature or other measurements) leaving only the charge current density j_c and the intrinsic damping parameter α_0 as free parameters in the model calculations. These, however, can also be estimated from the applied microwave source power, impedance matching characteristics and the damping parameters extracted from spin pumping experiments on the YIG/Pt samples [185]. The spin transport parameters are: spin diffusion length $\lambda = 1.5\,\mathrm{nm}$, spin Hall angle $\theta_{\mathrm{SH}} = 0.11$ and spin mixing conductance $\mathrm{Re}(G^{\uparrow\downarrow}) = 4 \times 10^{14}\,\Omega^{-1}\mathrm{m}^{-2}$ which have proven to be robust to variations of other sample parameters (Refs. [48, 185, 199]). The phase $\delta = -63°$ is inferred from additional measurements with magnetic fields oriented at a slight angle to the film normal (see Ch. 7.1.4). The saturation magnetization $M_\mathrm{s} = 118\,\mathrm{kA/m}$ is determined from the magnetic resonance field, and $\rho = 445 \times 10^{-9}\,\Omega\mathrm{m}$ from DC resistance measurements. For $j_\mathrm{c} = 0.53 \times 10^{9}\,\mathrm{A/m^2}$ and $\alpha_0 = 0.01$, good quantitative agreement between model and experiment [Fig. 7.3(a)] is obtained. The large effective intrinsic damping α_0 in the samples can be understood in terms of efficient magnon-magnon-scattering induced by roughness in thin ferromagnetic films [241, 242], especially when magnetized in the film plane [243].

cf. *Ch.* 7.2

After finding good agreement of the simulated and the measured V_DC the simulation allows to infer the contributions due to the Oersted field and spin transfer torque, as depicted Fig. 7.3b. The excitation in this sample is dominated by the Oersted field as expected for the comparably large YIG layer thickness. The largely symmetric shape of the resonance peak is due to a significant spin pumping contribution, with the spin Hall magnetoresistance being small ($\Delta\rho/\rho \approx 2 \times 10^{-4}$) [11, 48] for thick Pt films. Splitting Oersted field and spin torque contributions further into spin pumping and spin Hall magnetoresistance components shows that the Oersted field approximately equally efficient excites spin pumping and spin Hall magnetoresistance voltages (Fig. 7.3c) and that the spin transfer torque contributes little to no spin pumping voltage (Fig. 7.3d). As a note of caution, however, the spin pumping voltage (Eq. (7.2) also contains terms mixing Oersted field and the effective magnetic field parameterizing the (anti-)damping torque which are then unaccounted for in Figs. 7.3c,d and the corresponding panels for the other two samples below.

In the YIG(55 nm)/Pt(4 nm) sample with its smaller Pt thickness, a distinct asymmetric V_DC resonance line shape (Fig. 7.4a) is observed. This particular sample shows a somewhat higher resonance field and absolute voltage level due to a reduced saturation magnetization and better impedance matching, respectively. Again, the experimental data are well reproduced by the simulation using $M_\mathrm{s} = 89\,\mathrm{kA/m}$, $j_\mathrm{c} = 4 \times 10^{9}\,\mathrm{A/m^2}$, $\rho = 317 \times 10^{-9}\,\Omega\mathrm{m}$, $\delta = -55^\circ$ and $\alpha_0 = 0.015$. The spin Hall magnetoresistance is known to be maximal for a Pt thickness of roughly twice the spin diffusion length [48] $d_\mathrm{N} \approx 2\lambda = 3\,\mathrm{nm}$. The antisymmetric shape here then is due to significantly increased spin Hall magnetoresistance rectification as compared to the YIG(55 nm)/Pt(17 nm) sample (Figs. 7.4c,d). The smaller d_N also enhances the effective field describing the (anti-)damping torque. However, since the YIG layer is still comparably thick, the Oersted field still accounts for most of the excitation (Fig. 7.4b).

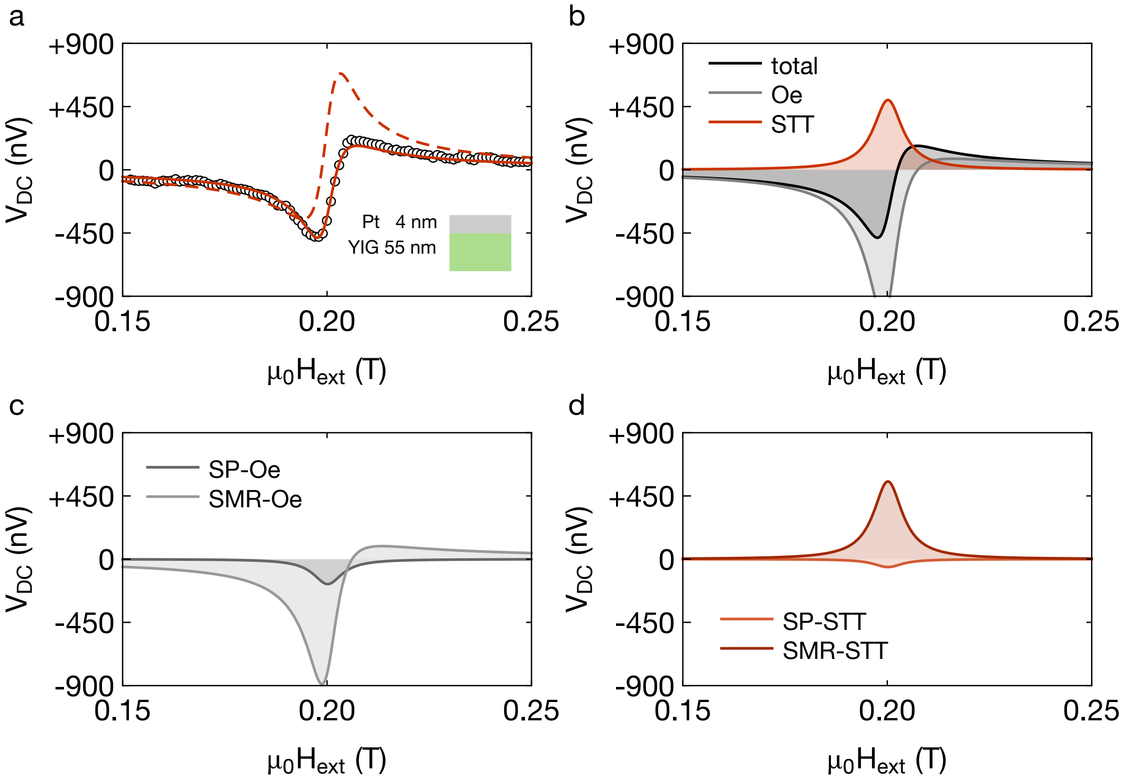

Figure 7.4.: **a** Measured DC voltage V_{DC} of YIG(55 nm)/Pt(4 nm) under an AC current bias (full symbols). The solid/dashed red line is calculated from a simulation based on Eqs. (7.2) and (7.3) using $\delta = -55°/\delta = 0$, respectively. The angle between the (in-plane) external magnetic field and the microwave current is $\varphi \cong -35°$ [$\theta = 90°$, Fig. 7.1]. **b** Contributions to the excitation by Oersted field and spin transfer torque to V_{DC}, according to the simulation. While the smaller d_{N} benefits the effective field describing the (anti-)damping torque the magnetization dynamics are still dominantly induced by the Oersted field. **c** Oersted field induced contributions to V_{SP} and V_{SMR}. **d** Spin transfer torque induced contributions to V_{SP} and V_{SMR}.

The YIG(4 nm)/Pt(3 nm) sample behaves markedly different. Here, a broad *positive voltage* peak which indicates spin transfer torque excitation (Fig. 7.5a) is observed. With decreasing YIG film thickness, the effect of surface roughness on the magnetization damping is increased. This is taken care of in the simulations with $M_{\mathrm{s}} = 128\,\mathrm{kA/m}$, $j_{\mathrm{c}} = 1.1 \times 10^{9}\,\mathrm{A/m^2}$, $\rho = 481 \times 10^{-9}\,\Omega\mathrm{m}$, $\delta = -78°$ and $\alpha_0 = 0.04$. The symmetric line shape in Fig. 7.5b is caused by the dominant spin transfer torque component, both for the spin pumping and spin Hall magnetoresistance component of V_{DC} (Fig. 7.5c,d).

As an additional sanity check of the modeling a rotation of the external magnetic field as a function of the in-plane angle φ has also been performed. The result depicted in Fig. 7.6 agrees well with the behavior predicted by Eqs. (7.2) and (7.3) and thus demonstrates that

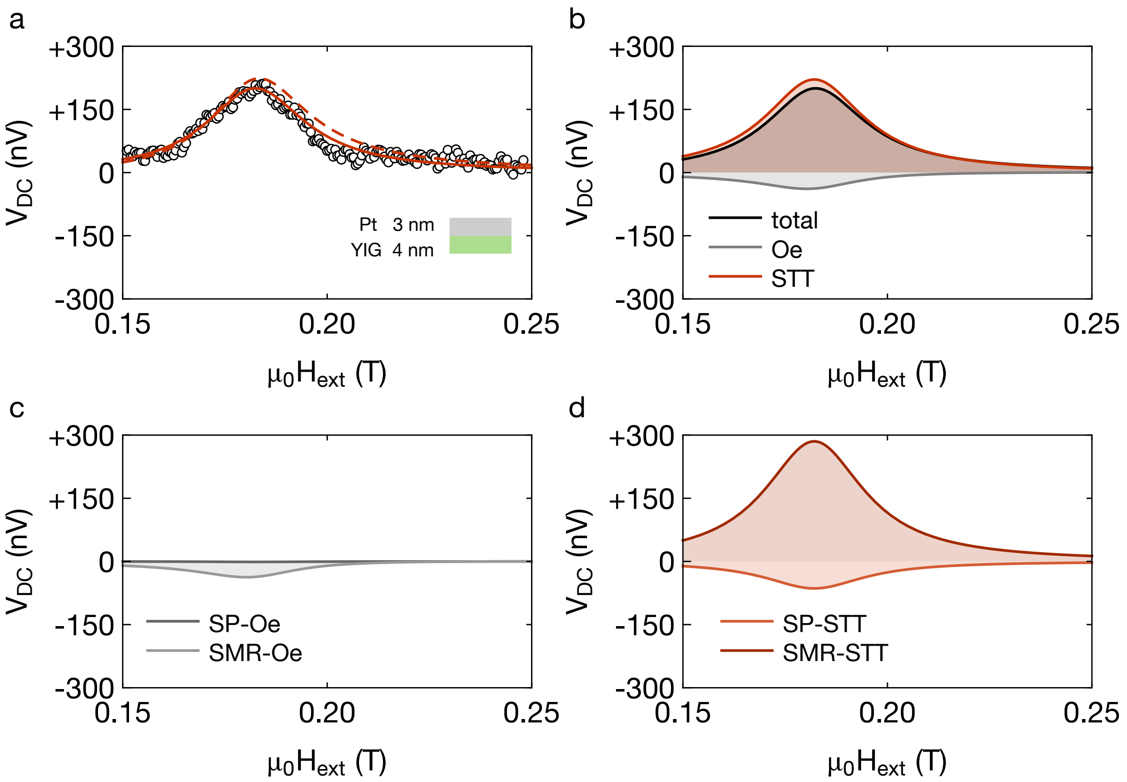

Figure 7.5.: **a** Measured DC voltage V_{DC} of YIG(4 nm)/Pt(3 nm) under an AC current bias (full symbols). The solid/dashed red line is calculated from a simulation based on Eqs. (7.2) and (7.3) using $\delta = -78^\circ / \delta = 0$, respectively. The angle between the (in-plane) external magnetic field and the microwave current is $\varphi \cong -35^\circ$ [$\theta = 90^\circ$, Fig. 7.1]. **b** Contributions to the excitation by Oersted field and spin transfer torque to V_{DC}, according to the simulation. The spin transfer torque dominates the excitation of the magnetization dynamics due to the very thin YIG layer. **c** Oersted field induced contributions to V_{SP} and V_{SMR}. **d** Spin transfer torque induced contributions to V_{SP} and V_{SMR}.

spurious effects and anisotropy are not significant for the in-plane measurements, at least in this particular sample. It should be noted, however, that behavior deviating from the expected $\cos\varphi \sin 2\varphi$ in thicker YIG films has been reported in Ref. [244] and is also observed and discussed further in Ch. 7.2.

7.1.4 *Out-of-plane measurements and extraction of the phase offset*

As discussed in Sec. 7.1.3, the measured DC voltages, especially their dependence on the thickness of the YIG and Pt layer, are well reproduced by theory. As seen in Figs. 7.3, 7.4 and 7.5, the best match between theory and experiment is achieved, however, only by allowing for $\delta \neq 0$ in Eqs. (7.2) and (7.3). Although good agreement is obtained for $\delta \neq 0$, one has to keep in mind that the Oersted field-

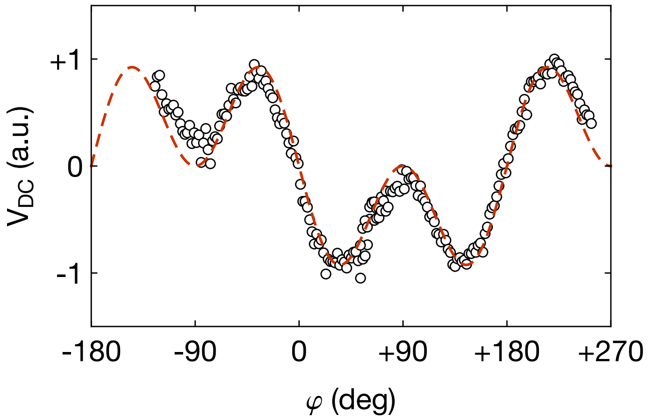

Figure 7.6.: Normalized DC voltage recorded on the YIG(4 nm)/Pt(3 nm) sample on resonance as a function of the external magnetic field orientation φ. The dashed line sketches the expected $\cos\varphi \sin 2\varphi$ variation of V_{DC}.

induced spin Hall magnetoresistance rectification voltage [Eq. (7.3)] then also contributes to the symmetric line shape. Therefore, the phase offset δ must be determined in order to conclusively establish the role of the spin transfer torque vs. the Oersted field. While both V_{SP} and V_{SMR} vanish for magnetic fields in the plane spanned by the film normal and the charge current direction [236], i.e. $\varphi = 0°$, for any other value of φ their magnitude is differently affected by the polar (out-of-plane) angle θ between the film normal and the magnetization direction [235]. More specifically, the ratio R of the symmetric (S) to antisymmetric (A) contributions to the line shape [233] changes characteristically as a function of θ for a given δ. A pronounced change in R is observed for $\theta \to 0°$ i.e., for magnetization nearly perpendicular to the film plane. Since the DC voltage vanishes for $\theta = 0°$, however, it is not possible to take data with the magnetic field exactly perpendicular to the film stack. For all samples additional experiments (Fig. 7.7) with the magnetic field applied at a small angle to the film normal ($\theta \approx 5°$, $\varphi = 90°$, Fig. 7.1.3) have thus been carried out. A *direct* computation of the experimental out-of-plane resonance spectra is unfortunately not possible as magnetocrystalline anisotropy other than shape anisotropy is not accounted for in Refs. [234, 235] but affects the resonance field in the out-of-plane measurements. The measured value may further be affected by the different sample position in the magnet for the out-of-plane configuration. The line shape itself, however, is hardly affected for typical crystalline anisotropy strengths in these thin films. The phase offset δ can then be determined by extracting R for the in-plane and out-of-plane measurements and adjusting δ such that both the in-plane and out-of-plane R value are

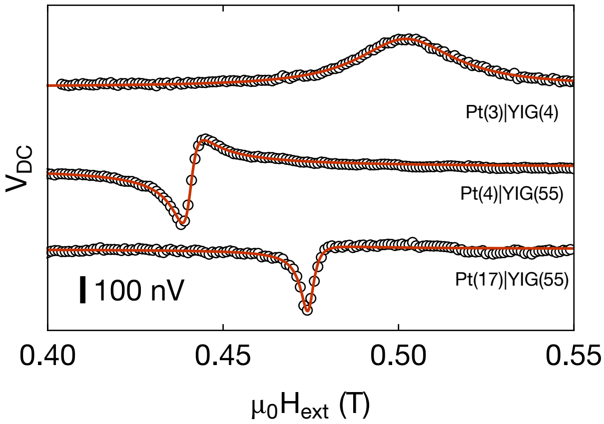

Figure 7.7.: Measured and fitted DC voltages for external fields applied at a slight angle $\theta \approx 5°$ relative to the film normal on the YIG(55 nm)/Pt(17 nm), YIG(55 nm)/Pt(4 nm) and YIG(4 nm)/Pt(3 nm) sample, respectively.

reproduced. This procedure is essentially the same as introducing an artificial resonance field offset in the simulation to counteract the effect of the unaccounted resonance field shifts. $R = S/A$ is obtained by fitting the experimental data assuming a generalized Lorentzian, i.e.

$$\begin{aligned} V_{\mathrm{DC}} &= S\frac{\Delta B^2}{(B_{\mathrm{ext}}-B_{\mathrm{res}})^2+\Delta B^2} \\ &\quad + A\frac{\Delta B(B_{\mathrm{ext}}-B_{\mathrm{res}})}{(B_{\mathrm{ext}}-B_{\mathrm{res}})^2+\Delta B^2}, \end{aligned} \tag{7.4}$$

where ΔB is the (half width half maximum) linewidth, B_{res} is the resonance field, B_{ext} is the external field and S and A are the amplitudes of the symmetric and antisymmetric contributions to the line shape. For the simulation all terms associated with the imaginary part of the spin mixing conductance have been disregarded and it is assumed that the static magnetization is oriented along the external field direction. Since the out-of-plane magnetic resonance fields are of the order of 450 mT (*cf.* $\mu_0 M_{\mathrm{s}} \lesssim 160\,\mathrm{mT}$), $\mathrm{Re}(G^{\uparrow\downarrow}) \gg \mathrm{Im}(G^{\uparrow\downarrow})$ in the YIG/Pt samples [48] and the Oersted as well as the effective field describing the (anti-)damping torque both lie in the film-plane when $\theta \to 0°$, these assumptions are not expected to compromise the results.

The experimental R values are found as $R_{\mathrm{ip}} = -3.2$, $R_{\mathrm{oop}} = -2.5$ for the YIG(55 nm)/Pt(17 nm) sample, $R_{\mathrm{ip}} = -0.43$, $R_{\mathrm{oop}} = -0.35$ for the YIG(55 nm)/Pt(4 nm) sample and $R_{\mathrm{ip}} = 19$, $R_{\mathrm{oop}} = 25$ for the YIG(4 nm)/Pt(3 nm) sample. The subscripts ip and oop indicate magnetic field in the film plane and (approximately) out of plane, respectively.

A comparison with the simulation based on Ref. [235] then yields phase offsets of $\delta = -63°$ [YIG(55 nm)/Pt(17 nm)], $\delta = -55°$ [YIG(55 nm)/Pt(4 nm)] and $\delta = -78°$ [YIG(4 nm)/Pt(3 nm)], respectively. The R value of the YIG(4 nm)/Pt(3 nm) sample is most uncertain causing a phase offset error of about $\pm 3°$.

7.1.5 *Summary*

The pronounced dependence of the V_{DC} resonance spectra on the thicknesses of the yttrium iron garnet and platinum layers (d_{F} and d_{N}), observed in experiment and accurately reproduced by the model, provides clear evidence for spin transfer torque driven magnetization dynamics in thin yttrium iron garnet films. In particular, the polarity change of the DC voltage in the thinnest film is a strong indicator for spin transfer torque driven dynamics. From a different perspective, the results presented above also show that AC spin pumping [245–247] in magnetic insulators is reciprocal, as predicted by the Onsager relations for the linear response regime. This corroborates the notion that spin transfer torques provide an efficient link between pure magnonic and conventional electronic circuits, in particular on the nanometer scale. While Oersted fields drive bulk magnetization dynamics, the spin transfer torque is linked to the interface and is thus very effective for thin film structures. Magnetic insulators specifically can be engineered for low saturation magnetization [248], further increasing the effectiveness of spin transfer torque mediated magnetization actuation. Recent results [224, 231] also indicate that the spin transfer torque may be able to couple to the Néel order parameter in antiferromagnetic insulators which could allow for very high-frequency dynamics. This opens new perspectives for the efficient integration of ferro-, ferri-, and antiferromagnetic insulators, in the form of e.g. spin transfer torque magnetic random access memory (STT-MRAM) or and spin-wave based interconnects, into electronic devices.

When this study was initially performed the origin of the phase offset δ was not known. The more recent results in Ch. 7.2 give a number of important insights into this issue but, unfortunately, do not allow to eliminate δ from the analysis of the fundamental (FMR) mode in a simple manner.

7.2 BROADBAND SPIN WAVE SPECTROSCOPY USING THE SPIN TRANSFER TORQUE

Resonant excitation of magnetization dynamics as demonstrated in the preceding chapter allows to encode information into a magnetostatic mode, e.g. in an amplitude modulation scheme. Resonant excitation, however, is only possible at specific field-frequency combinations of which only a small subset has been explored in Ch. 7.1. In principle, several modes, at different frequencies, can be excited at the same field value simultaneously. To account for these additional modes the theory of ferromagnetic resonance, introduced in Ch. 2.4 has to be extended. Magnetization dynamics can be described by the phenomenological Landau-Lifshitz-Gilbert equation, from which Kittel [51] first derived the ferromagnetic resonance condition. Spin wave theory is a generalization of Kittel's approach and also considers surface- as well as higher order volume modes. This gives rise to a large spectrum of possible excitation states for the magnetic system and has been explored in great detail for many different materials [249, 250].

Magnetostatic spin waves are also called magnetostatic modes.

In spin wave theory one distinguishes between spin waves of magnetostatic and dipolar exchange character. Although this differentiation is not particularly well defined one may use the criterion [250] $(l_{\mathrm{ex}}q^*)^2 \gg 1$, with the magnetic exchange length $l_{\mathrm{ex}} = \sqrt{D/(\gamma\mu_0\hbar M_{\mathrm{s}})}$ and the magnitude of the in-plane part of the wave vector $\boldsymbol{q}^*$, to characterize the (dipolar) exchange regime. The out-of-plane component q_n (parallel to the film normal) is required to be quantized by the boundary conditions of the magnetostatic equations governing the problem. Due to the quantization the out-of-plane wave vector takes the form of a standing wave. If the in-plane (or propagating) character of magnetostatic spin waves is of interest one further divides the possible configurations into three classes. *Forward volume waves* describe the case of spin waves propagating in the plane of a magnetic film, magnetized parallel to its surface normal. For an in-plane magnetized film, *backward volume waves* describe the case when the (in-plane) propagation is along the magnetization direction and *surface waves* describe the case when the two are perpendicular to each other.

The spin waves of interest in the following, however, are analyzed only for their quantized component which is perpendicular to their propagation in the film plane. With this in mind, the resonance frequency of the perpendicular magnetostatic volume modes in a laterally infinite thin film with an external field in its film plane is found as [249, 250]

$$f_{\mathrm{res}} = \frac{\gamma\mu_0}{2\pi}\sqrt{[H_{\mathrm{ext}} + M_{\mathrm{s}}l_{\mathrm{ex}}^2q_n^2][H_{\mathrm{ext}} + M_{\mathrm{s}} - K + M_{\mathrm{s}}l_{\mathrm{ex}}^2q_n^2]}, \tag{7.5}$$

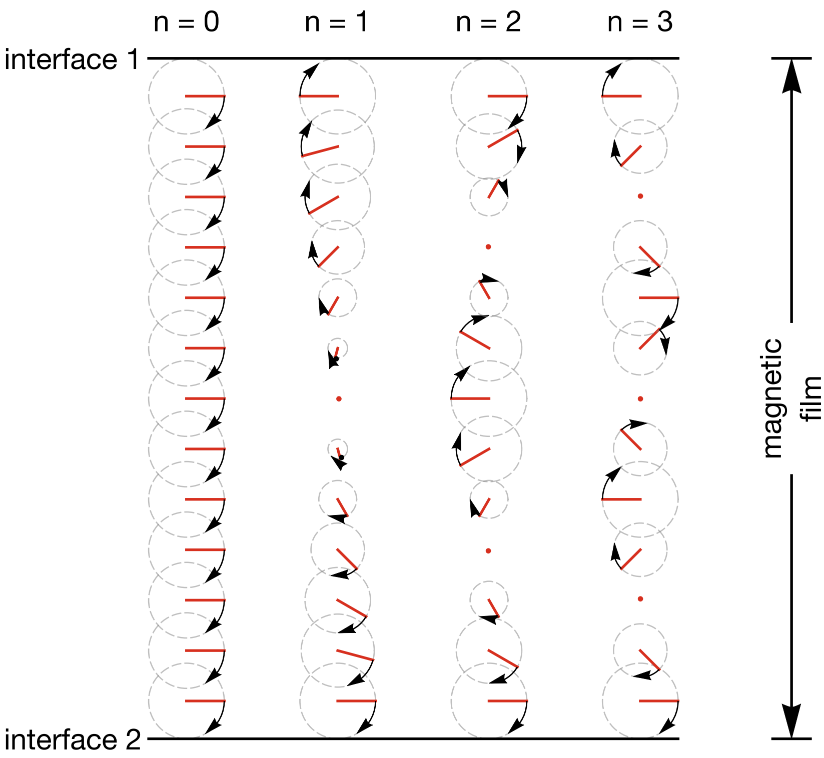

Figure 7.8.: Perpendicular standing spin wave modes in a magnetic film. The red lines indicate the dynamic magnetization components perpendicular to the external magnetic field.

$n \in \mathbb{N}$ *for* $K = 0$.

where H_{ext} is the magnitude of the external magnetic field, K is the sum of the magnetocrystalline anisotropies, and $q_n = n\pi/d_{\text{F}}$ is the quantized part of the wave vector with d_{F} the thickness of the film and n the order of the mode. The Kittel formula [51] is recovered from Eq. (7.5) by taking $n = 0$.

Whether or not a specific mode can be excited also depends on its spatial profile. Figure 7.8 depicts the spatial profile of the precession amplitudes and phases for the $n = 0, 1, 2, 3$ mode in the case of negligible surface anisotropy. Notably the phase of the magnetization precession throughout the entire film thickness is constant for the $n = 0$ mode but varies in sign for the $n = 1$ and higher order modes. Hence a uniform force (such as the one exerted by a spatially uniform Oersted field) acting on the magnetization is limited to the excitation of the $n = 0$ mode and fails to couple to the other modes for the net force vanishes under consideration of the phase differences throughout the film. Note that for strong surface anisotropy (*pinned* boundary conditions) this is only true for the odd modes ($n = 1, 3, 5, \dots$). Since the spin torque acts only in the immediate proximity of the interface, the mode profile within the films does not affect the effectiveness of spin transfer driven magnetization excitation. In nanostructures in particular, where Oersted fields can, in many cases, be considered homogeneous, interface effects such as the spin transfer torque therefore represents the only option to excite these modes. This is especially true for insulating magnets, that can not efficiently screen Oersted fields as is the case in metallic magnets.

It is worth noting that spin pumping affects the mode profiles [251]. For in-plane wave vectors $q^* \approx 0$, relevant for the experiments in the following, however, this effect is negligibly small.

A further point to consider is that the demonstration of spin torque actuated magnetization dynamics in the preceding chapter and in the literature [232, 244, 252–254] hinges on the analysis of the line shape by comparison with theory [234–236]. While the latter provides a powerful tool for the interpretation of the data or the design of new experiments, the large parameter space of the corresponding equations [*cf.* Eqs. (7.2) and (7.2)] can be an issue. Since the $n > 0$ modes in thin insulating films are largely immune to the influence of the Oersted fields generated in the experiment, their mere detection constitutes a direct proof of spin torque actuated magnetization dynamics.

7.2.1 *Spatial profile of the Oersted field*

For the experiment a 105 nm thick YIG film covered by a 5 nm thin Pt layer is connected to a coplanar waveguide as depicted in Fig. 7.1 and the experiment is performed analogously to Ch. 7.1. While thinner magnetic films are beneficial for the magnitude of the spin transfer torque, a thicker film permits more magnetostatic modes to be observed within a given frequency window as evident from Eq. (7.5). To facilitate measurements over a broad frequency range at reasonable signal to noise levels, the output power of the microwave source is adjusted between $P_{\mathrm{mw}} = 4 - 100\,\mathrm{mW}$ as a function of the microwave frequency to compensate for losses in the circuitry and to yield approximately the same DC voltage levels throughout the entire investigated frequency spectrum.

The magnitude of time varying Oersted field generated by the high-frequency charge current is approximated in Ch. 7.1.1 by the constant value $B_{\mathrm{Oe}} = j_{\mathrm{c}} d_{\mathrm{N}} \mu_0 / 2$, but its spatial variation can also be calculated

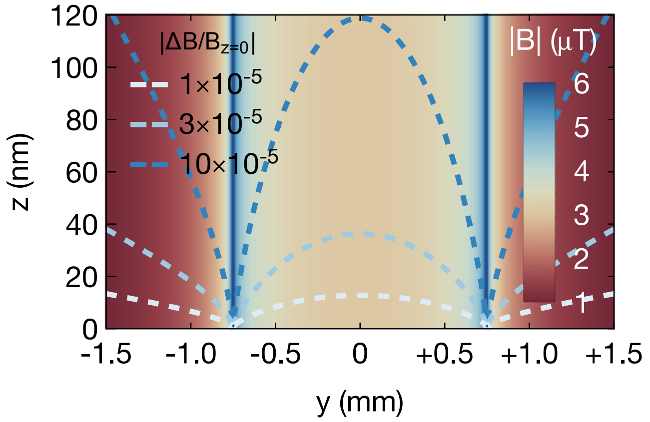

Figure 7.9.: Magnitude of the Oersted field generated by a 1.5 mm wide, 5 nm thick Pt strip at a constant current density of $j_\mathrm{c} = 1 \times 10^9\,\mathrm{A/m^2}$. The Pt strip is located outside of the plotted region at $-0.75\,\mathrm{mm} \leq y \leq 0.75\,\mathrm{mm}$, $-5\,\mathrm{nm} \leq z \leq 0\,\mathrm{nm}$. The dashed (contour) lines give the relative deviation of the field from its value at the interface.

analytically for a thin film, i.e. a rectangular conductor [255, 256]. Using[2]

$$\begin{aligned}\tilde{B}_y(p_0, z_0) = \frac{\mu_0 j_\mathrm{c}}{4\pi}\Bigg[& p_0 \log\left(1 + \frac{h^2 + 2z_0 h}{p_0^2 + z_0^2}\right) + 2(z_0 + h)\arctan\left(\frac{p_0}{z_0 + h}\right) \\ & -2z_0 \arctan\left(\frac{p_0}{z_0}\right)\Bigg] \qquad (7.6)\end{aligned}$$

and

$$\begin{aligned}\tilde{B}_z(p_0, z_0) = \frac{\mu_0 j_\mathrm{c}}{4\pi}\Bigg[& z_0 \log\left(1 + \frac{p_0^2}{z_0^2}\right) - (z_0 + h)\log\left(1 + \frac{p_0^2}{(z_0 + h)^2}\right) \\ & -2p_0 \arctan\left(\frac{z_0 + h}{p_0}\right) + 2p_0 \arctan\left(\frac{z_0}{p_0}\right)\Bigg], \qquad (7.7)\end{aligned}$$

the magnetic field at a given position (y_0, z_0) above the top edge of the conductor is then given by $B_{y(z)}(y_0, z_0) = \tilde{B}_{y(z)}(\frac{w}{2} + y_0, z_0) - \tilde{B}_{y(z)}(-\frac{w}{2} + y_0, z_0)$. In the equations above, h is the height of the conductor and w is its width.

Setting $w = 1.5\,\mathrm{mm}$, $h = d_\mathrm{N} = 5\,\mathrm{nm}$ and assuming a constant current density $j_\mathrm{c} = 1 \times 10^9\,\mathrm{A/m^2}$ yields the profile depicted in Fig. 7.9. In the center of the strip ($y = 0$) the field value from the full expression above agrees with the approximated value to within less than a percent. This error becomes larger towards the edges of the film due to the additional z-component of the Oersted field here. The variation of the magnitude of the Oersted field along the y-direction,

The z-component of the Oersted field has opposite sign for the left and right edge of the Pt strip.

---

[2] *Magnetic field of rectangular conductor with current*. Retrieved December 29, 2015, from http://www.ntmdt.com/spm-basics/view/magnetic-field-rectangular-wire

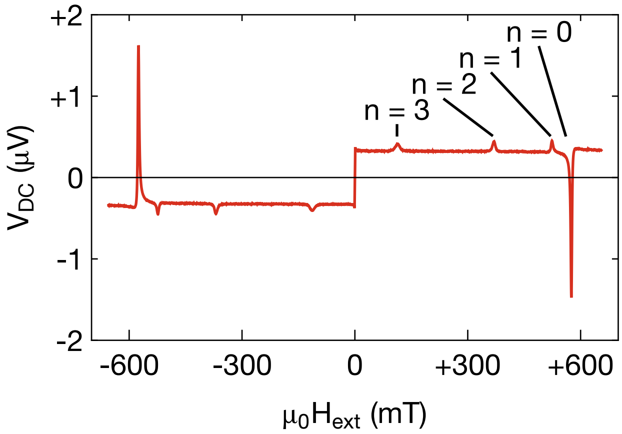

Figure 7.10.: DC Voltage recorded at $f_{\mathrm{mw}} = 18.5\,\mathrm{GHz}$ and $\varphi = 35°$. Modes up to $n = 3$ are clearly visible in the spectrum (higher spin wave modes appear at lower magnetic field magnitudes). The step in the DC voltage level at zero field, originates from the spin Seebeck effect.

however, does not lead to the excitation of the magnetostatic modes of interest, which require a variation along the z-direction. The latter is very small as outlined by the dashed (contour) lines that give the relative deviation of the Oersted field magnitude with respect to its value directly at the interface. The deviation barely exceeds 10^{-4} throughout the YIG film thickness of 105 nm, and the Oersted field should thus not be expected to contribute substantially to the excitation of the $n = 1, 2, 3, \ldots$ mode. Fundamentally, standing spin waves are also possible in the other two directions, however, the large sample dimensions here prevent the detection of such modes.

The discussion above hinges on the assumption of a uniform current distribution within the Pt layer, from which deviations are to be expected in the experiment due to nonuniform resistivity (e.g. edge defects) and the skin effect. The latter results in an increased current density at the far edges of the film at high frequencies. Both phenomena are likely to increase the Oersted field inhomogeneity overall but should have only limited influence on the variation along the z-direction in the region of interest.

7.2.2 *Voltage spectra analysis*

The DC voltage on the YIG(105 nm)/Pt(5 nm) sample has been recorded over a microwave frequency range of $5\,\mathrm{GHz} \leq f_{\mathrm{mw}} \leq 18.5\,\mathrm{GHz}$ in increments of 500 MHz at an in-plane angle between microwave current and external magnetic field of $\varphi = 35°$. A typical DC voltage spectrum is depicted in Fig. 7.10 for $f_{\mathrm{mw}} = 18.5\,\mathrm{GHz}$. Both for positive and negative external magnetic fields four voltage peaks can be identified, as well as a step in the DC voltage around zero external magnetic field. The sudden step in the DC voltage arises from a Joule heating induced spin Seebeck effect as discussed in Ch. 5.3. On very close inspection the voltage step at zero field also coincides with a peak-like structure, which arises from the superposition of Oersted and external magnetic field, similar to the discussion in the same chapter. The resonance fields of the other, more pronounced voltage peaks allow their identification as the $n = 0$ (uniform precession) to $n = 3$ (perpendicular standing) spin wave modes. Immediately apparent is the different polarity of the $n = 1, 2, 3$ compared to the $n = 0$ mode. As discussed in Ch. 7 the voltage peaks generated by spin pumping and spin torque mediated spin Hall magnetoresistance rectification are of opposite sign. By comparison with the results from Ch. 6 and Ch. 7.1 it becomes clear that the voltage peak of the $n = 0$ mode can be attributed (at least partially) to spin pumping, whereas the peaks for the $n = 1, 2, 3$ modes are due to spin torque mediated rectification. Upon closer inspection (expanded upon later in the chapter) the $n = 0$ mode also contains a substantial antisymmetric component, whereas the $n = 1, 2, 3$ mode are largely symmetric. Since the antisymmetric line shape is a hallmark of the excitation by the Oersted field this observation is consistent with the expectation that only the $n = 0$ mode can be driven by the Oersted field. By the same argument also the significant difference in the peak height, which is comparable for the $n = 1, 2, 3$ mode, but much larger for the $n = 0$ mode can be explained. In fact, the quite similar peak height of the $n = 1, 2, 3$ modes and their polarity (as discussed above) further supports the notion of their spin torque driven origin. Even if the Oersted field is assumed to be substantially more inhomogeneous than anticipated the excitation efficiency should still be very different for each spin wave mode. On the other hand, as long as the interfacial amplitude of the magnetostatic modes remain unchanged for larger n, the spin transfer torque will excite all of them equally efficient. This topic will also be discussed in more detail later in the chapter.

Although the discussion in the following will show that the interpretation of the data can not be limited entirely to the simple case proposed at the beginning of this chapter, it is reasonable to interpret the observation of the higher order modes as an unambiguous proof of spin transfer torque actuated dynamics.

Figure 7.10, in some sense, represents the culmination of this thesis, in that it demonstrates *all* spin related phenomena discussed so far (spin pumping, spin Seebeck effect, Spin Hall effect, spin Hall magnetoresistance, spin transfer torque) in a single measurement.

To analyze this spectrum and the ones at other microwave frequencies in more detail, including the higher order modes, the data are

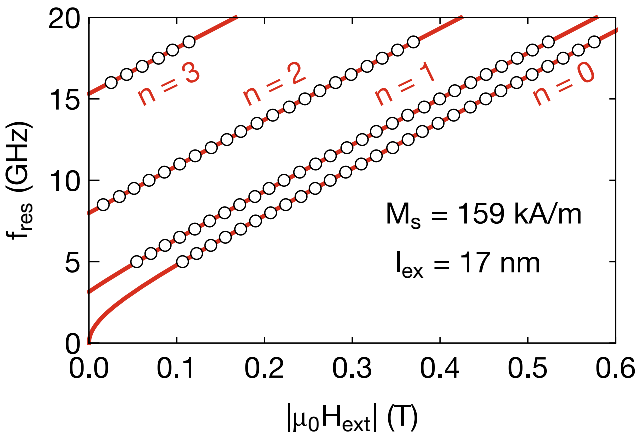

Figure 7.11.: Experimentally determined resonance frequencies of the $n = 0, 1, 2, 3$ mode as a function of the external magnetic field. The solid lines are a fit by Eq. (7.5) using the parameters given in the figure.

fitted in similar fashion to Eq. (7.4), i.e. each peak (spin wave mode n) is analyzed in terms of its symmetric and antisymmetric contributions to the generalized Lorentzian

$$\begin{aligned} V_{\mathrm{DC}}^{n} &= V_{\mathrm{symm}}^{n} \frac{\Delta B_n{}^2}{(B_{\mathrm{ext}} - B_{\mathrm{res}}^{n})^2 + \Delta B_n{}^2} \\ &\quad + V_{\mathrm{antisymm}}^{n} \frac{\Delta B_n (B_{\mathrm{ext}} - B_{\mathrm{res}}^{n})}{(B_{\mathrm{ext}} - B_{\mathrm{res}}^{n})^2 + \Delta B_n{}^2}, \end{aligned} \tag{7.8}$$

where $B_{\mathrm{ext}} = \mu_0 H_{\mathrm{ext}}$ is the external magnetic field and ΔB_n is the *half width half maximum* linewidth. Since the $n = 0$ and $n = 1$ mode are very close to each other or even partially overlap at high frequencies the fit is performed for the entirety of the positive (negative) external magnetic field branch (i.e. for all four peaks of a given magnetic field polarity) simultaneously. Resonance field and linewidth discussed in the following are the mean of the fitted values for the positive and negative external magnetic field branch (corrected for the negative sign of the peak amplitudes).

The resonance fields B_{res}^{n} of the modes allows for the extraction of a first set of information on the specimen. For ease of comparison with theory [Eq. (7.5)] Fig. 7.11 plots the pairs $(f_{\mathrm{mw}}, B_{\mathrm{res}}^{n})$ obtained in experiment as $(B_{\mathrm{ext}}, f_{\mathrm{res}})$, which merely represents a change in nomenclature and does not require any data manipulation. In the investigated frequency range f_{res} linearly increases with H_{ext} as expected from Eq. (7.5) in the limit $H_{\mathrm{ext}} > M_{\mathrm{s}}$ for the $n = 0$ mode and in the entire external magnetic field range for the $n = 1, 2, 3$ modes. Mode spacing and a linear extrapolation to $H_{\mathrm{ext}} = 0$ from the region of large H_{ext} allow to extract the magnetization M_{s} ($M_{\mathrm{s}} - K$ in the presence of anisotropy K) and exchange length l_{ex} by fitting the data simultaneously. This yields $M_{\mathrm{s}} = 159\,\mathrm{kA/m}$ and $l_{\mathrm{ex}} = 17\,\mathrm{nm}$ under the assumption of negligible surface anisotropy, i.e. $K = 0$ in Eq. (7.5). The saturation magnetization in this particular sample is rather large compared to some of the other samples investigated in this thesis (*cf.* Ch. 7.1) and the literature value of $M_{\mathrm{s}} \approx 140\,\mathrm{kA/m}$ [97], but not unheard of in the literature [160]. The magnetic exchange length l_{ex} relates to the exchange constant A_{ex} of the magnetic material by [39]

The sample was grown after a major maintenance of the growth cluster, which could explain the unexpectedly large M_{s}.

$$l_{\mathrm{ex}} = \sqrt{\frac{2A_{\mathrm{ex}}}{\mu_0 M_{\mathrm{s}}^2}}. \tag{7.9}$$

Inserting M_{s} and l_{ex} as determined above gives $A_{\mathrm{ex}} = 4.6\,\mathrm{pJ/m}$ which agrees with values ($A_{\mathrm{ex}} \approx 4\,\mathrm{pJ/m}$) reported for YIG in the literature [126, 257, 258], even if somewhat on the large side.

The discussion in the following will indicate that the assumption of negligible surface anisotropy is likely only an approximation for this particular sample. By allowing for $K \neq 0$ in Eq. (7.5) the wavevectors q_n are no longer integer multiples of π/d_{F} but instead have to fulfill the relation [259] $K_{\mathrm{s}} = A_{\mathrm{ex}} q_{\mathrm{n}} \tan(q_{\mathrm{n}} d_{\mathrm{F}})$ where $K_{\mathrm{s}}/(d_{\mathrm{F}}\mu_0 M_{\mathrm{s}}) = K$ is the surface anisotropy. Unfortunately, a fitting scheme that implemented this condition did prove to be rather sensitive to the starting parameters and was thus unable to deliver robust results. In many cases, however, the fit converged close to values $M_{\mathrm{s}} \approx 140\,\mathrm{kA/m}$, $A_{\mathrm{ex}} \approx 4\,\mathrm{pJ/m}$ and $K_{\mathrm{s}} \approx 1 \times 10^{-4}\,\mathrm{J/m^2}$ which appear compatible with the literature and the experiment.

This relation only holds for an in-plane magnetized sample with anisotropy on a single surface.

The linewidth ΔB_n of a spin wave mode is determined by a number of magnetization damping mechanisms [260, 261]. In yttrium iron garnet it is generally sufficient to consider only the frequency independent inhomogeneous broadening ΔB_n^0 and a frequency dependent component $\alpha(n) f_{\mathrm{mw}} 2\pi/\gamma$. As discussed in Ch. 7.1, $\alpha(n)$ is the sum of the intrinsic damping α_0 of the film, and a component due to spin pumping $\alpha_{\mathrm{SP}} = \gamma\hbar^2/(2e^2 M_{\mathrm{s}} d_{\mathrm{F}})\,\mathrm{Re}[G^{\uparrow\downarrow}/(1 + 2\rho\lambda G^{\uparrow\downarrow} \coth\frac{d_{\mathrm{N}}}{\lambda})]$. With an experimentally determined resistivity of $\rho = 375 \times 10^{-9}\,\Omega\mathrm{m}$ and the same spin transport parameters as in Ch. 7.1, the expected damping due to spin pumping is $\alpha_{\mathrm{SP}}^{n=0} = 0.0006$ for the fundamental ($n = 0$) mode in the investigated sample. For the $n = 1$ and higher order modes, however, the ratio of the precession amplitude at the interface compared to the total mode volume is enhanced by a factor of two which amplifies the coupling strength of the spin transfer torque to the magnetization by the same factor [262]. While this increases the effectiveness of the magnetization actuation by the spin transfer torque, also the damping figure due to spin pumping is twice as large, i.e. $\alpha_{\mathrm{SP}}^{n>0} = 0.0013$.

Figure 7.12 plots ΔB_n as extracted from the fit to the experiment. Clearly, the linewidth increases with mode the number for the

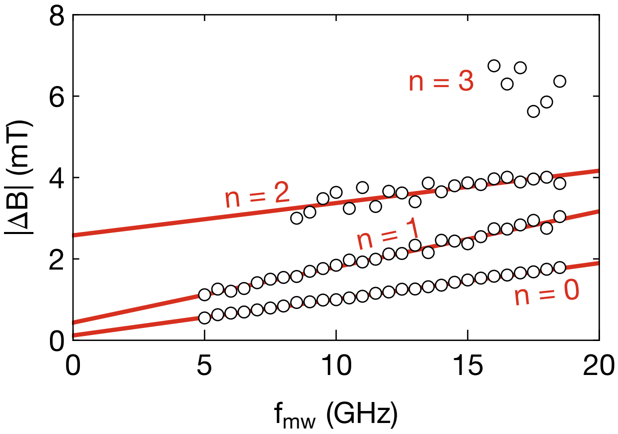

Figure 7.12.: Linewidth (half width at half maximum) as a function of the microwave (resonance) frequency. Solid lines are linear fits to the data.

mode number n	$\alpha(n)$	ΔB_n^0 (mT)
0	0.0025	0.12
1	0.0038	0.43
2	0.0022	2.58

Table 7.1.: Frequency dependent magnetization damping $\alpha(n)$ and inhomogeneous broadening ΔB_n^0 values extracted from a fit to the data in Fig. 7.12.

$n = 0, 1, 2$ mode. The solid lines fitted to the data show that the inhomogeneous broadening ΔB_n^0 in particular rises significantly for larger n. Inhomogeneous broadening is often explained in terms of magnon-magnon-scattering [263–267], which is indeed expected to also depend on the mode number. Details, however, depend on factors such as sample geometry and roughness and prevent a more in depth analysis of the inhomogeneous broadening at this point. The $n = 3$ mode follows the same linewidth trend, however, the data points unfortunately do not permit a meaningful fit to extract $\alpha(3)$ and ΔB_3^0. For the other modes the extracted values are summarized in Tab. 7.1. While the increase in α from the $n = 0$ to the $n = 1$ mode is qualitatively expected as discussed above, the low damping of the $n = 2$ mode is surprising. Quantitatively also the damping figures of the $n = 0$ and $n = 1$ mode behave differently than predicted. With the $\alpha_{\mathrm{SP}}^{n=0}$ calculated above the intrinsic damping of the YIG film as obtained from the fundamental mode is $\alpha_0 = 0.0019$. Correspondingly the total damping of the $n = 1$ mode is expected to take a value of $\alpha(1) = 0.0032$, notably smaller than the measured value. Turning the argument around, the intrinsic damping experienced by the individual modes takes values $\alpha_0^{n=0} = 0.0019$, $\alpha_0^{n=1} = 0.0025$

and $\alpha_0^{n=2} = 0.0009$. These numbers indicate that the intrinsic magnetization damping is not uniform throughout the film. Indeed, each mode samples the intrinsic damping of the film according to its oscillation magnitude profile (Fig. 7.8), which e.g. emphasizes the damping towards the edges of the film in the $n = 1$ mode compared to the $n = 0$ mode. To some extent the measured different damping values then allow to reconstruct the magnetization damping profile in the film. However, since the functions describing the magnitude profiles do not form an orthonormal set, a unique solution can not be inferred. Qualitatively, however, the observations are compatible with a strongly decreased intrinsic magnetization damping at the center ("in the bulk") of the film compared to its edges. This might arise from crystal defects due to lattice mismatch, stoichiometric variations or roughness at the interfaces. Such behavior would, in fact, explain the comparably large magnetization damping figures measured in the films grown at the Walther-Meißner-Institut (*cf.* Ch. 7.1 or e.g. Ref. [99]), which rarely exceed few ten nanometers and thus presumably overemphasize the large damping near the surfaces or interfaces in ferromagnetic resonance studies.

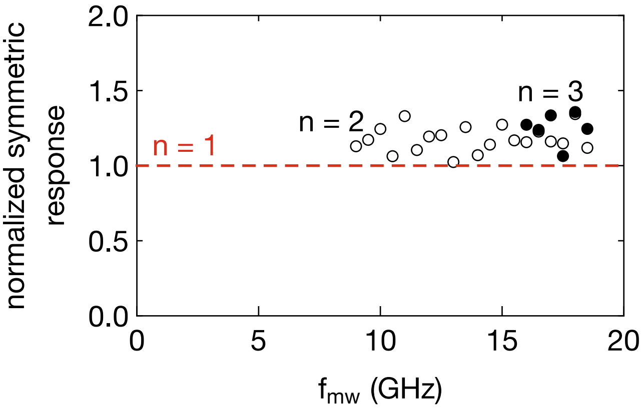

Figure 7.13.: Symmetric peak heights of the $n = 1, 2, 3$ modes, corrected for the different linewidth of the individual modes and normalized to the value of the $n = 1$ mode.

The detailed linewidth information can also be utilized to perform a more elaborate analysis of the peak heights of the $n = 1, 2, 3$ mode. Upon closer inspection of the voltage spectrum in Fig. 7.10 (and the data in Fig. 7.15a) these modes, while indeed featuring very similar peak heights, still slightly decrease in amplitude with larger n. However, to determine the strength of the excitation not only peak heights, but also the individual linewidths have to be considered. An accurate measure of the excitation strength, i.e. the power absorbed by each mode, is given by the area enclosed within

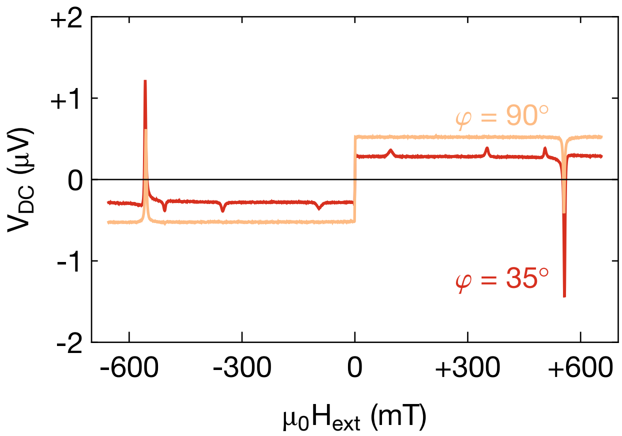

Figure 7.14.: DC voltage recorded at $f_{\mathrm{mw}} = 18\,\mathrm{GHz}$ at angles $\varphi = 35°$ and $90°$ of the external magnetic field.

the (symmetric) Lorentz peak. This requires the peak height to be multiplied with the respective linewidth if different voltage peaks are to be compared. The symmetric response accordingly obtained, normalized to the $V^n_{\mathrm{symm}}\Delta B_n$ value of the $n = 1$ mode, is plotted in Fig. 7.13. The comparison reveals that the values of both the $n = 2$ and $n = 3$ mode are on average about 20% larger than those of the $n = 1$ mode. This implies that the $n = 1$ is also affected by an excitation mechanism different from the spin transfer torque, which diminishes the resonant voltage response. Data and discussion later in this chapter will show that the smaller response value of the $n = 1$ mode can be attributed to a small but notable Oersted field component of the excitation.

To analyze the individual modes in more detail and confirm the assumption of the dominantly spin transfer torque induced origin of the $n = 1,2,3$ mode, voltage spectra have also been taken at different angles φ of the external magnetic field with respect to the microwave charge current in the film plane. Figure 7.6 previously confirmed the angular dependence expected from theory [Eqs. (7.2) and (7.3)] for a 5 nm thick YIG film, in which the spin transfer torque dominates the magnetization excitation, even for the fundamental mode. In the much thicker film here, however, the data show a more complicated behavior as depicted in Fig. 7.14 exemplarily for the two field angles $\varphi = 35°$ and $\varphi = 90°$. While the spin Seebeck contribution is maximized and the higher order modes vanish at $\varphi = 90°$ as expected [Eqs. (6.10), (7.2) and (7.3)], the fundamental mode is still clearly visible, with only a moderate reduction of the peak height. For a more comprehensive analysis spectra like the above are fitted as before, for a series of field angles φ at a constant microwave frequency of $f_{\mathrm{mw}} = 18\,\mathrm{GHz}$. The result for the symmetric and and antisymmetric peak height values is plotted in Figs. 7.15a and 7.15b, respectively.

The full data set for the dependence of the symmetric lineshape

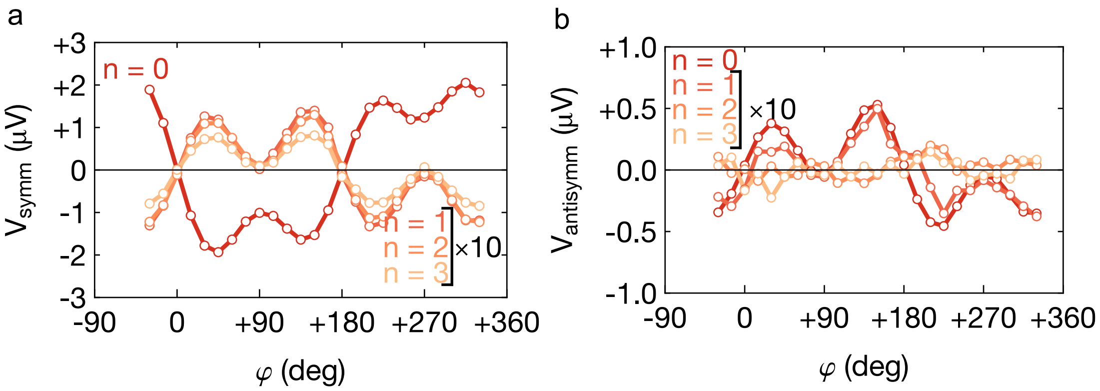

Figure 7.15.: **a** Evolution of the symmetric (**b** antisymmetric) lineshape amplitude as a function of the in-plane field angle φ at $f_{\mathrm{mw}} = 18\,\mathrm{GHz}$. Values for the $n = 1, 2, 3$ mode have been boosted by a factor of 10 for better comparability.

on φ in Fig. 7.15a reinforce the observations made in Fig. 7.14 and show good agreement with the expected $\sin(2\varphi)\cos(\varphi)$ behavior [Eqs. (7.2) and (7.3)] for the $n = 1, 2, 3$ mode but some qualitative deviations for the $n = 0$ mode. Before addressing this point in more detail, it is worth pointing out that the data in Fig. 7.15a also confirm the different polarity of the $n = 0$ compared to the $n = 1, 2, 3$ mode for all configurations of the external magnetic field in the film plane. This is yet another strong indicator of the spin transfer torque driven origin of these modes. Getting back to the $n = 0$ mode the data show that at $\varphi = 90^\circ$ its amplitude only drops to about 60% of its maximum value rather than to vanish as expected from the theory in Ch. 7.1. Additionally, the peak heights for the different maxima are slightly different for the $n = 0$ mode but are about the same for the higher order modes. Before analyzing these findings more exhaustively it is constructive to also investigate the antisymmetric peak heights depicted in Fig. 7.15b. In contrast to the symmetric contribution to the line shape, the antisymmetric contribution of the $n = 0$ mode vanishes at $\varphi = 90^\circ$ as predicted by theory. Once again the maxima show different heights, but it should be noted that the antisymmetric contribution at this frequency is generally small and the observed differences could be a fitting artifact. Interestingly the $n = 1$ mode depends on φ similarly to the $n = 0$ mode, albeit at a much smaller amplitude. The data for the $n = 2, 3$ mode, on the other hand, are essentially flat down to the limit of the noise floor. The latter further strengthens the assumption that these modes are (almost) exclusively of spin transfer torque origin, while the former suggest that also the $n = 1$ mode is still partially affected by the Oersted field. This notion is fully consistent with the smaller (linewidth corrected) voltage signal of the $n = 1$ mode compared to

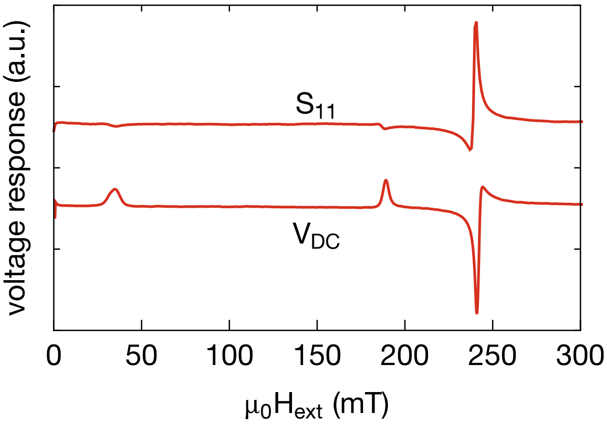

Figure 7.16.: Reflected microwave voltage (S_{11}) and DC voltage recorded at $f_{\mathrm{mw}} = 9\,\mathrm{GHz}$ at an angle $\varphi = 35°$ of the external magnetic field.

the $n = 2$ and $n = 3$ modes in Fig. 7.13.

Further evidence for a partial contamination of also the higher order modes by the Oersted field is provided by a measurement of the reflected microwave power S_{11} in Fig. 7.16. S_{11} assesses the AC rather than the DC voltage response of the sample, but is expected to be dominated by the mutual inductive coupling of the normal metal and the magnet instead of a inverse spin Hall effect mediated spin current signal. The precessing magnetic moments in the magnet induce a (AC) voltage in the normal metal proportional to the total dynamic magnetization of a mode. Due to the principal of reciprocity S_{11} then also quantifies the excitation of the magnetization by the Oersted field. Comparing S_{11} to V_{DC} recorded at the same frequency ($f_{\mathrm{mw}} = 9\,\mathrm{GHz}$) reveals some remarkable difference in the two spectra. Ignoring the line shape and focusing on the magnitude of the voltage peaks it is obvious that the $n = 1$ and $n = 2$ mode are far less efficiently excited than the fundamental mode (and the $n = 2$ mode even less efficient than the $n = 1$ mode). This is yet another indicator that the higher order modes are predominantly spin torque driven. In fact, the AC signal in S_{11} should even overemphasize the Oersted field excitation compared to the DC voltage. This can be motivated by the observation that the dynamic component of the magnetization measured by S_{11} is perpendicular to the equilibrium magnetization orientation, i.e. $S_{11} \propto \sin\Theta$ with the precision cone angle Θ ($\sin\Theta < 1$) [268]. The DC voltage, in contrast, is proportional to the change of the magnetization along the equilibrium orientation axis, i.e. $V_{\mathrm{DC}} \propto \sin^2\Theta$. Note that S_{11} also contains the AC spin pumping voltage contribution of each mode in addition to the inductive coupling. As mentioned above, however, the AC spin pumping voltage signal should be smaller than the voltage due to the inductive coupling, in particular for the $n = 0$ mode.

The fact that also at least the $n = 1$ mode is, if only partially, affected by the Oersted field allows for a number of interpretations. A first possibility is that the Oersted field is far less homogeneous than calculated in Ch. 7.2.1. By a simple estimate based on the peak heights of the $n = 0$ and $n = 1$ mode in the S_{11} measurement, however, the required inhomogeneity is of the order of a few percent or about a factor of 100–1000 larger than calculated in Fig. 7.9, which makes this conclusion somewhat less likely. A second option is that the mode profile deviates from the one depicted in Fig. 7.8. Such a distortion of the mode profile can be caused by surface anisotropy or potentially by the large variation of the intrinsic damping figure throughout the film. Based on the analysis of the resonance frequencies a moderate surface anisotropy appears to be a likely candidate to explain the observed behavior, however, further measurements are required to confirm this assumption.

The unexpected finite signal for $\varphi = 90°$ and the different maxima heights for the fundamental mode have also been observed in Ref. [244] and attributed to a combination of resonant heating and unintentional out of plane magnetic fields, respectively. The data presented above, however, do not fully support these conjectures. The magnitude of the fundamental mode peak at $\varphi = 90°$ would imply resonant heating about as strong as the (non-resonant) Joule heating, which appears excessive. Also, the fact that this effect only occurs for the fundamental mode is not be expected from resonant heating. Most significantly perhaps, at a field angle of $\varphi = 90°$ both (in-plane) Oersted field and spin transfer torque are, to first order, unable to drive the magnetization, which rules out substantial resonant heating in the first place. The out of plane magnetic fields in Ref. [269] cited by Ref. [244] in support of their argument arise from interface effects similar to the spin transfer torque and should thus also affect the higher harmonics. This does not seem not to be the case in the investigated sample here.

Alternatively the Oersted field generated by the microwave charge current might produce a spatially extended out of plane magnetic field. Although the sample geometry (Fig. 7.1) does does not favor such fields orientations, at microwave frequencies current paths can become complicated and produce rather unexpected electric and magnetic field distributions. For an out of plane magnetic field due to high-frequency effects, one would expect to observe an pronounced dependence on the microwave frequency f_{mw}. As shown in Fig. 7.17a, however, the ratio of the symmetric voltage peak height at $\varphi = 90°$ to the symmetric voltage peak height at $\varphi = 35°$ stays relatively constant at a value of about 0.61. There are a few somewhat more pronounced outliers in the data which

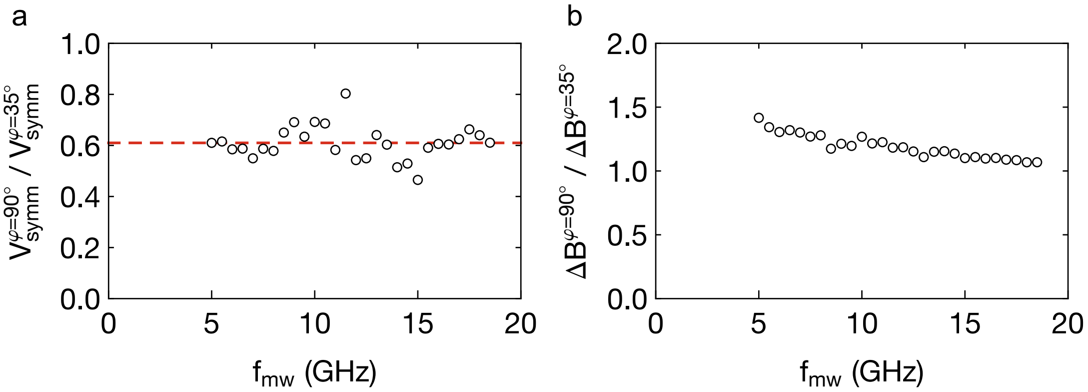

Figure 7.17.: **a** Ratio of the fundamental mode's symmetric voltage peak height at $\varphi = 90^\circ$ to $\varphi = 35^\circ$ as a function of the microwave (resonance) frequency. The dashed line indicates the mean value over all data points. **b** Ratio of the fundamental mode's resonance voltage peak linewidth at $\varphi = 90^\circ$ to $\varphi = 35^\circ$ as a function of the microwave (resonance) frequency.

could indicate resonances in the microwave circuitry, but the data overall appear too flat to support such conjectures. Simultaneously an oddity is observed in the linewidth of the symmetric voltage peaks at $\varphi = 35^\circ$ and $\varphi = 90^\circ$. Comparing again the ratio of the two values in Fig. 7.17b shows that the peak for $\varphi = 90^\circ$ is significantly broader than the one for $\varphi = 35^\circ$ at low frequencies, but approaches the same value for higher frequencies. Analyzed on its own the linewidth at $\varphi = 90^\circ$ yields a total damping of $\alpha(0) = 0.0023$ and an inhomogeneous broadening of $\Delta B_0^0 = 0.39\,\text{mT}$. The different values compared to those extracted in Tab. 7.1 could be caused by magnetocrystalline anisotropy, however, the resonance fields which are typically rather sensitive to anisotropy remain constant for different external magnetic field angles φ.

While interfacial or extended magnetic fields are thus unlikely to be the cause of the finite signal at $\varphi = 90^\circ$ a sizeable, localized out-of-plane magnetic field is generated at the far edges of the film (Fig. 7.9), as noted in Ch. 7.2.1. Although the out-of-plane magnetic fields at the left and right edge of the film are of opposite polarity and thus not able to excite a uniform precession, the width (1.5 mm) of the film far exceeds the exchange length (17 nm) of the film and thus also allows the magnetization to be excited locally. Since the polarity of e.g. the DC spin pumping voltage is determined by the static magnetization component rather than the phase of the precession, these hypothetical spin pumping voltages would add up rather than canceling out. Additionally, the out-of-plane edge fields could also excite the transverse $n = 1, 2, 3, \ldots$ mode that add to the observed DC voltage. The width of the sample here causes the resonance fields of these modes to be largely identical to that of the uniform precession mode. Since higher order modes appear to

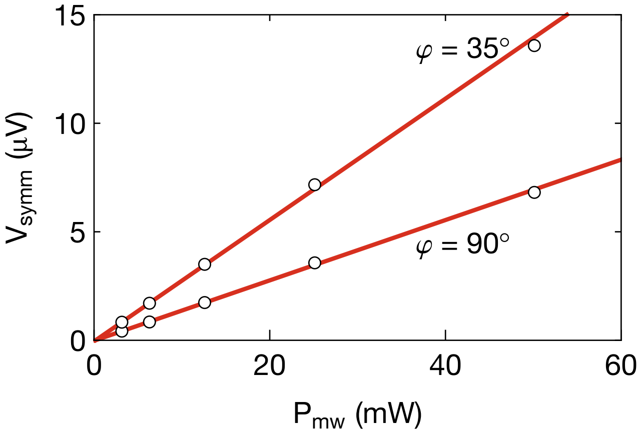

Figure 7.18.: Microwave power dependence of the resonance peak voltages at $f_{\mathrm{mw}} = 5\,\mathrm{GHz}$. Microwave power is given in terms of the value at the microwave source and is reduced by a constant factor at the sample. Solid lines are linear fits to the data.

feature broader resonance lines as discussed above,, this could also explain the increased linewidth of the voltage peak at $\varphi = 90°$. In any case, further theoretical modeling is required to verify if also the rectification generated by such modes is purely symmetrical as observed in the experiment. These modes could even show the resonant heating argued for in Ref. [244], but the voltage signal magnitude observed in the experiment still appears quite a bit too large for this to be plausible.
It is likely that the process that generates the voltages at $\varphi = 90°$ is also present for other values of φ. The effect on the α_0 and ΔB_0^0 values in Tab. 7.1 and the corresponding discussion is, however, small or even negligible. Assuming a variation of the voltage signal at $\varphi = 90°$ as $\sin\varphi$ for symmetry reasons then this signal constitutes about 35% to the total voltage at $\varphi = 35°$. Correcting for this contamination yields $\alpha(0) = 0.0026$ and $\Delta B_0^0 = 0.03\,\mathrm{mT}$ as the *true* damping and inhomogeneous broadening of the fundamental mode, where the former value in particular is almost identical to the value originally extracted.

Another cause for the signal at $\varphi = 90°$ could be parallel pumping [270, 271]. At large driving powers also Oersted fields along the magnetization can drive a precession of the magnetization. Parallel pumping, however, excites modes at half the driving frequency, i.e. at a lower resonance field, which is not compatible with the experimental observations. Additionally, parallel pumping is only possible above a certain microwave power threshold which clearly is not the case for the investigated sample as depicted in Fig. 7.18. The same measurements also confirm the linewidth to be microwave power independent within the margin of the fitting error, ruling out nonlinear effects contaminating the analysis performed above.

7.2.3 *Summary*

The broadband ferromagnetic resonance spectroscopy presented above establishes the spin transfer torque as a convenient tool to study magnetic properties, some of them with spatial resolution, in insulating magnetic thin films. Scaling favorably with the thickness of the investigated specimen [Eq. (7.5)] a number of spin wave modes can be observed of which all but the fundamental mode are dominantly driven by the spin transfer torque. The fact that the spin transfer torque excites all higher order modes equally efficient can be a valuable feature for technological applications, allowing for frequency multiplexing in future spin wave logic devices. In the investigated 105 nm YIG film specifically, four distinct modes can be observed in a frequency window up to 18.5 GHz. As expected, the fundamental mode is driven largely by the microwave magnetic field but shows a dependence on the orientation of applied external magnetic field not covered by present theories. This is in contrast to the data in a much thinner, and thus mainly spin transfer torque driven, YIG film in Ch. 7.1 which behaved according to theory in this respect. The origin of the unexpected angular dependence could not be fully verified, but previous attempts [244] to motivate this feature could be ruled out by the extracted data. Potential candidates are transversely quantized magnetostatic modes or such modes confined to the edges in the YIG film. However, further theoretical modeling and more experiments are required to verify the validity of these assumptions. In light of these findings it appears likely that the phases observed in Ch. 7.1 originate from similar features. This would affect the quantitative decomposition of the DC voltages performed in that chapter to some extent, but should not qualitatively affect the findings. This is particularly true for the thinnest film where Oersted fields can largely be ignored.

The higher order modes observed in the 105 nm thick YIG film are qualitatively compatible with theory and are found to be predominantly excited by the spin transfer torque, with only a faint coupling to the Oersted field. Combining the resonance field data of all modes allows to extract values for the saturation magnetization and the exchange constant of the film. A moderately strong surface anisotropy appears to be present in the sample, however, an exact determination is unfortunately not possible at this point. The linewidth and resulting magnetization damping figures imply a significant variation of the intrinsic magnetization damping across the film, with the value at the edges much larger than in its center.

Further studies could find valuable information in experiments going beyond in plane external magnetic fields and should focus on systematically studying the resonances with the external magnetic field applied along arbitrary (out of plane) directions to fully characterize the evolution of the lineshape.
It would also be worthwhile to investigate the simultaneous excitation of several modes at different frequencies to explore a potential coupling between the modes and how, if at all, it affects the resonance linewidths.
Another interesting aspect is the use of the mostly spin torque actuated modes for the demonstration of AC spin pumping. The AC spin pumping experiments performed so far [245–247] suffer from inductive coupling between the sample magnetization and the voltage signals measured in the Pt layers. These inductive signals require elaborate methods to be eliminated from the signals of interest. This coupling should be far less of an issue for the purely spin torque actuated higher order modes in magnetic insulators and could be used both for the demonstration of AC spin pumping on magnetic insulators in the first place, but also to verify some of the more unusual interpretations [247] of the existing data.

8

REVIEW

This thesis covered some of the most relevant spin current based phenomena in normal metal/magnet thin film structures. The obtained experimental results provide important insights into the effect of a spin transfer torque exerted by one of the two materials and the respective other. Significant contributions have also been made to the experimental state-of-the-art with new measurement techniques. Moreover, the long-standing issue regarding the sign of the spin Hall angle has been resolved. In the following the key results presented in this thesis are summarized and reviewed, before concluding with some final remarks.

Chapter 4 is not so much concerned with investigating any specific features of spin current based phenomena but rather with establishing a new measurement method that drastically speeds up measurements while simultaneously improving the robustness of the measurement with respect to external perturbations. This is achieved by shifting measurement and analysis from a purely static approach, where a DC signal is averaged for a constant magnetic field direction, to a dynamic scheme, where the field direction is rotated and the time-varying signal is averaged over many field rotations. Employing a continuously rotating magnetic field and subsequent Fourier analysis the angular dependence featured by most spin current based effects can be resolved at much greater speed than using the conventional approach with static magnetic fields. Towards this end a device based on a continuously rotating permanent magnet system was conceived and implemented. The results show that the spin Hall magnetoresistance can be measured by approximately an order of magnitude (or even more) faster compared to measurements based on static magnetic fields, while maintaining a very similar degree of precision, even under much less ideal ambient conditions. While not demonstrated experimentally, it is also outlined how other phenomena, such as spin pumping or the spin Seebeck effect, could be measured using the same device.

Chapter 5 covers the research performed towards a better understanding of the spin Seebeck effect. In Ch. 5.1 the established

two-temperature-model is extended and adopted to perform analytical and numerical calculations of the coupled temperature distributions of phonons, electrons and magnons in normal metal/magnet thin film structures on the nanometer scale. The two central results are that phonons and most magnons equilibrate over much shorter distances than previously estimated in yttrium iron garnet (Fig. 5.4) and that the coupling of the magnons in the yttrium iron garnet, via the spin transfer torque, with the electrons in the Pt significantly influences the magnon temperature distribution (Fig. 5.3). These findings are supported by a comparison with experiments. The quantitative analysis of the experimental data in terms of a nonequlibrium state at the normal metal/magnet interface which is described by an effective two-temperature model should, however, be regarded as a first approximation only, as indicated by the findings in Ch. 5.2 and the results presented by others in the literature.
Chapter 5.2 presents an experimental study of the transient behavior of the spin Seebeck effect in yttrium iron garnet films of varying thicknesses. Using amplitude modulated heating, the transfer functions, i.e. the evolution of the measured voltage magnitude as a function of frequency, are mapped out and analyzed. The transfer functions show an attenuation of the spin Seebeck voltage with increasing the modulation frequency. Moreover, the degree of this decrease and the shape of the transfer functions depend on the yttrium iron garnet film thickness. Based on a survey of both theoretical and experimental reports the data are interpreted in terms of a dependence of the magnon spectrum on the thickness of the yttrium iron garnet films. The interpretation allows to combine the aforementioned theoretical and experimental results and draws a consistent picture of some of the microscopic processes in (insulating) magnets under a spatially varying temperature bias.
The experimental technique presented in Ch. 5.3 is meant to simplify spin Seebeck measurements and, as an added benefit, allows integration into many preexisting setups. Instead of using some external means to apply temperature gradients to the normal metal/magnet samples used in all experiments, the Pt detector layer is used as an integrated resistive heater. Exploiting the symmetry properties of the resistive heating and spin Seebeck effect, the latter can be recovered even in the presence of much larger background voltage signals. The technique has already found widespread adoption in the community and allowed the measurements at large external magnetic field strengths and at low temperatures presented in this thesis.

Chapter 6 presents a collaborative work with the aim of resolving conflicting reports on the sign of perhaps the central quantity in spin current based research: the spin Hall angle. A theoretical toy model is developed that links the spin Hall angle to scattering at charged impurities and, using careful bookkeeping of all signs involved, an experimental guideline is given to determine the *absolute* sign of the spin Hall angle.

Finally, Ch. 7 shows the experimental verification of spin transfer torque induced, resonant magnetization dynamics in a magnetic insulator. A detailed analysis of the DC voltage arising under an AC current bias in yttrium iron garnet/platinum thin film samples revealed the efficient excitation of resonant magnetization precession by the spin transfer torque. This study was made possible by comparing samples with varying yttrium iron garnet and platinum layer thickness with a theoretical model. The results represent the first demonstration that the spin transfer torque also allows to resonantly excite magnetization dynamics in insulating magnetic materials and should stimulate further research in this direction.
The second part of the chapter (Ch. 7.2) extends the experiments to the broadband investigation of perpendicular standing spin waves in the same material. The demonstrated excitation and detailed analysis of several spin wave modes in a yttrium iron garnet thin film not only reaffirm the findings in the first part of the chapter but allows a much more in depth examination of the magnetic properties of insulating magnetic thin films. In particular the spatial evolution of the magnetization damping across the film can be inferred (Tab. 7.1 and corresponding discussion) and a voltage signal unforseen by the theoretical modeling is explored exhaustively (Figs. 7.14, 7.15, 7.17 and 7.18).
The simultaneous occurrence of all relevant spin related phenomena demonstrated in these experiments emphasizes the importance of the research for technological applications, even for devices built around only one of the spin effects covered herein.

Despite the multitude of results presented here, an in-depth understanding of spin transfer torque mediated phenomena has not yet been achieved. One should expect many more insights in the years to come, which will hopefully have benefited from the developments put forward in this thesis.

A

APPENDIX

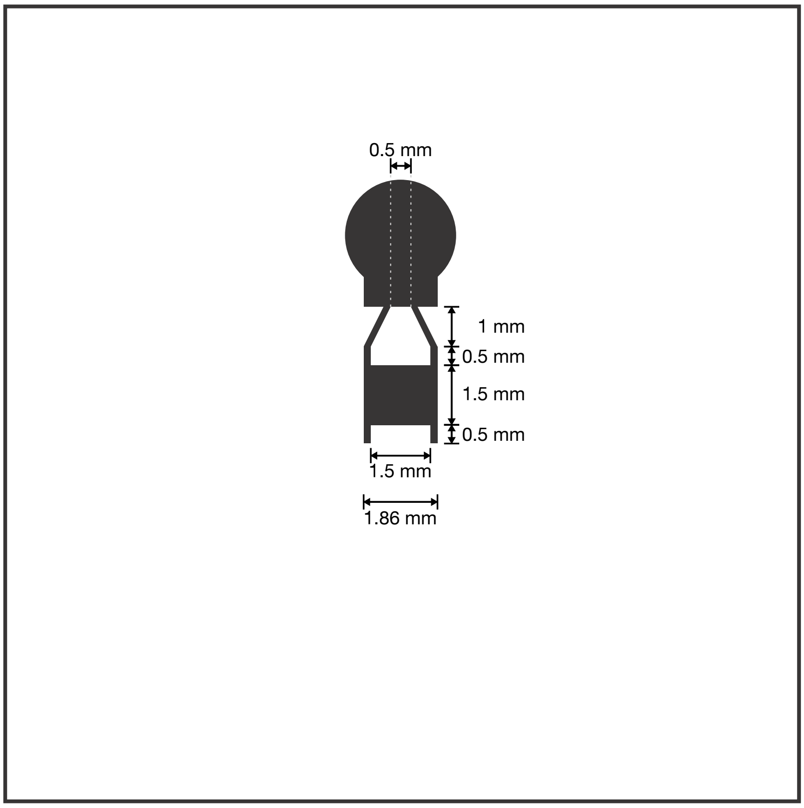

Figure A.1.: Annotated version of the mask used for the fabrication of the coplanar waveguides in the spin torque resonance experiments in Ch. 7. The circular shape is a standard mini-SMP footprint. Design by Johannes Lotze.

PUBLICATIONS

The following publications were prepared during the course of the doctoral studies, some of which served as template for text and figures in this thesis:

1. **Quantitative study of the spin Hall magnetoresistance in ferromagnetic insulator/normal metal hybrids**
   M. Althammer, S. Meyer, H. Nakayama, *M. Schreier*, S. Altmannshofer, M. Weiler, H. Huebl, S. Geprägs, M. Opel, R. Gross, D. Meier, C. Klewe, T. Kuschel, J.-M. Schmalhorst, G. Reiss, L. Shen, A. Gupta, Y.-T. Chen, G. E. W. Bauer, E. Saitoh, S. T. B. Goennenwein
   Phys. Rev. B **87**, 224401 (2013)
   Selected as "Editor's Suggestion" by the journal
2. **Magnon, phonon, and electron temperature profiles and the spin Seebeck effect in magnetic insulator/normal metal hybrid structures**
   M. Schreier, A. Kamra, M. Weiler, J. Xiao, G. E. W. Bauer, R. Gross, S. T. B. Goennenwein
   Phys. Rev. B **88**, 094410 (2013)
3. **Experimental test of the spin mixing interface conductivity concept**
   M. Weiler, M. Althammer, *M. Schreier*, J. Lotze, M. Pernpeintner, S. Meyer, H. Huebl, R. Gross, A. Kamra, J. Xiao, Y.-T. Chen, H. Jiao, G. E. W. Bauer, S. T. B. Goennenwein
   Phys. Rev. Lett. **111**, 176601 (2013)
   Selected as "Editor's Suggestion" by the journal
4. **Current heating induced spin Seebeck effect**
   M. Schreier, N. Roschewsky, E. Dobler, S. Meyer, H. Huebl, R. Gross, S. T. B. Goennenwein
   Appl. Phys. Lett. **103**, 242404 (2013)
5. **Theoretical model for torque differential magnetometry of single domain magnets**
   A. Kamra, *M. Schreier*, H. Huebl, S. T. B. Goennenwein
   Phys. Rev. B **89**, 184406 (2014)
6. **Time resolved spin Seebeck experiments**
   N. Roschewsky, *M. Schreier*, A. Kamra, F. Schade, K. Ganzhorn, S. Meyer, H. Huebl, S. Geprägs, R. Gross, S. T. B. Goennenwein
   Appl. Phys. Lett. **104**, 202410 (2014)

7. **Sign of inverse spin Hall voltages generated by ferromagnetic resonance and temperature gradients in yttrium iron garnet platinum bilayers**
   M. Schreier, G. E. W. Bauer, V. Vasyuchka, J. Flipse, K. Uchida, J. Lotze, V. Lauer, A. Chumak, A. Serga, S. Daimon, T. Kikkawa, E. Saitoh, B. J. van Wees, B. Hillebrands, R. Gross, S. T. B. Goennenwein
   J. Phys. D: Appl. Phys. **48**, 025001 (2015)
   Selected as "Highlight" by the journal

8. **Current-induced spin torque resonance of magnetic insulators affected by field-like spin-orbit torques and out-of-plane magnetizations**
   T. Chiba, *M. Schreier*, G. E. W. Bauer, S. Takahashi
   J. Appl. Phys. **117**, 17C715 (2015)

9. **Longitudinal spin Seebeck effect contribution in transverse spin Seebeck effect experiments in Pt/YIG and Pt/NFO**
   D. Meier, D. Reinhardt, M. van Straaten, C. Klewe, M. Althammer, *M. Schreier*, S. T. B. Goennenwein, A. Gupta, M. Schmid, C. H. Back, J.-M. Schmalhorst, T. Kuschel, G. Reiss
   Nat. Comm. **6**, 8211 (2015)

10. **An all-electrical torque differential magnetometer operating under ambient conditions**
    A. Kamra, S. von Hoesslin, N. Roschewsky, J. Lotze, *M. Schreier*, R. Gross, S. T. B. Goennenwein, H. Huebl
    Eur. Phys. J. B (2015) **88**: 224

11. **Current-induced spin torque resonance of a magnetic insulator**
    M. Schreier, T. Chiba, A. Niedermayr, J. Lotze, H. Huebl, S. Geprägs, S. Takahashi, G. E. W. Bauer, R. Gross, S. T. B. Goennenwein
    Phys. Rev. B **92**, 144411 (2015)

12. **Antiferromagnetic resonance detected by direct current voltages in MnF_2/Pt bilayers**
    P. Ross, *M. Schreier*, J. Lotze, H. Huebl, R. Gross, S. T. B. Goennenwein
    J. Appl. Phys. **118**, 233907 (2015)

13. **Spin Seebeck effect at microwave frequencies**
    M. Schreier, F. Kramer, H. Huebl, S. Geprägs, R. Gross, S. T. B. Goennenwein
    T. Noack, T. Langner, A. A. Serga, B. Hillebrands, V. I. Vasyuchka
    submitted for publication

BIBLIOGRAPHY

[1] B. Steves, M. Hendry, and A. Cameron, *Extra-Solar Planets: The Detection, Formation, Evolution and Dynamics of Planetary Systems*, Scottish Graduate Series (CRC Press, 2010).

[2] P. Kustaanheimo, in *Mathematische Methoden der Himmelsmechanik und Astronautik: Bericht einer Tagung des Mathematischen Forschungsinstituts Oberwolfach, 15. - 21. März 1964* (1964) pp. 330–340.

[3] P. Kustaanheimo and E. Stiefel, *Journal für die reine und angewandte Mathematik (Crelles Journal)*, J. Reine Angew. Math. **218**, 204 (1965).

[4] E. Stiefel and G. Scheifele, *Linear and regular celestial mechanics: perturbed two-body motion, numerical methods, canonical theory*, Grundlehren der mathematischen Wissenschaften (Springer-Verlag, 1971).

[5] J. Binney and S. Tremaine, *Galactic Dynamics: (Second Edition)*, Princeton Series in Astrophysics (Princeton University Press, 2011).

[6] P. Saha, Mon. Not. R. Astron. Soc. **400**, 228 (2009).

[7] E. Fermi, Phys. Rev. **75**, 1169 (1949).

[8] A. Schlüter and L. Biermann, Z. Naturforsch. **5a**, 237 (1950).

[9] Y. Tserkovnyak, A. Brataas, and G. E. W. Bauer, Phys. Rev. Lett. **88**, 117601 (2002).

[10] K. Uchida, H. Adachi, T. Ota, H. Nakayama, S. Maekawa, and E. Saitoh, Appl. Phys. Lett. **97**, 172505 (2010).

[11] H. Nakayama, M. Althammer, Y.-T. Chen, K. Uchida, Y. Kajiwara, D. Kikuchi, T. Ohtani, S. Geprägs, M. Opel, S. Takahashi, R. Gross, G. E. W. Bauer, S. T. B. Goennenwein, and E. Saitoh, Phys. Rev. Lett. **110**, 206601 (2013).

[12] J. Xiao, G. E. W. Bauer, K. Uchida, E. Saitoh, and S. Maekawa, Phys. Rev. B **81**, 214418 (2010); J. Xiao, G. E. W. Bauer, K. Uchida, E. Saitoh, and S. Maekawa, Phys. Rev. B **82**, 099904 (2010).

[13] Q. Sun, H. Guo, and J. Wang, Phys. Rev. B **69**, 054409 (2004).

[14] A. Fournier, G. Bergmann, and R. S. Thompson, Phys. Rev. B **75**, 233101 (2007).

[15] M. Schreier, A. Kamra, M. Weiler, J. Xiao, G. E. W. Bauer, R. Gross, and S. T. B. Goennenwein, Phys. Rev. B **88**, 094410 (2013).

[16] M. Schreier, N. Roschewsky, E. Dobler, S. Meyer, H. Huebl, R. Gross, and S. T. B. Goennenwein, Appl. Phys. Lett. **103**, 242404 (2013).

[17] M. Schreier, G. E. W. Bauer, V. I. Vasyuchka, J. Flipse, K. Uchida, J. Lotze, V. Lauer, A. V. Chumak, A. A. Serga, S. Daimon, T. Kikkawa, E. Saitoh, B. J. van Wees, B. Hillebrands, R. Gross, and S. T. B. Goennenwein, J. Phys. D: Appl. Phys. **48**, 025001 (2015).

[18] M. Schreier, T. Chiba, A. Niedermayr, J. Lotze, H. Huebl, S. Geprägs, S. Takahashi, G. E. W. Bauer, R. Gross, and S. T. B. Goennenwein, Phys. Rev. B **92**, 144411 (2015).

[19] W. Gerlach and O. Stern, Z Phys A - Hadron Nucl **9**, 353 (1922).

[20] W. Gerlach and O. Stern, Z Phys **9**, 349 (1922).

[21] P. Zeeman, Nature **55**, 347 (1897).

[22] V. Cherepanov, I. Kolokolov, and V. L'vov, Phys. Rep. **229**, 81 (1993).

[23] T. Holstein and H. Primakoff, Phys. Rev. **58**, 1098 (1940).

[24] L. P. Kadanoff and P. C. Martin, Ann. Phys. **24**, 419 (1963).

[25] H. S. Bennett and P. C. Martin, Phys. Rev. **138**, A608 (1965).

[26] I. J. Lowe and S. Gade, Phys. Rev. **156**, 817 (1967).

[27] M. A. Khasawneh, C. Klose, W. P. Pratt, and N. O. Birge, Phys. Rev. B **84**, 014425 (2011).

[28] H. Jiao and G. E. W. Bauer, Phys. Rev. Lett. **110**, 217602 (2013).

[29] P. C. van Son, H. van Kempen, and P. Wyder, Phys. Rev. Lett. **58**, 2271 (1987).

[30] M. I. D'yakonov and V. I. Perel', JETP Lett. **13**, 467 (1971).

[31] J. E. Hirsch, Phys. Rev. Lett. **83**, 1834 (1999).

[32] Y. K. Kato, R. C. Myers, A. C. Gossard, and D. D. Awschalom, Science **306**, 1910 (2004).

[33] J. Sinova, S. O. Valenzuela, J. Wunderlich, C. H. Back, and T. Jungwirth, Rev. Mod. Phys. **87**, 1213 (2015).

[34] S. Singh, M. Anguera, E. del Barco, R. Springell, and C. W. Miller, Appl. Phys. Lett. **107**, 232403 (2015).

[35] J. C. Slonczewski, Phys. Rev. B **39**, 6995 (1989).

[36] J. Slonczewski, J. Magn. Magn. Mater. **159**, L1 (1996).

[37] L. Berger, Phys. Rev. B **54**, 9353 (1996).

[38] A. Brataas, Y. V. Nazarov, and G. E. W. Bauer, Phys. Rev. Lett. **84**, 2481 (2000).

[39] D. Ralph and M. Stiles, J. Magn. Magn. Mater. **320**, 1190 (2008).

[40] A. Brataas, Y. Tserkovnyak, G. E. W. Bauer, and P. Kelly, in *Spin Current*, Oxford science publications, edited by S. Maekawa, S. Valenzuela, E. Saitoh, and T. Kimura (OUP Oxford, 2012).

[41] A. F. Andreev, Sov. Phys. JETP. **19**, 1823 (1964).

[42] M. Johnson and R. H. Silsbee, Phys. Rev. Lett. **55**, 1790 (1985).

[43] M. Johnson and R. H. Silsbee, Phys. Rev. B **37**, 5312 (1988).

[44] X. Jia, K. Liu, K. Xia, and G. E. W. Bauer, EPL (Europhysics Letters) **96**, 17005 (2011).

[45] X. Waintal, E. B. Myers, P. W. Brouwer, and D. C. Ralph, Phys. Rev. B **62**, 12317 (2000).

[46] P. M. Haney, H.-W. Lee, K.-J. Lee, A. Manchon, and M. D. Stiles, Phys. Rev. B **87**, 174411 (2013).

[47] Y.-T. Chen, S. Takahashi, H. Nakayama, M. Althammer, S. T. B. Goennenwein, E. Saitoh, and G. E. W. Bauer, Phys. Rev. B **87**, 144411 (2013).

[48] M. Althammer, S. Meyer, H. Nakayama, M. Schreier, S. Altmannshofer, M. Weiler, H. Huebl, S. Geprägs, M. Opel, R. Gross, D. Meier, C. Klewe, T. Kuschel, J.-M. Schmalhorst, G. Reiss, L. Shen, A. Gupta, Y.-T. Chen, G. E. W. Bauer, E. Saitoh, and S. T. B. Goennenwein, Phys. Rev. B **87**, 224401 (2013).

[49] T. Gilbert, Phys. Rev. **100**, 1243 (1955).

[50] T. Gilbert, IEEE Trans. Magn. **40**, 3443 (2004).

[51] C. Kittel, Phys. Rev. **73**, 155 (1948).

[52] R. H. Silsbee, A. Janossy, and P. Monod, Phys. Rev. B **19**, 4382 (1979).

[53] E. Saitoh, M. Ueda, H. Miyajima, and G. Tatara, Appl. Phys. Lett. **88**, 182509 (2006).

[54] M. V. Costache, M. Sladkov, S. M. Watts, C. H. van der Wal, and B. J. van Wees, Phys. Rev. Lett. **97**, 216603 (2006).

[55] M. V. Costache, S. M. Watts, C. H. van der Wal, and B. J. van Wees, Phys. Rev. B **78**, 064423 (2008).

[56] O. Mosendz, V. Vlaminck, J. E. Pearson, F. Y. Fradin, G. E. W. Bauer, S. D. Bader, and A. Hoffmann, Phys. Rev. B **82**, 214403 (2010).

[57] O. Mosendz, J. E. Pearson, F. Y. Fradin, G. E. W. Bauer, S. D. Bader, and A. Hoffmann, Phys. Rev. Lett. **104**, 046601 (2010).

[58] F. D. Czeschka, L. Dreher, M. S. Brandt, M. Weiler, M. Althammer, I.-M. Imort, G. Reiss, A. Thomas, W. Schoch, W. Limmer, H. Huebl, R. Gross, and S. T. B. Goennenwein, Phys. Rev. Lett. **107**, 046601 (2011).

[59] B. Heinrich, C. Burrowes, E. Montoya, B. Kardasz, E. Girt, Y.-Y. Song, Y. Sun, and M. Wu, Phys. Rev. Lett. **107**, 066604 (2011).

[60] Y. Shiomi and E. Saitoh, Phys. Rev. Lett. **113**, 266602 (2014).

[61] T. J. Seebeck, Abhandlungen der Königlichen Preußischen Akademie der Wissenschaften zu Berlin , 265 (1823).

[62] H. Adachi, J. Ohe, S. Takahashi, and S. Maekawa, Phys. Rev. B **83**, 094410 (2011).

[63] S. S.-L. Zhang and S. Zhang, Phys. Rev. B **86**, 214424 (2012).

[64] S. Hoffman, K. Sato, and Y. Tserkovnyak, Phys. Rev. B **88**, 064408 (2013).

[65] H. Adachi, K. Uchida, E. Saitoh, and S. Maekawa, Rep. Prog. Phys. **76**, 036501 (2013).

[66] K. S. Tikhonov, J. Sinova, and A. M. Finkel'stein, Nat Commun **4**, (2013).

[67] L. Chotorlishvili, Z. Toklikishvili, V. K. Dugaev, J. Barnaś, S. Trimper, and J. Berakdar, Phys. Rev. B **88**, 144429 (2013).

[68] U. Ritzmann, D. Hinzke, and U. Nowak, Phys. Rev. B **89**, 024409 (2014).

[69] S. R. Etesami, L. Chotorlishvili, and J. Berakdar, Appl. Phys. Lett. **107**, 132402 (2015).

[70] K. Uchida, T. Kikkawa, A. Miura, J. Shiomi, and E. Saitoh, Phys. Rev. X **4**, 041023 (2014).

[71] S. Geprägs, A. Kehlberger, F. D. Coletta, Z. Qiu, E. Guo, T. Schulz, C. Mix, S. Meyer, A. Kamra, M. Althammer, H. Huebl, G. Jakob, Y. Ohnuma, H. Adachi, J. Barker, S. Maekawa, G. E. W. Bauer, E. Saitoh, R. Gross, S. T. B. Goennenwein, and M. Kläui, Nat Commun **7**, (2016).

[72] S. R. Boona and J. P. Heremans, Phys. Rev. B **90**, 064421 (2014).

[73] K. Uchida, S. Takahashi, K. Harii, J. Ieda, W. Koshibae, K. Ando, S. Maekawa, and E. Saitoh, Nature **455**, 778 (2008).

[74] K. Uchida, J. Xiao, H. Adachi, J. Ohe, S. Takahashi, J. Ieda, T. Ota, Y. Kajiwara, H. Umezawa, H. Kawai, G. E. W. Bauer, S. Maekawa, and E. Saitoh, Nat. Mater. **9**, 894 (2010).

[75] A. Kehlberger, U. Ritzmann, D. Hinzke, E.-J. Guo, J. Cramer, G. Jakob, M. C. Onbasli, D. H. Kim, C. A. Ross, M. B. Jungfleisch, B. Hillebrands, U. Nowak, and M. Kläui, Phys. Rev. Lett. **115**, 096602 (2015).

[76] L. J. Cornelissen, J. Liu, R. A. Duine, J. B. Youssef, and B. J. van Wees, Nat Phys **11**, 1022 (2015).

[77] S. T. B. Goennenwein, R. Schlitz, M. Pernpeintner, K. Ganzhorn, M. Althammer, R. Gross, and H. Huebl, Appl. Phys. Lett. **107**, 172405 (2015).

[78] D. Meier, D. Reinhardt, M. van Straaten, C. Klewe, M. Althammer, M. Schreier, S. T. B. Goennenwein, A. Gupta, M. Schmid, C. H. Back, J.-M. Schmalhorst, T. Kuschel, and G. Reiss, Nat Commun **6**, (2015).

[79] S. Y. Huang, X. Fan, D. Qu, Y. P. Chen, W. G. Wang, J. Wu, T. Y. Chen, J. Q. Xiao, and C. L. Chien, Phys. Rev. Lett. **109**, 107204 (2012).

[80] D. Qu, S. Y. Huang, J. Hu, R. Wu, and C. L. Chien, Phys. Rev. Lett. **110**, 067206 (2013).

[81] S. Geprägs, S. Meyer, S. Altmannshofer, M. Opel, F. Wilhelm, A. Rogalev, R. Gross, and S. T. B. Goennenwein, Appl. Phys. Lett. **101**, 262407 (2012); S. Geprägs, S. T. B. Goennenwein, M. Schneider, F. Wilhelm, K. Ollefs, A. Rogalev, M. Opel, and R. Gross, ArXiv e-prints (2013), arXiv:1307.4869 .

[82] T. Kikkawa, K. Uchida, Y. Shiomi, Z. Qiu, D. Hou, D. Tian, H. Nakayama, X.-F. Jin, and E. Saitoh, Phys. Rev. Lett. **110**, 067207 (2013).

[83] F. Bertaut and F. Forrat, C. R. Acad. Sci. **242**, 382 (1956).

[84] S. Geller and M. A. Gilleo, Acta Cryst. **10**, 239 (1957).

[85] M. N. Baibich, J. M. Broto, A. Fert, F. N. Van Dau, F. Petroff, P. Etienne, G. Creuzet, A. Friederich, and J. Chazelas, Phys. Rev. Lett. **61**, 2472 (1988).

[86] G. Binasch, P. Grünberg, F. Saurenbach, and W. Zinn, Phys. Rev. B **39**, 4828 (1989).

[87] Persistence of Vision Pty. Ltd., "Persistence of vision raytracer (version 3.7)," `http://www.povray.org/` (2004).

[88] LILYsoft, "Spectral rendering with pov-ray," `http://www.lilysoft.org/` (2012).

[89] Abdel Samad, B., Blanc-Mignon, M.-F., Roumie, M., Siblini, A., Chatelon, J. P., and Korek, M., Eur. Phys. J. Appl. Phys. **50**, 10502 (2010).

[90] L. Surhone, M. Timpledon, and S. Marseken, *Yttrium Iron Garnet* (VDM Publishing, 2010).

[91] G. B. Scott, D. E. Lacklison, and J. L. Page, Phys. Rev. B **10**, 971 (1974).

[92] G. B. Scott and J. L. Page, Phys. Status Solidi B **79**, 203 (1977).

[93] A. Sposito, T. C. May-Smith, G. B. G. Stenning, P. A. J. de Groot, and R. W. Eason, Opt. Mater. Express **3**, 624 (2013).

[94] H. Serier-Brault, L. Thibault, M. Legrain, P. Deniard, X. Rocquefelte, P. Leone, J.-L. Perillon, S. L. Bris, J. Waku, and S. Jobic, Inorg. Chem. **53**, 12378 (2014).

[95] B. P. Richards and A. C. Greenham, J. Phys. D: Appl. Phys. **1**, 1297 (1968).

[96] S. H. Wemple, S. L. Blank, J. A. Seman, and W. A. Biolsi, Phys. Rev. B **9**, 2134 (1974).

[97] E. E. Anderson, Phys. Rev. **134**, A1581 (1964).

[98] T. Kasuya and R. C. LeCraw, Phys. Rev. Lett. **6**, 223 (1961).

[99] M. Althammer, *Spin-transport-phenomena in metals, semiconductors, and insulators*, Ph.D. thesis, Technische Universität München (2012).

[100] S. Altmannshofer, *Epitaxie und Charakterisierung von dünnen Schichten des ferromagnetischen Isolators* $Y_3Fe_5O_{12}$, Master's thesis, Hochschule für angewandte Wissenschaften München (2012).

[101] S. Meyer, *Spin Caloritronics in ferromagnet/normal metal hybrid systems*, Ph.D. thesis, Technische Universität München (2015).

[102] D. Lide, *CRC Handbook of Chemistry and Physics, 89th Edition* (Taylor & Francis, 2008).

[103] M. Cardona, in *Proceedings of the International Conference on the Physics of Semiconductors* (1968) p. 365.

[104] M. Cardona, *Modulation spectroscopy*, Solid state physics: Supplement (Academic Press, 1969).

[105] M. Faraday, in *Philosophical Transactions of the Royal Society of London: Giving Some Accounts of the Present Undertakings, Studies, and Labours, of the Ingenious, in Many Considerable Parts of the World, Vol. 122*, edited by The Royal Society, London (1832).

[106] K. Halbach, Nucl. Instr. Meth. **169**, 1 (1980).

[107] J. Mallinson, IEEE Trans. Magn. **9**, 678 (1973).

[108] J. Coey, J. Magn. Magn. Mater. **248**, 441 (2002).

[109] F. Bloch, O. Cugat, G. Meunier, and J. Toussaint, IEEE Trans. Magn. **34**, 2465 (1998).

[110] M. Kumada, Y. Iwashita, M. Aoki, and E. Sugiyama, in *Particle Accelerator Conference, 2003. PAC 2003. Proceedings of the*, Vol. 3 (2003) pp. 1993–1995 vol.3.

[111] M. Weiler, *Magnon-Phonon Interactions in Ferromagnetic Thin Films*, Ph.D. thesis, Technische Universität München (2012).

[112] A. v. Ettingshausen and W. Nernst, Ann. Phys. **265**, 343 (1886).

[113] M. Johnson and R. H. Silsbee, Phys. Rev. B **35**, 4959 (1987).

[114] A. Slachter, F. L. Bakker, J.-P. Adam, and B. J. van Wees, Nat Phys **6**, 879 (2010).

[115] J. Flipse, L. F. Bakker, A. Slachter, K. F. Dejene, and B. J. van Wees, Nat Nano **7**, 166 (2012).

[116] G. E. W. Bauer, E. Saitoh, and B. J. van Wees, Nat. Mater. **11**, 391 (2012).

[117] K. Uchida, T. Nonaka, T. Ota, and E. Saitoh, Appl. Phys. Lett. **97**, 262504 (2010).

[118] M. Weiler, M. Althammer, F. D. Czeschka, H. Huebl, M. S. Wagner, M. Opel, I.-M. Imort, G. Reiss, A. Thomas, R. Gross, and S. T. B. Goennenwein, Phys. Rev. Lett. **108**, 106602 (2012).

[119] D. Meier, T. Kuschel, L. Shen, A. Gupta, T. Kikkawa, K. Uchida, E. Saitoh, J.-M. Schmalhorst, and G. Reiss, Phys. Rev. B **87**, 054421 (2013).

[120] T. Kikkawa, K. Uchida, S. Daimon, Z. Qiu, Y. Shiomi, and E. Saitoh, Phys. Rev. B **92**, 064413 (2015).

[121] H. Jin, S. R. Boona, Z. Yang, R. C. Myers, and J. P. Heremans, Phys. Rev. B **92**, 054436 (2015).

[122] M. Agrawal, V. I. Vasyuchka, A. A. Serga, A. D. Karenowska, G. A. Melkov, and B. Hillebrands, Phys. Rev. Lett. **111**, 107204 (2013).

[123] P. L. Kapitza, Journal of Physics **4**, 181 (1941).

[124] D. J. Sanders and D. Walton, Phys. Rev. B **15**, 1489 (1977).

[125] S. S. Shinozaki, Phys. Rev. **122**, 388 (1961).

[126] S. Klingler, A. Chumak, T. Mewes, B. Khodadadi, C. Mewes, C. Dubs, O. Surzhenko, B. Hillebrands, and A. Conca, J. Phys. D: Appl. Phys. **48**, 015001 (2015).

[127] A. Brataas, Y. Tserkovnyak, G. E. W. Bauer, and B. I. Halperin, Phys. Rev. B **66**, 060404 (2002).

[128] J. Fourier, *Théorie analytique de la chaleur* (Chez Firmin Didot, père et fils, 1822).

[129] M. Reichling and H. Gronbeck, J. Appl. Phys. **75**, 1914 (1994).

[130] D. Keith Roper, W. Ahn, and M. Hoepfner, J Phys Chem C **111**, 3636 (2007).

[131] N. Kumar and K. Sinha, Physica **36**, 655 (1967).

[132] A. P. Caffrey, P. E. Hopkins, J. M. Klopf, and P. M. Norris, Microscale Thermophysical Engineering **9**, 365 (2005).

[133] Z. Lin, L. V. Zhigilei, and V. Celli, Phys. Rev. B **77**, 075133 (2008).

[134] M. I. Kaganov, I. M. Lifshitz, and L. V. Tanatarov, Sov. Phys. JETP **4**, 173 (1957).

[135] A. Brataas, Y. Tserkovnyak, and G. E. W. Bauer, Phys. Rev. Lett. **101**, 037207 (2008).

[136] W. A. Little, Can. J. Phys. **37**, 334 (1959).

[137] E. T. Swartz, *Thermal resistance at interfaces*, Ph.D. thesis, Cornell University (1987).

[138] E. T. Swartz and R. O. Pohl, Rev. Mod. Phys. **61**, 605 (1989).

[139] J. W. S. Rayleigh, *The Theory of Sound* (MacMillan, 1894).

[140] P. Debye, Annalen der Physik **39**, 789 (1912).

[141] S. Hunklinger and C. Kittel, *Einführung in die Festkörperphysik*, Einführung in die Festkörperphysik (Oldenbourg Wissenschaftsverlag, 2005).

[142] R. M. Costescu, M. A. Wall, and D. G. Cahill, Phys. Rev. B **67**, 054302 (2003).

[143] B. C. Gundrum, D. G. Cahill, and R. S. Averback, Phys. Rev. B **72**, 245426 (2005).

[144] C. M. Bhandari and G. S. Verma, Phys. Rev. **152**, 731 (1966).

[145] B. Y. Pan, T. Y. Guan, X. C. Hong, S. Y. Zhou, X. Qiu, H. Zhang, and S. Y. Li, EPL (Europhysics Letters) **103**, 37005 (2013).

[146] C. Euler, P. Hołuj, T. Langner, A. Kehlberger, V. I. Vasyuchka, M. Kläui, and G. Jakob, Phys. Rev. B **92**, 094406 (2015).

[147] H. G. A. E. A. ElHaes, *Magnon heat transport and magnon-hole scattering in one and two dimensions spin systems*, Ph.D. thesis, Rheinisch-Westfälische Technische Hochschule Aachen (2004).

[148] M. Montagnese, M. Otter, X. Zotos, D. A. Fishman, N. Hlubek, O. Mityashkin, C. Hess, R. Saint-Martin, S. Singh, A. Revcolevschi, and P. H. M. van Loosdrecht, Phys. Rev. Lett. **110**, 147206 (2013).

[149] R. L. Douglass, Phys. Rev. **129**, 1132 (1963).

[150] A. I. Akhiezer, V. G. Bag'Yakhtar, and S. V. Peletminskii, *Spin Waves*, edited by G. C. J., R. De Bruyn Ouboter, and D. De Klerk (North-Holland Publishing Company - Amsterdam, 1968).

[151] L. D. Landau and E. M. Lifshitz, *Physical Kinetics* (Robert Maxwell, M. C., 1981).

[152] I. V. Kolokolov, V. S. L'vov, and V. B. Cherepanov, Zh. Eksp. Teor. Fiz. **86**, 1131 (1984).

[153] N. P. Padture and P. G. Klemens, J. Am. Ceram. Soc. **80**, 1018 (1997).

[154] H. Sato, Progr. Theoret. Phys. **13**, 119 (1955).

[155] C. M. Srivastava and R. Aiyar, J Phys C **20**, 1119 (1987).

[156] E. Spencer and R. C. LeCraw, IEE PROC-B **109**, 66 (1962).

[157] O. Dzyapko, *Magnon Kinetics in Quasi-Equilibrium under Parametric Pumping Leading to Bose-Einstein Condensation*, Ph.D. thesis, Wilhelms-Universität Münster (2010).

[158] D. S. Hung, Y. P. Fu, S. F. Lee, Y. D. Yao, and F. B. A. Ahad, J. Appl. Phys. **107**, 09A503 (2010).

[159] H. Kurebayashi, O. Dzyapko, V. E. Demidov, D. Fang, A. J. Ferguson, and S. O. Demokritov, Nat Mater **10**, 660 (2011).

[160] Y. Kajiwara, K. Harii, S. Takahashi, J. Ohe, K. Uchida, M. Mizuguchi, H. Umezawa, H. Kawai, K. Ando, K. Takanashi, S. Maekawa, and E. Saitoh, Nature **464**, 262 (2010).

[161] A. E. Clark and R. E. Strakna, J. Appl. Phys. **32**, 1172 (1961).

[162] A. Hofmeister, Phys. Chem. Miner. **33**, 45 (2006).

[163] A. Ikesue, T. Kinoshita, K. Kamata, and K. Yoshida, J. Am. Ceram. Soc. **78**, 1033 (1995).

[164] M. J. Duggin, J. Phys. D: Appl. Phys. **3**, L21 (1970).

[165] N. N. Sirota, P. A. Popv, and I. A. Ivanov, Cryst. Res. Technol. **27**, 535 (1992).

[166] X. Zhou, J. Li, W. J. Nellis, X. Wang, J. Li, H. He, and Q. Wu, J. Appl. Phys. **109**, 083536 (2011).

[167] V. F. Kitaeva, E. V. Zharikov, and I. L. Chistyi, phys. stat. sol. (a) **92**, 475 (1985).

[168] S. M. Rezende, R. L. Rodríguez-Suárez, J. C. Lopez Ortiz, and A. Azevedo, Phys. Rev. B **89**, 134406 (2014).

[169] S. O. Demokritov and V. E. Demidov, IEEE Trans. Magn. **44**, 6 (2008).

[170] M. Schreier, *Spatially resolved spin Seebeck experiments*, Master's thesis, Technische Universität München (2012).

[171] A. Fresnel, *Premier mémoire sur la diffraction de la lumière*, edited by J.-L. Basdevant (1815).

[172] W. Zinth and H. Körner, *Optik, Quantenphänomene und Aufbau der Atome: Mit 13 Tabellen*, Physik : Einführungskurs für Studierende der Naturwissenschaften und Elektrotechnik (Oldenbourg, 1998).

[173] E. Palik, *Handbook of Optical Constants of Solids, Volumes I, II, and III: Subject Index and Contributor Index*, Academic Press Handbook Series (Elsevier Science & Tech, 1985).

[174] P. Potera, S. Ubizskii, C. Sugak, and K. Schwartz, Acta Phys. Pol., A **117**, 181 (2010).

[175] D. L. Wood and K. Nassau, Appl. Opt. **29**, 3704 (1990).

[176] L. Jiji, *Heat Convection* (Springer-Verlag Berlin Heidelberg, 2009).

[177] R. Meservey, P. Tedrow, and V. Kalvey, Solid State Commun. **36**, 969 (1980).

[178] A. W. Smith, Phys. Rev. (Series I) **33**, 295 (1911).

[179] S. Takahashi and S. Maekawa, Sci. Tech. Adv. Mater. **9**, 014105 (2008).

[180] P. C. Dorsey, S. E. Bushnell, R. G. Seed, and C. Vittoria, J. Appl. Phys. **74**, 1242 (1993).

[181] J. Flipse, F. K. Dejene, D. Wagenaar, G. E. W. Bauer, J. B. Youssef, and B. J. van Wees, Phys. Rev. Lett. **113**, 027601 (2014).

[182] M. Agrawal, V. I. Vasyuchka, A. A. Serga, A. Kirihara, P. Pirro, T. Langner, M. B. Jungfleisch, A. V. Chumak, E. T. Papaioannou, and B. Hillebrands, Phys. Rev. B **89**, 224414 (2014).

[183] N. Roschewsky, *Spin Seebeck Effect Experiments*, Master's thesis, Technische Universität München (2014).

[184] M. Agrawal, A. A. Serga, V. Lauer, E. T. Papaioannou, B. Hillebrands, and V. I. Vasyuchka, Appl. Phys. Lett. **105**, 092404 (2014).

[185] M. Weiler, M. Althammer, M. Schreier, J. Lotze, M. Pernpeintner, S. Meyer, H. Huebl, R. Gross, A. Kamra, J. Xiao, Y.-T. Chen, H. Jiao, G. E. W. Bauer, and S. T. B. Goennenwein, Phys. Rev. Lett. **111**, 176601 (2013).

[186] J. Lotze, H. Huebl, R. Gross, and S. T. B. Goennenwein, Phys. Rev. B **90**, 174419 (2014).

[187] J. Casas-Vázquez and D. Jou, Rep. Prog. Phys. **66**, 1937 (2003).

[188] D. Tang and N. Araki, Int. J. Heat Mass Transfer **42**, 855 (1999).

[189] R. Bird, W. Stewart, and E. Lightfoot, *Transport Phenomena*, Wiley International edition (Wiley, 2007).

[190] G. Srinivasan and A. Slavin, *High Frequency Processes in Magnetic Materials* (World Scientific, 1995).

[191] N. Vlietstra, J. Shan, B. J. van Wees, M. Isasa, F. Casanova, and J. Ben Youssef, Phys. Rev. B **90**, 174436 (2014).

[192] W. X. Wang, S. H. Wang, L. K. Zou, J. W. Cai, Z. G. Sun, and J. R. Sun, Appl. Phys. Lett. **105**, 182403 (2014).

[193] E. Padrón-Hernández, A. Azevedo, and S. M. Rezende, Phys. Rev. Lett. **107**, 197203 (2011).

[194] R. O. Cunha, E. Padrón-Hernández, A. Azevedo, and S. M. Rezende, Phys. Rev. B **87**, 184401 (2013).

[195] X. Fan, J. Wu, Y. Chen, M. J. Jerry, H. Zhang, and J. Q. Xiao, Nat Commun **4**, 1799 (2013).

[196] H.-C. Ri, F. Kober, R. Gross, R. P. Huebener, and A. Gupta, Phys. Rev. B **43**, 13739 (1991).

[197] H.-C. Ri, F. Kober, A. Beck, L. Alff, R. Gross, and R. P. Huebener, Phys. Rev. B **47**, 12312 (1993).

[198] D. B. Poker and C. E. Klabunde, Phys. Rev. B **26**, 7012 (1982).

[199] S. Meyer, M. Althammer, S. Geprägs, M. Opel, R. Gross, and S. T. B. Goennenwein, Appl. Phys. Lett. **104**, 242411 (2014).

[200] S. M. Rezende, R. L. Rodríguez-Suárez, R. O. Cunha, A. R. Rodrigues, F. L. A. Machado, G. A. Fonseca Guerra, J. C. Lopez Ortiz, and A. Azevedo, Phys. Rev. B **89**, 014416 (2014).

[201] Z. Q. Qiu and S. D. Bader, Rev. Sci. Instrum. **71**, 1243 (2000).

[202] J. G. Dawber, Analyst **89**, 755 (1964).

[203] A. B. Cahaya, O. A. Tretiakov, and G. E. W. Bauer, Appl. Phys. Lett. **104**, 042402 (2014), 10.1063/1.4863084.

[204] S. Zhang, Phys. Rev. Lett. **85**, 393 (2000).

[205] S. Murakami, in *Advances in Solid State Physics*, Advances in Solid State Physics, Vol. 45, edited by B. Kramer (Springer Berlin Heidelberg, 2006) pp. 197–209.

[206] J. Sinova, D. Culcer, Q. Niu, N. A. Sinitsyn, T. Jungwirth, and A. H. MacDonald, Phys. Rev. Lett. **92**, 126603 (2004).

[207] S. O. Valenzuela and M. Tinkham, Nature **442**, 176 (2006).

[208] T. Kimura, Y. Otani, T. Sato, S. Takahashi, and S. Maekawa, Phys. Rev. Lett. **98**, 156601 (2007).

[209] J. Wunderlich, B.-G. Park, A. C. Irvine, L. P. Zârbo, E. Rozkotová, P. Nemec, V. Novák, J. Sinova, and T. Jungwirth, Science **330**, 1801 (2010).

[210] Y. Tserkovnyak, A. Brataas, and G. E. W. Bauer, Phys. Rev. B **66**, 224403 (2002).

[211] K. Ando, Y. Kajiwara, K. Sasage, K. Uchida, and E. Saitoh, IEEE Trans. Magn. **46**, 3694 (2010).

[212] C. W. Sandweg, Y. Kajiwara, A. V. Chumak, A. A. Serga, V. I. Vasyuchka, M. B. Jungfleisch, E. Saitoh, and B. Hillebrands, Phys. Rev. Lett. **106**, 216601 (2011).

[213] V. Castel, N. Vlietstra, J. Ben Youssef, and B. J. van Wees, Appl. Phys. Lett. **101**, 132414 (2012).

[214] C. M. Jaworski, J. Yang, S. Mack, D. D. Awschalom, J. P. Heremans, and R. C. Myers, Nat Mater **9**, 898 (2010).

[215] L. Liu, C.-F. Pai, Y. Li, H. W. Tseng, D. C. Ralph, and R. A. Buhrman, Science **336**, 555 (2012).

[216] C.-F. Pai, L. Liu, Y. Li, H. Tseng, D. Ralph, and R. Buhrman, Appl. Phys. Lett. **101**, 122404 (2012).

[217] J. Jackson, *Classical electrodynamics* (Wiley, 1975).

[218] L. I. Schiff, *Quantum Mechanics* (McGraw-Hill, 1949).

[219] H.-A. Engel, E. I. Rashba, and B. I. Halperin, "Theory of spin hall effects in semiconductors," in *Handbook of Magnetism and Advanced Magnetic Materials* (John Wiley & Sons, Ltd, 2007).

[220] M. B. Jungfleisch, T. An, K. Ando, Y. Kajiwara, K. Uchida, V. I. Vasyuchka, A. V. Chumak, A. A. Serga, E. Saitoh, and B. Hillebrands, Appl. Phys. Lett. **102**, 062417 (2013).

[221] M. B. Jungfleisch, V. Lauer, R. Neb, A. V. Chumak, and B. Hillebrands, Appl. Phys. Lett. **103**, 022411 (2013).

[222] Z. Qiu, K. Ando, K. Uchida, Y. Kajiwara, R. Takahashi, H. Nakayama, T. An, Y. Fujikawa, and E. Saitoh, Appl. Phys. Lett. **103**, 092404 (2013).

[223] G. Y. Guo, S. Murakami, T.-W. Chen, and N. Nagaosa, Phys. Rev. Lett. **100**, 096401 (2008).

[224] A. Hamadeh, O. d'Allivy Kelly, C. Hahn, H. Meley, R. Bernard, A. H. Molpeceres, V. V. Naletov, M. Viret, A. Anane, V. Cros, S. O. Demokritov, J. L. Prieto, M. Muñoz, G. de Loubens, and O. Klein, Phys. Rev. Lett. **113**, 197203 (2014).

[225] I. M. Miron, K. Garello, G. Gaudin, P.-J. Zermatten, M. V. Costache, S. Auffret, S. Bandiera, B. Rodmacq, A. Schuhl, and P. Gambardella, Nature **476**, 189 (2011).

[226] V. E. Demidov, S. Urazhdin, H. Ulrichs, V. Tiberkevich, A. Slavin, D. Baither, G. Schmitz, and S. O. Demokritov, Nat. Mater. **11**, 1028 (2012).

[227] P. P. J. Haazen, E. Murè, J. H. Franken, R. Lavrijsen, H. J. M. Swagten, and B. Koopmans, Nat. Mater. **12**, 299 (2013).

[228] R. H. Liu, W. L. Lim, and S. Urazhdin, Phys. Rev. Lett. **110**, 147601 (2013).

[229] J. Ryu, K.-J. Lee, and H.-W. Lee, Appl. Phys. Lett. **102**, 172404 (2013).

[230] S. Kasai, K. Kondou, H. Sukegawa, S. Mitani, K. Tsukagoshi, and Y. Otani, Appl. Phys. Lett. **104**, 092408 (2014).

[231] T. Moriyama, S. Takei, M. Nagata, Y. Yoshimura, N. Matsuzaki, T. Terashima, Y. Tserkovnyak, and T. Ono, Appl. Phys. Lett. **106**, 162406 (2015).

[232] L. Liu, T. Moriyama, D. C. Ralph, and R. A. Buhrman, Phys. Rev. Lett. **106**, 036601 (2011).

[233] R. Iguchi, K. Sato, D. Hirobe, S. Daimon, and E. Saitoh, Appl. Phys. Expr. **7**, 013003 (2014).

[234] T. Chiba, G. E. W. Bauer, and S. Takahashi, Phys. Rev. Applied **2**, 034003 (2014).

[235] T. Chiba, M. Schreier, G. E. W. Bauer, and S. Takahashi, J. Appl. Phys. **117**, 17C715 (2015).

[236] L. Bai, P. Hyde, Y. S. Gui, C.-M. Hu, V. Vlaminck, J. E. Pearson, S. D. Bader, and A. Hoffmann, Phys. Rev. Lett. **111**, 217602 (2013).

[237] H. J. Juretschke, J. Appl. Phys. **31**, 1401 (1960).

[238] A. Azevedo, L. H. Vilela-Leão, R. L. Rodríguez-Suárez, A. F. Lacerda Santos, and S. M. Rezende, Phys. Rev. B **83**, 144402 (2011).

[239] K. Levenberg, Quart. Appl. Math. **II**, 164 (1944).

[240] D. W. Marquardt, SIAM J. Appl. Math. **11**, 431 (1963).

[241] A. Azevedo, A. B. Oliveira, F. M. de Aguiar, and S. M. Rezende, Phys. Rev. B **62**, 5331 (2000).

[242] K. Zakeri, J. Lindner, I. Barsukov, R. Meckenstock, M. Farle, U. von Hörsten, H. Wende, W. Keune, J. Rocker, S. S. Kalarickal, K. Lenz, W. Kuch, K. Baberschke, and Z. Frait, Phys. Rev. B **76**, 104416 (2007).

[243] R. D. McMichael, M. D. Stiles, P. J. Chen, and W. F. Egelhoff, J. Appl. Phys. **83**, 7037 (1998).

[244] J. Sklenar, W. Zhang, M. B. Jungfleisch, W. Jiang, H. Chang, J. E. Pearson, M. Wu, J. B. Ketterson, and A. Hoffmann, Phys. Rev. B **92**, 174406 (2015).

[245] C. Hahn, G. de Loubens, M. Viret, O. Klein, V. V. Naletov, and J. Ben Youssef, Phys. Rev. Lett. **111**, 217204 (2013).

[246] D. Wei, M. Obstbaum, M. Ribow, C. H. Back, and G. Woltersdorf, Nat. Commun. **5**, (2014).

[247] M. Weiler, J. M. Shaw, H. T. Nembach, and T. J. Silva, Phys. Rev. Lett. **113**, 157204 (2014).

[248] S. Geller, J. P. Remeika, R. C. Sherwood, H. J. Williams, and G. P. Espinosa, Phys. Rev. **137**, A1034 (1965).

[249] C. E. Patton, Phys. Rep. **103**, 251 (1984).

[250] D. Stancil and A. Prabhakar, *Spin Waves: Theory and Applications* (Springer US, 2009).

[251] Y. Zhou, H. Jiao, Y.-t. Chen, G. E. W. Bauer, and J. Xiao, Phys. Rev. B **88**, 184403 (2013).

[252] K. Kondou, H. Sukegawa, S. Mitani, K. Tsukagoshi, and S. Kasai, Appl. Phys. Expr. **5**, 073002 (2012).

[253] A. R. Mellnik, J. S. Lee, A. Richardella, J. L. Grab, P. J. Mintun, M. H. Fischer, A. Vaezi, A. Manchon, E.-A. Kim, N. Samarth, and D. C. Ralph, Nature **511**, 449 (2014).

[254] W. Zhang, W. Han, X. Jiang, S.-H. Yang, and S. S. P. Parkin, Nat Phys **11**, 496 (2015).

[255] M. Strutt, Archiv f. Elektrot. **17**, 533 (1926).

[256] M. Strutt, Archiv f. Elektrot. **18**, 282 (1927).

[257] D. T. Edmonds and R. G. Petersen, Phys. Rev. Lett. **2**, 499 (1959).

[258] C. Vittoria and J. H. Schelleng, Phys. Rev. B **16**, 4020 (1977).

[259] R. F. Soohoo, Phys. Rev. **131**, 594 (1963).

[260] M. Sparks, *Ferromagnetic-relaxation theory*, McGraw-Hill advanced physics monograph series (McGraw-Hill, 1964).

[261] S. Vonsovskii, *Ferromagnetic Resonance: The Phenomenon of Resonant Absorption of a High-Frequency Magnetic Field in Ferromagnetic Substances*, International series of monographs on solid state physics (Elsevier Science, 2013).

[262] A. Kapelrud and A. Brataas, Phys. Rev. Lett. **111**, 097602 (2013).

[263] A. Clogston, H. Suhl, L. Walker, and P. Anderson, J. Phys. Chem. Solids **1**, 129 (1956).

[264] S. Geschwind and A. M. Clogston, Phys. Rev. **108**, 49 (1957).

[265] R. L. White, J. Appl. Phys. **30**, S182 (1959).

[266] P. C. Fletcher and I. H. Solt, J. Appl. Phys. **30**, S181 (1959).

[267] K. Motizuki, M. Sparks, and P. E. Seiden, Phys. Rev. **140**, A972 (1965).

[268] F. Czeschka, *Spin Currents in Metallic Nanostructures*, Ph.D. thesis, Technische Universität München (2011).

[269] T. Skinner, *Electrical control of spin dynamics in spin-orbit coupled ferromagnets*, Ph.D. thesis, University of Cambridge (2014).

[270] N. Bloembergen and R. W. Damon, Phys. Rev. **85**, 699 (1952).

[271] P. W. Anderson and H. Suhl, Phys. Rev. **100**, 1788 (1955).

ACKNOWLEDGEMENTS

I would like to explicitly thank the following individuals for their unconditional support, in the absence of which I would not have been able to pursue my doctorate:

- *Prof. Dr. Rudolf Gross*, for promoting an atmosphere of appreciation and enabling my doctoral studies to begin with.
- *Dr. habil. Sebastian Goenenwein*, for the many hours spend on improving manuscripts, the invaluable scientific insights, the opportunity to independently choose and pursue research and for lending an ear even during busy times.
- *Dr. habil. Hans Huebl*, for all his clever tricks on just about everything, his magic drawer and for being available at any time.
- *Prof. Dr. Gerrit Bauer*, for his tremendous efforts and strong opinions when collaborating, his hospitality and generosity during my visits to Delft and Sendai and some lessons on what it means to be a scientist.
- *Dr. Stephan Geprägs*, for preparing many of the samples investigated in this thesis and his sociable attitude in the many work and non work related discussion.
- *Dr. Mathias Weiler*, for his expertise on a seemingly endless list of topics and for his enthusiasm that also contributed to me pursuing a doctorate.
- *Dr. Matthias Althammer*, for his technical ingenuity, knowing how to fix or assemble any type of lab equipment.
- *Dr. Akashdeep Kamra*, for being the fantastically instructive theoretician he is, his hospitality, outgoing mindset and for being a good friend.
- *Dr. Matthias Opel*, for his work on keeping the institute's IT up and running.
- *Matthias Pernpeintner*, for enduring being the subject of all my questions starting with "You're the expert on [*insert random topic*], aren't you?" and then actually being able to give insightful answers.
- My fellow "Magnetiker" inmates *Dr. Johannes Lotze, Dr. Sibylle Meyer, Christoph Zollitsch, Hannes Meier-Flaig, Kathrin Ganzhorn*

and *Stefan Weichselbaumer* for providing the fabulous environment that I got to enjoy during my studies and the many times they lent me a hand, fabricated samples or otherwise helped me to advance my agenda.

- *Hans Skarsvåg*, for the discussions and insights on spin transfer torques gained in the collaboration, the time spent in Sendai and his amicable character.
- My master's and bachelor's students *Niklas Roschewsky, Roland Rösslhuber, Franz Kramer, Erich Dobler* and *Arthur Niedermayer*, for all the time they spent in the lab while I was ... busy in my office, their passion and the fantastic work that all of them have done.
- *Ludwig Ossiander* and *Emel Dönertas*, for keeping administrative issues away from me whenever possible and their help with a lot of little things.
- *Thomas Brenninger*, for his phenomenal work on the design of the Halbach rotation stage.
- *Karen Helm-Knapp* and *Astrid Habel*, for the many printed circuit boards and dias fabricated and advises on all things chemical.
- *Robert Müller, Helmut Thies, Christian Reichlmeier, Georg Nitschke* and *Alexander Rößl*, for invaluable and outstanding craftsmanship and being handy whenever anything required real mechanical expertise.
- *Siegfried Wanninger* and *Ulrich Guggenberger*, for their expertise and helpful contributions to experiments and constructions.
- My parents *Martina* and *Gunter* as well as my sister *Elisabeth*, for their unconditional support, their love and patience that, above all else, made my studies possible. *Thank you.*
- My wife *Atcharee*, for insisting that my work ends weekdays at five (at the latest), keeping my mind of physics and taking care of me. ผมรักคุณ